Propositions ("Stellingen")

Accompanying the dissertation of M.B. Nooru-Mohamed.

- Shear loading on partially opened cracks with small crack openings triggers secondary cracking. This effect is so dominant that it changes the entire behaviour of the specimen.

- The terminology mixed-mode fracture for heterogeneous materials like concrete needs some revision. The curved crack associated with mixed-mode loading can simply arise due to mode I crack propagation.

- The aspects of path dependency and the occurrence of various failure modes impose restrictions on the formulation of a constitutive relation between normal and shear stresses and normal and shear deformations on a rough crack.

- Even though fracture mechanics research of concrete started three decades ago, the applications remain on the ground. The take off is expected sometime in the foreseeable future.

- But in science the credit goes to the man who convinces the world, not to the man to whom the idea first occurs.

  [Sir] Francis Darwin
  *Eugenic Review 1914, **6**, 1*

  This aphorism is particularly persuasive as far as the size effect law of Bažant is concerned.

- Not only the bright, but also the dull side of the experimental findings must be reported. By doing so, the person who attempts to validate his model is adequately warned of the pitfalls.

- It is often emphasized that numerical and experimental fracture research must go hand in hand. However, in reality the two groups, the experimentalist and the numerical analyst, appear to be living in two different worlds. A healthy development can be both groups coming under one roof and interacting more frequently than before.

- Dutch society in general is tolerant towards foreigners. However, the unrestricted flow of (economic)migrants seeking asylum on the pretext of political persecution might aggravate the racial undercurrent which is competing to be heard in the wider public.

- The ending of the cold war and the fall of the Soviet Union paved the way for the United States to become the undisputed leader of the world. This is not a favourable outcome. A balance of power must remain to prevent one party dictates terms in world affairs.

- A compatible magnetic card must be available to make photocopies at various faculty libraries as well as the central library of the university. This avoids unnecessary paper work and provides easy use.

- The brain drain in the developing countries is a form of loss of resources. The mismanagement of the economy, nepotism and the misuse of power by the ruling class add to the frustration of the literate and the illiterate alike. When countries are ethnically divided there must be a consensus between the (ruling) majority and the minorities such that give and take must prevail. Most importantly, a person should be judged because of what he/she knows or what he/she is and rather not because of where he/she comes from or what he/she professes.

- There must be a balance between the material advancement and the spiritual fulfilment. Negating one or the other can harm the well being of the human being.

- Democracy is being advocated as a panacea for the illness of the world. As long as poverty, hunger and illiteracy remain democracy is meaningless.

Mixed-mode fracture of concrete: an experimental approach

Koninklijke Bibliotheek, The Hague Cataloging in Publication Data

Nooru-Mohamed, Mohamed Buhary

Mixed-mode fracture of concrete: an experimental approach / Mohamed Buhary Nooru-Mohamed. -[S.l. :s.n.]. -Ill.
Thesis Technische Universiteit Delft. -With ref. - With summary in Dutch.
ISBN 90-9005047-7
Subject heading: fracture of concrete

ISBN 90-9005047-7

Printed in the Netherlands by Universiteitsdrukkerij, Delft Univerity of Technology, Delft.

Mixed-mode fracture of concrete: an experimental approach

Proefschrift

ter verkrijging van de graad van doctor aan de Technische Universiteit Delft, op gezag van de Rector Magnificus, prof. drs. P.A. Schenck, in het openbaar te verdedigen ten overstaan van een commissie aangewezen door het College van Dekanen op 21 mei 1992 te 16.00 uur door

Mohamed Buhary Nooru-Mohamed

geboren te Hingul-Oya, Ceylon
civiel ingenieur

Dit proefschrift is goedgekeurd door de promotoren:
Prof. dr. ir. R. de Borst
Prof. dr. -Ing. H.W. Reinhardt

en de toegevoegd promotor:
Dr. ir. J.G.M. van Mier

Mixed-mode fracture of concrete: an experimental approach

Thesis

In fulfillment of the requirements for the degree of Doctor in technical sciences, at Delft University of Technology, under the authority of the Rector Magnificus, prof. drs. P.A. Schenck, and to be defended in public for a committee appointed by the board of Deans on May 21, 1992 at 16:00 hours by

Mohamed Buhary Nooru-Mohamed

Born at Hingul-Oya, Ceylon
Civil Engineer

This thesis is approved by the dissertation directors:
Prof. Dr. ir. R. de Borst
Prof. Dr. -Ing. H.W. Reinhardt

and the associate dissertation director:
Dr. ir. J.G.M. van Mier

To My Parents
&
To Thajul Mazaya

Acknowledgements

I wish to place on record my deepest gratitude to Delft University of Technology for availing me the opportunity to work towards my Ph.D. degree.

A contact with Prof. Dr.-Ing. H.W. Reinhardt, the former head of the Stevin Laboratory and my (second)dissertation director, paved the way for me to join the research group at Delft. I thank him for this opportunity.

My deepest gratitude is extended to Dr. Ir. J.G.M. van Mier, my advisor and associate dissertation director for his guidance, advice, criticism and fruitful discussions throughout this research. It was a pleasure to have been associated with him on this research.

I thank Prof. Dr. Ir. R. de Borst, my (first)dissertation director for his kind assistance during this study.

I am indebted to Mr. Ing. G. Timmers for his expert, innovative methods in instrumentation, performing the experiments and full fledged cooperation throughout this research.

I thank Mr. A. Wensveen and Mr. Ir. H. Voorsluis of the Measurements and Instrumentation group of the Stevin Laboratory for their substantial assistance in building the biaxial testing machine and the data acquisition system.

I thank all Colleagues of the Concrete Structures group for the support, and the lovely environment during my stay.

The partial financial support by the "Stichting Professor Bakkerfons", U.S. Air Force Office of Scientific Research (AFOSR contract no. F49620-88-C-0135) and the Netherlands Center for Civil Engineering, Research, Codes and Specifications (CUR, Committee A30) is highly appreciated.

Contents

page

1 **Introduction** 1

2 **From the literature** 5
- 2.1 Linear elastic fracture mechanics 5
- 2.2 Nonlinear fracture mechanics 6
- 2.2.1 Fictitious Crack Model(FCM) 7
- 2.2.2 Crack Band Model(CBM) 9
- 2.3 Crack methodology 10
- 2.3.1 Discrete crack concept 10
- 2.3.2 Smeared crack concept 13
- 2.4 Mixed-mode fracture criteria 20
- 2.5 Mixed-mode test geometries 24

3 **Experimental procedure** 29
- 3.1 Materials and specimens 29
- 3.2 Loading frame 31
- 3.3 Measuring system 36
- 3.3.1 Load and displacement measurements 36
- 3.3.2 Test control 42
- 3.3.3 Data acquisition system 44
- 3.4 Experimental problems 45
- 3.4.1 Influence of glue platens 45
- 3.4.2 Frame rotations 47
- 3.4.3 Plate spring behaviour and the development of bending moments in the frame assembly 49

4 **Experimental results and discussions** 54
- 4.1 Load-path description 54
- 4.2 Compressive shear versus tensile shear 61
- 4.3 Influence of crack opening 68
- 4.4 Influence of axial confinement 72
- 4.4.1 Lytag unconfined shear(load-path 3a) 73
- 4.4.2 Lytag confined shear (load-path 3b) 75
- 4.4.3 Shear stiffness analysis 81
- 4.5 Influence of material structure 84
- 4.6 Influence of lateral confinement 87
- 4.6.1 Experiments 87

4.6.2 Numerical simulation 93
4.7 Size related influence 96
4.7.1 Load-path 4 versus three specimen sizes 95
4.7.2 Load-path 5 versus three sizes 98
4.7.3 Load-path 6 versus three sizes 101
4.7.4 Size effect 108
4.8 Path dependence 112
4.9 Failure mechanism 113

5 Conclusions and Recommendations 117

Notations 120

References 122

Appendices

A0 Information regarding test series 131
A1 Additional results of load-path 1(b) experiments 134
A2 Test scheme corresponding to load-path 3 135
A3 Load-path 3a and 3b results for 2 mm mortar 136
A4 Load-path 3a and 3b results for 16 mm concrete 140
A5 Test scheme for load-path 0, 4, 5, and 6 experiments 144
A6 Load-path 5c crack patterns for three sizes 145
A7 Load-path 6b and 6c crack patterns for three sizes 146

Summary 148

Samenvatting 150

1 Introduction

Most engineering materials inherently possess flaws and damage from the very fabrication of the material itself. Due to catastrophic failures in the past which have resulted in damage to the economy, human beings and to the environment, the engineering community has re-examined its design codes and provisions. An option was to base the design on fracture mechanics principles. As a consequence, knowledge, expertise and experience on the application of fracture mechanics to metallic materials grew. This development prompted concrete researchers to also analyze brittle disordered materials like concrete in the light of fracture mechanics principles. Yet, the application of fracture mechanics principles to real life concrete structures is still a far reaching goal.

The concrete code provisions which exist today are based on empirical formulations which have been obtained from a number of laboratory tests. More and more new cement based materials have been proposed and the technological development demands such materials. Moreover, the use of concrete structures in adverse situations such as nuclear storage facilities, tall structures in earthquake prone regions, off-shore platforms, and storage tanks for liquid gases at cryogenic temperature imposes stringent conditions on the safety and the performance of those structures. A fracture mechanics based approach may be a good option to meet these challenges especially to analyze thick-walled structures under shear loading.

In fracture mechanics terminology, three modes known as mode I, II and III occur in solids due to the normal load, in-plane shear load and out-of-plane shear load respectively (Fig. 1.1). In other words, mode I, II and III are known as "opening mode", "shearing mode" and "tearing mode". These three modes essentially describe three independent kinematic movements of the upper and lower crack surfaces with respect to each other and are sufficient to describe all the possible modes of crack propagation in an elastic material.

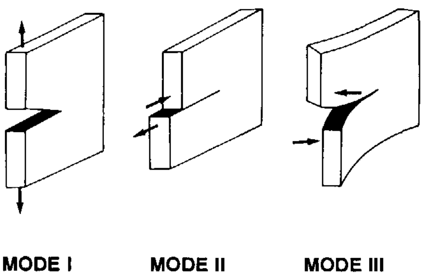

Fig. 1.1 Three modes of loading: mode I opening mode, mode II shearing mode , mode III tearing mode (from Broek[88]).

definition

In practice most cracks results from mode I loading. The other modes may occur in combination with mode I. That is I-II, I-III or I-II-III. In this study, *mode I(tension)* and *the combination of mode I and mode II(shear)* loading conditions are considered (the latter combination is hereafter referred to as *mixed-mode loading*).

Much attention has been focused on obtaining a better understanding of mode I fracture of concrete and an enormous amount of data and nonlinear mode I fracture theories was generated. Such a large number of studies was not devoted to mixed-mode fracture of concrete. It may be that the inherent difficulties in performing realistic mixed-mode experiments hamper the development of proper mixed-mode theories. For this reason, nonlinear mixed-mode theories are not yet well developed for heterogeneous materials like concrete. However, real life situations are seldom confined to mode I behaviour. In general combined tension/shear stress state or mixed-mode fracture prevails.

In Fig. 1.2, a four point bend beam is shown. Suppose two cracks A and B form at the symmetric and non-symmetric region of the beam. The crack A forms because the principal tensile stress is exceeded at the outer edge of the beam. This corresponds to mode I crack opening. In the shear zone crack B tends to bend which is a consequence of the inclination of the principal stress. Also, crack B is initiated as a mode I crack, perpendicular to the largest principal stress. During further loading, the crack opens more and is loaded by shear simultaneously(Reinhrdt et al.[89]). At and behind the tip (as indicated by 2 and 3 in Fig. 1.2) of crack B, a combined tensile (mode I) and shear (mode II) stress state arises. This is an example, where the crack forms due to tension and becomes a mixed-mode crack due to the presence of shear.

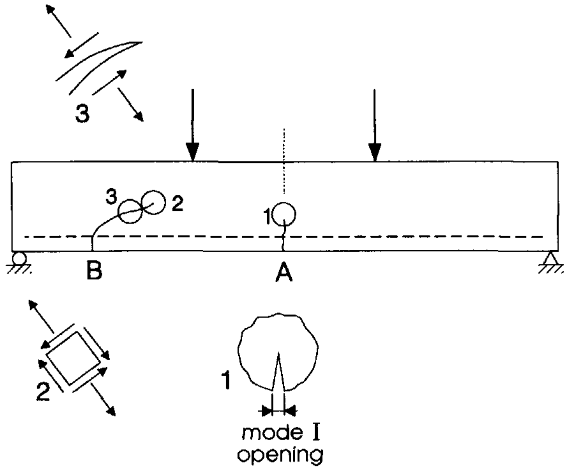

Figure 1.2 Four point bend beam.

two approaches

Mixed-mode fracture of concrete can be looked upon in two different ways. The first approach is to subject a crack to a mixed-mode stress field and to study the fracture propagation in terms of macrocrack evolution. Traditional fracture mechanics parameters are extracted. Along this line, the Iosipescu single-notched-beam geometry (Iosipescu[67]) (Fig. 1.3a) was first adapted by Arrea & Ingraffea[82] for the mixed-mode studies of concrete. The loading arrangement in this geometry was chosen such that a large shear to moment ratio (mode II to mode I) prevailed at the notch tip. As the crack initiated from the notch tip and propagated under load, the mode I component began to dominate, and the mode II/mode I ratio decreased (Arrea & Ingraffea[82]). The situation in this geometry is similar to crack growth in real structures, where mixed-mode loading leads to a rotation of the principal stress direction after mode I crack nucleation. The same geometry was proposed for a mixed-mode round robin test by the RILEM technical committee, Fracture Mechanics Testing (RILEM-89-FMT) (Shah & Carpinteri[91]).

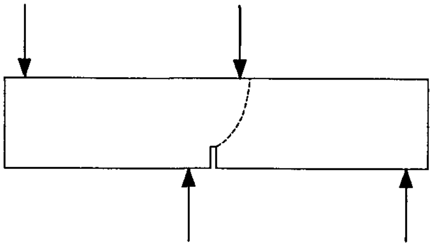

Fig. 1.3a Iosipescu beam geometry.

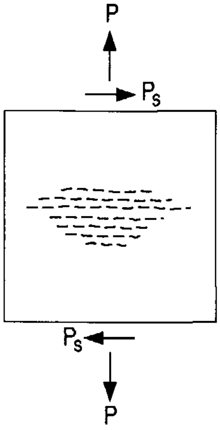

Fig. 1.3b Process zone testing.

The second approach is to determine the material properties within the fracture process zone subjected to a mixed-mode loading (Fig.1.3b). The fracture process zone is defined as the region of discontinuous microcracking ahead of a continuous macrocrack (Mindess[90]). The push-off type specimen used by Reinhardt et al.[87] and the quadratic cube specimen adopted by Hassanzadeh[89] fall in this category. Reinhardt et al.[87] used the push-off type specimens to study the mixed-mode fracture process zone. A fracture plane was created between the saw cuts of the push-off specimen by means of a tensile force and subsequently shear was applied as compression or tension. Furthermore, the quadratic cube geometry was used by Hassanzadeh[89] to measure the material properties within a fracture process zone subjected to mixed-mode loading.

purpose

The behaviour of concrete subjected to mixed-mode loading is studied using the recently developed biaxial machine at the Stevin Laboratory of Delft University of Technology. The biaxial machine consists of two independent frames which are capable of moving along the vertical and horizontal directions. Axial load and lateral shear are applied to the specimen through this configuration of independent loading frames. Double-Edge-Notched concrete square plate specimens with three different size are used.

In order to study the fracture process in concrete, seven load-paths have been pursued, which fall into three broad categories. The first deals with the investigation on the shear capacity of partially opened cracks. The crack openings are within the range 0 to 400 μm and still capable of transmitting tensile load normal to the crack face. The validity of aggregate interlock theories at small crack openings can be investigated. The second deals with the behaviour of concrete subjected to shear (mode II) without any pre-crack. The third deals with the behaviour of concrete subjected to a combination of tension (mode I) and shear (mode II) in uncracked specimens.

During the four year period the testing technique was gradually updated which can be seen in the results discussed in chapter 4. At present the testing arrangement is such that any load-path can be pursued in a fully automated manner.

In the study no attempts were made to model-mixed mode fracture of concrete. The main goal was to optimize the testing and to obtain reliable mixed-mode results.

three level approach

It is most important to define the level at which the observations were made in interpreting experimental results. The three level approach proposed by Wittmann[83] consists of a hierarchical system. The three levels are: (a) the micro level, which is concerned with the structure of the hardened cement paste (b) the meso level, which deals with pores, inclusions, cracks and interfaces, and (c) the macro level, which is related to the structural element. This means that the models on the different levels are interrelated in a systematic way, or more precisely, models on the given level are based on the results of the previous level. At the macro level the information which comes out of the previous two levels is used to describe the material behaviour.

In this study, the meso level is considered as the level of observation for explaining the experimental results.

2 From the literature

This is not a comprehensive literature survey. In this chapter attempts are made to review some aspects of the state of the art in fracture mechanics of concrete. At the beginning, the early developments in the Linear Elastic Fracture Mechanics (LEFM) of concrete is discussed. Thereafter the Nonlinear Fracture Mechanics of concrete and the related mode I crack models are addressed. Numerical modelling of cracked concrete in terms of discrete and smeared crack is presented. Finally, the mixed-mode fracture criteria and some of the mixed-mode geometries are looked into.

2.1 Linear elastic fracture mechanics (mode I)

After the pioneering work of Kaplan[61], a great deal of time and energy has been devoted to applications of LEFM principles to characterize fracture of concrete, mortar and cement paste. In the early days, researchers have attempted to derive the traditional, global LEFM parameters such as the critical stress intensity factor K_c, the critical energy release rate G_c etc. for the above materials. Subsequent work involved determining the relation between K_c and the various parameters related to concrete, such as the aggregate size, water-cement ratio, air content, strength, age, rate of loading etc. Yet, there was no agreement with respect to which specimen size should be chosen to characterize the fracture mechanics parameters in the most appropriate manner (Mindess[84]). Indeed, it became apparent that a straightforward application of the concepts of metal fracture to concrete is not possible.

The micro-mechanical structure of concrete is entirely different from that of metals. Concrete is a porous material containing aggregates, hardened cement paste and water. At the meso level there exist pores, cracks, inclusions and interfaces. Due to the composite nature of concrete, the cracking process is also very complicated. Micro-cracks at the interface between coarse aggregate and mortar matrix exist in plain concrete before any load is applied (Hsu[63]). This is due to bleeding, volume changes during hydration and drying shrinkage.

According to Hsu[63] bond between the aggregate and the matrix is the weakest link in the heterogeneous concrete system. Bond cracks exist even before any load is applied. Once a specimen is subjected to a load, approximately 30 percent of the peak load, de-bonding starts at the interface. The load-displacement (P-δ) diagram start to deviate from linearity. During subsequent loading energy dissipation occurs due to the formation of micro-cracks. Therefore, failure is not brittle for concrete-like materials, but softening in nature. Using crack detection techniques Van Mier[90] has for example shown that crack face grain bridging is the main physical explanation for softening (see Fig. 2.1).

Sih[84] questions the meaning of G_c or K_c in LEFM, when the source of energy release does not coincide with the instability of a single crack. Additional energy can be dissipated during slow crack growth and local material damage before the catastrophic failure. He argued that K_{Ic} in LEFM should be interpreted as a material behaviour parameter rather than a material constant.

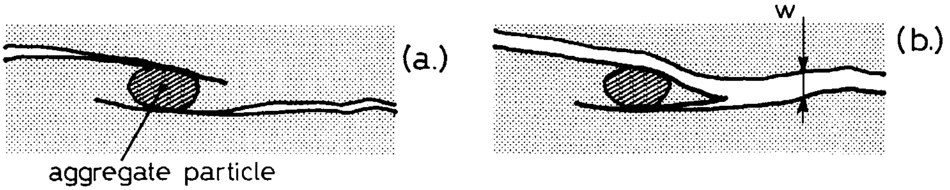

Figure 2.1 Crack interface grain bridging (a) falilure of bridge (b), after Van Mier[90].

2.2 Nonlinear fracture mechanics

The existence of a fracture process zone in concrete is now widely accepted by the concrete fracture mechanics community. Mindess[83] has defined it as the region of discontinuous microcracking ahead of a continuous (visible) crack. The question is whether there is a fracture process zone in concrete, and if so, what are the dimensions of it. Until now there is no agreement to this effect. The RILEM technical committee 89-FMT (Fracture Mechanics Test Methods) has reported fifteen methods to determine the fracture process zone in concrete. The extent of the fracture process zone ranged from a few μm to 500 mm according to the above study. It is also suggested that the fracture process zone is not a material property (at least for laboratory-size specimens), but depends on the specimen geometry and method of loading.

For three materials, viz. a truly linear elastic material, a metal and a concrete the extent of hypothesized fracture process zone is shown in Fig. 2.2. The size of the fracture process zone is larger for concrete than for metals or for a truly linear elastic material. Linear elastic fracture mechanics requires this zone to be small in comparison with the size of the structure. On the contrary, concrete-like, heterogeneous materials behave nonlinearly in a rather large fracture process zone. Initially it was believed that the load transferring capacity of the softening zone is a material property and is a function of the deformation of the localized zone. However, Van Mier[84,85], Read & Hegemier[84] and Sandler[84] have argued that softening is not a true material property, but is rather a manifestation of progressive increase of damage that depends on specimen geometry, size and experimental conditions. However part of it will be a manifestation of the material itself and, Van Mier[90] has recently argued that softening is the consequence of crack face grain bridging. This experimental result is supported with results obtained from two distinct numerical micromechanics models, see Schlangen & Van Mier[91b] and Vonk et al.[91].

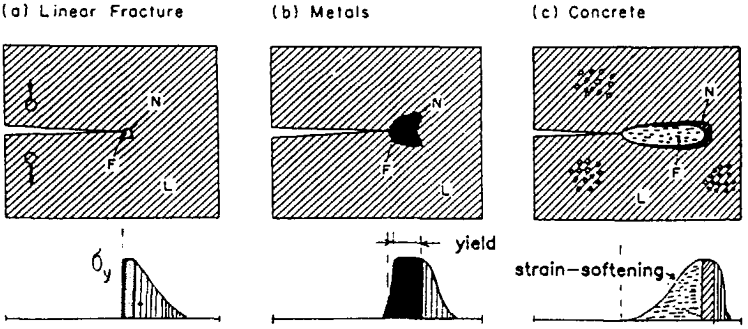

Figure 2.2 Hypothesised fracture process zone (from Bazant & Oh[83]) .

The fracture process zone, has become a convenient tool in formulating two well known fracture models for concrete, namely the fictitious crack model (Hillerborg et al.[76]) and the crack band model (Bazant & Oh[83]). In these models not so much the physical background is considered important, but rather a mechanics view point is taken and the energy dissipation of an equivalent crack system is considered to be the only necessary information.

2.2.1 Fictitious Crack Model (FCM)

The Fictitious Crack Model(FCM) proposed by Hillerborg and co-workers is a simplified tool for analyzing concrete structures. The concept in the FCM is similar to the plastic crack model proposed by Dugdale[60] / Barentblat[62] for metal fracture. As shown in Fig. 2.3, in a tensile member that is stretched under uniaxial tension a fracture zone forms in region A once the major principal stress reaches the tensile strength f_t of the material. When the crack opens, the stress is not assumed to fall to zero at once, but to decrease gradually with increasing crack width w, even though the material in the damaged zone is localized. Meanwhile, the material outside the localized region unloads. The behaviour of the bulk of the body and the localized behaviour can be represented by two distinct graphs. The bulk behaviour corresponds to the elastic region of the specimen where loading and unloading is possible. It is described by a σ-ε graph where ε represents the strain in the elastic region anywhere outside the fracture zone. In the fracture zone progressive (micro)cracking takes place and the crack width w increases. So the $\sigma-w$ plot corresponds to the fracture zone deformation.

In other words, the FCM or the cohesive crack model accounts for:

- bulk behaviour: normally represented through a linear $\sigma-\varepsilon$ curve
- crack initiation criterion: maximum tensile strength $= f_t$
- crack evolution criterion : $\sigma = f(w)$ curve normally schematized as a bilinear diagram.

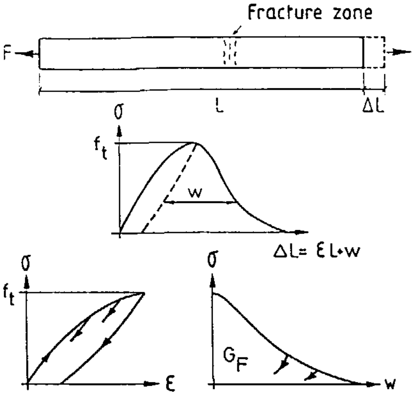

Figure 2.3 Fictitious Crack Model (FCM), after Hillerborg[76].

The area under the $\sigma-\omega$ curve is equated to the fracture energy G_F of the material. It is defined as the amount of energy expended in creating a unit area of a completely open crack. Note that G_F is different from G_c (critical strain energy release rate). In order to obtain G_F, a deformation controlled uniaxial tensile test is considered the best solution (Petersson[81]). However carrying out such a test properly requires a sophisticated closed-loop system. A pitfall of the test was discovered recently: Van Mier[86] and Hordijk et al.[87] recognised that non-symmetric fracture modes occur in uniaxial tensile tests, which was attributed to the heterogeneous nature of the material. The mechanism was correctly simulated by numerical means by Rots et al.[87] and Rots & De Borst[88]. Following this, Hillerborg and co-workers developed a stability criterion for the specimen machine system, and claimed that the process-zone properties can be derived from a test on a small specimen in a machine with sufficient stiffness (Zhou[88]). A three point bend test is generally recommended in order to determine G_F instead of a uniaxial tension test. This is due to its simplicity, so that it can be carried out in many laboratories. Accordingly, a round robin test by means of three point bend tests on the determination of the fracture energy G_F was recommended by RILEM. In Fig. 2.4, the G_F values reported by 14 different laboratories were plotted against the beam depth of the specimens used. As can be seen in Fig. 2.4, the values of G_F, determined by the RILEM method, in tendency size dependent. The reason for this phenomenon is attributed to the the tortuosity of the crack, energy dissipation outside the fracture zone. In addition different procedures followed in respective laboratories might contribute to the scatter in G_F values too.

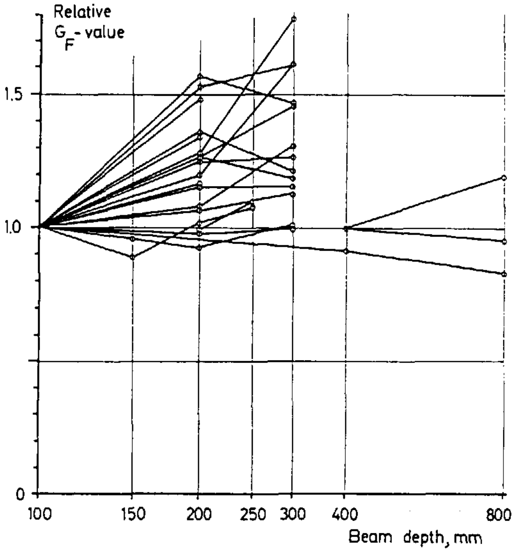

Figure 2.4 G_F versus beam depth (Hillerborg[85]).

It is important to note that the FCM can also be applied to initially un-notched structures as long as the fracture initiation criterion is the tensile strength. In this case, the stress is due to other reasons than the stress concentration in front of the notch. Moreover, the FCM can be used to study the development of the fracture zone, the initiation of crack growth and the propagation of the crack through the material.

2.2.2 Crack Band Model (CBM)

The Crack Band Model proposed by Bazant and Oh[83] is similar in bulk behaviour and crack initiation criterion but differs in crack evolution criterion from that of the FCM. In the Crack Band Model, it is assumed that fracture in a heterogeneous material can be modelled as a band of parallel, densely distributed microcracks with a blunt front. The crack band width w_c, which usually assumed to be equal to three times the maximum aggregate size is considered as a material property (Bazant & Oh [83]), see Fig. 2.5. The fracture energy G_F is then given as w_c times the area under the uniaxial complete tensile stress-strain diagram, or more precisely, the area under the loading and unloading diagrams emanating from the peak stress point. In its simplest form the σ-ε diagram may be taken as bilinear. The bulk and the localized behaviour are represented in a $\sigma-\varepsilon$ diagram. In the CBM, the three material fracture parameters are the fracture energy, the uniaxial tensile strength and the crack band width. The strain-softening modulus E_t which represents the stiffness degradation in the process zone, is a function of these three parameters. Bazant & Oh[83] argued that the CBM is advantageous over the FCM due to computational efficiency. In the CBM, the crack is modelled by changing the isotropic elastic moduli matrix into an orthotropic one, reducing the material stiffness in the direction normal to the cracks in the band.

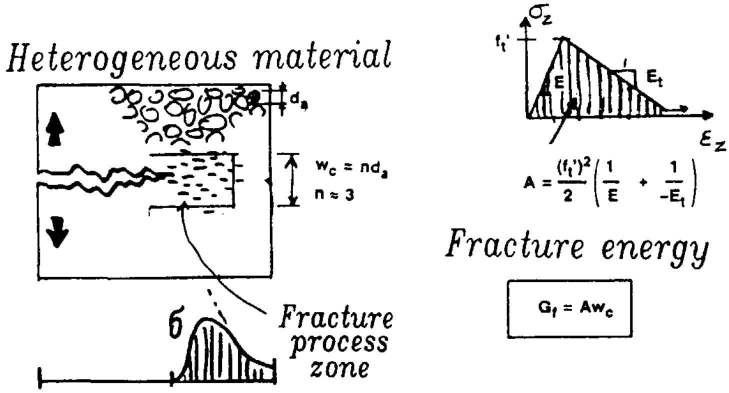

Figure 2.5 Illustration of the Crack Band Model, after Bazant & Oh[83].

2.3 Crack methodology

2.3.1 Discrete crack concept

In order to model cracking of concrete numerically two types of crack concepts were advocated. They are the discrete crack and the smeared crack models. In the discrete crack model (Ngo & Scordelis[67]), the common node between two elements is split into two when the tensile strength of the material is reached(Fig. 2.6). One of the disadvantages of this method is the constant change of the nodal connectivity of the finite element mesh. Another disadvantage is that the crack growth is along a pre-defined path, viz. along the element edges. In order to overcome this problem, Ingraffea & Saouma[84] proposed an interactive approach to discrete cracking. Following this procedure, the mesh automatically adjusted in the vicinity of a crack to accommodate arbitrary crack trajectories.

implementation of the FCM in discrete crack approach

In a finite element analysis, the refinement of the element mesh would lead to a very high stress concentration at the notch tip, if the softening of the material was not accounted for. If only the stress criterion was used for crack propagation the results would not converge upon the mesh refinement. However, convergence is attained when the FCM is used as demonstrated by Petersson & Gustavsson[80].

Implementing the FCM in the Finite Element analysis, two approaches have been adopted by researchers. Firstly, the crack path is known in advance and the element mesh is arranged such that the crack path coincides with element boundaries as shown in Fig. 2.7a. Secondly, the crack path is not known before, but, (a) the mesh is rearranged and

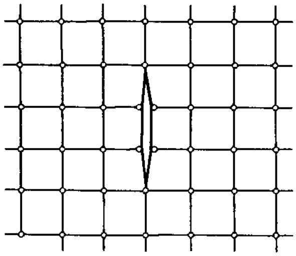

Figure 2.6 Discrete Crack Model (from Chen & Saleeb[82]).

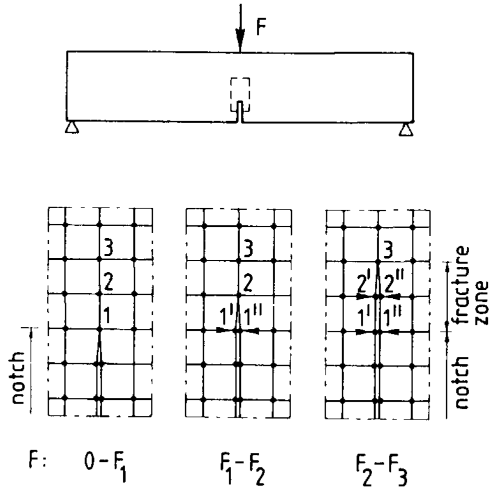

Figure 2.7a Discrete Crack, when the crack path is known (from Hillerborg[85b]).

successively new boundaries are added in order to simulate the crack path (Fig. 2.7b) or (b) the crack path is represented by a path following the boundaries of the original mesh, but the probable correct path is approximated (Fig. 2.7c).

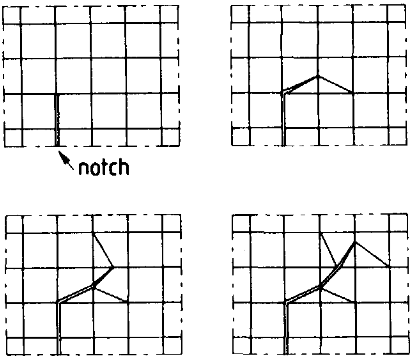

Figure 2.7b Rearrangement of the mesh, when the crack path is not known before (from Hillerborg[85b]).

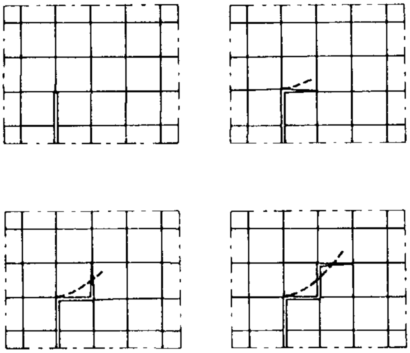

Figure 2.7c Approximate crack path (from Hillerborg[85b]).

In Fig. 2.8, the experimental and the simulated F-δ curves carried out on a three point bend beam by Petersson[81] are shown. He has simulated the global P-δ curve by means of the Fictitious Crack Model thereby assuming a linear and a bi-linear σ-w relation.The relevant material parameters, used for the computation are shown in the inset of Fig. 2.8. As can be seen in Fig. 2.8, the simulated P-δ curve using the bilinear softening curve comes closer to the experimental observation. Furthermore, the linear approximation overestimated the peak load. This shows the dependence of the simulated global P-δ response on the choice of a $\sigma-$w curve.

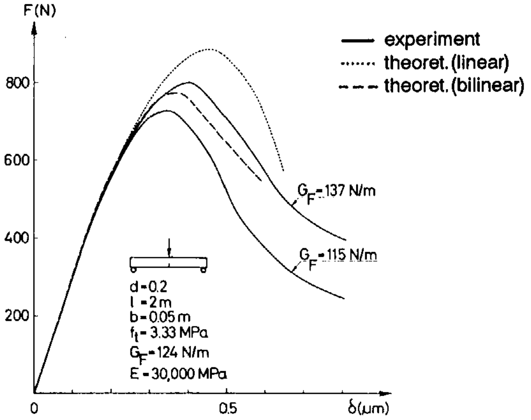

Figure 2.8 Comparison of global P-δ response from numerical simulations and experiments (discrete approach), after Petersson[81].

2.3.2 *Smeared crack concept*

The smeared crack approach is a continuum formulation, where concrete is treated as a homogeneous continuum which permits a description in terms of stress and strain. The smeared approach was first proposed by Rashid[68] to analyze reinforced concrete pressure vessels. Here cracking was assumed to grow in a band of parallel cracks distributed over a finitely sized zone rather than in a single crack (Fig. 2.9). Consequently, the numerical implementation is easier, since the approach only requires a change of the stiffness matrix of the element after cracking. The advantage of this procedure is that the topology of the original finite element mesh remains preserved which is computationally convenient.

The smeared crack concept can be divided into three broad categories. They are (1) fixed, (2) fixed multidirectional, and (3) rotating smeared crack concepts.

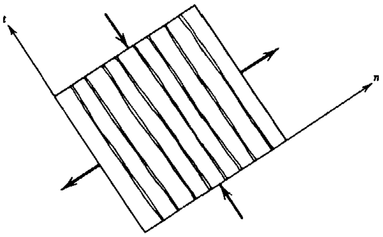

Figure 2.9 Smeared Crack Model (from Chen & Saleeb[82]).

fixed smeared crack model

In the fixed smeared crack model, when the local principal stress reaches the tensile strength of the material, or when the combination of principal stresses violates the tension cut off criterion, a fixed crack is formed perpendicular to the principal tensile stress. The isotropic stress strain law is changed into an orthotropic law (Rashid[68]) following,

$$\begin{vmatrix} \Delta\sigma_{nn} \\ \Delta\sigma_{tt} \\ \Delta\sigma_{nt} \end{vmatrix} = \begin{vmatrix} 0 & 0 & 0 \\ 0 & E & 0 \\ 0 & 0 & 0 \end{vmatrix} \begin{vmatrix} \Delta\varepsilon_{nn} \\ \Delta\varepsilon_{tt} \\ \Delta\varepsilon_{nt} \end{vmatrix} \qquad .....(2.1)$$

Two modifications were later made to (2.1). They are: (1) incorporation of a negative normal retention μ, as a result of the uniaxial softening, and (2) incorporation of shear retention β to reduce numerical difficulties. The orthotropic law for a two dimensional configuration then becomes,

$$\begin{vmatrix} \Delta\sigma_{nn} \\ \Delta\sigma_{tt} \\ \Delta\sigma_{nt} \end{vmatrix} = (1-\mu\nu^2) \begin{vmatrix} \mu E & \nu\mu E & 0 \\ \nu\mu E & E & 0 \\ 0 & 0 & \beta G/(1-\mu\nu^2) \end{vmatrix} \begin{vmatrix} \Delta\varepsilon_{nn} \\ \Delta\varepsilon_{tt} \\ \Delta\varepsilon_{nt} \end{vmatrix} \qquad .....(2.2)$$

The inclusion of tension softening has significantly widened the application of the smeared crack model. In the smeared application, the fracture energy G_F needs to be treated as the energy released in the crack band h. Therefore, the tensile softening modulus μE needs adjustment with respect to h. A detailed discussion of the subject has been given by Rots[88].

The relation in Eq. (2.2) corresponds to a smeared out relation for the cracked solid, without making any distinction between the crack and the solid material in between the cracks. According to De Borst & Nauta[85], the fixed crack approach has two major disadvantages. Firstly, in a total approach it is impossible to properly combine cracking and other nonlinear phenomena such as plasticity, creep and thermal effects. Secondly, in the fixed concept it is assumed that the crack plane is fixed upon violation of the tension cut off criterion. If a softening model is used after cracking, then a residual normal stress is allowed to act over the crack. As a consequence the combination of the residual normal and the shear load over the crack can cause rotation of the principal stress to a different direction than the normal to the existing crack plane. The above situation cannot be handled properly by a total stress-strain relation.

In order to overcome the above difficulties, De Borst & Nauta[85], decomposed the total strain increment $\Delta\varepsilon$ to a concrete strain increment $\Delta\varepsilon^{co}$ and a crack strain increment $\Delta\varepsilon^{cr}$ such that $\Delta\varepsilon = \Delta\varepsilon^{co} + \Delta\varepsilon^{cr}$. Such a decomposition also has been advocated by Litton[74] and by Bazant[80].

An analysis performed by Rots[88] on a three point bend specimen with the smeared crack concept, which incorporates the strain decomposition criterion mentioned above, is shown in Fig. 2.10. The concrete softening behaviour was implemented via two different curves as was in the FCM, but with a slight modification. In the smeared crack model, the localization is assumed to take place in a crack band (width = h). A stress-strain ($\sigma - \varepsilon^{cr}$) relation for the cracked concrete was used instead of the stress-crack opening ($\sigma - w$) relation as was in the Fictitious Crack Model. In Fig.2.10, the effect of the local softening diagram on the global P$-\delta$ response of a three point bend test is illustrated. Three types of softening diagrams, namely a linear, an exponential and a power law, were used. As shown in Fig.2.10, the exponential softening curve produces a P-δ relation which nicely falls within the experimental scatter. The choice of the softening diagram greatly influences the post peak behaviour of the global P-δ curve(A similar observation based on the discrete crack model is discussed in section 2.3.1).

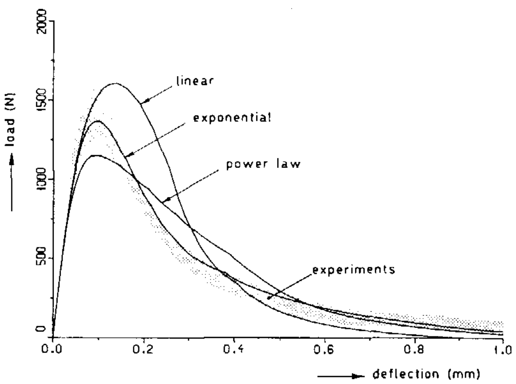

Figure 2.10 Comparison of global P-δ response from numerical simulations and experiments (smeared approach), after Rots[88].

fixed multi-directional smeared crack

The multi-directional fixed smeared crack concept allows the formation of primary and secondary nonorthogonal cracks in a sampling point. A crack forms perpendicular to the principal stress when it reaches the tensile strength of the solid. After the crack formation, further loading leads to a change of the principal stress directions. A new secondary crack is allowed to form when the angle between the principal stress direction and the normal to the existing crack has exceeded a threshold angle α (De Borst & Nauta[85]). Similarly, based on this criterion a third and more cracks are allowed to form. When the second crack opens the previously formed crack is allowed to close. According to De Borst[91], the fixed multi-directional concept is the most flexible and sophisticated smeared crack model available to date, however, with some notable disadvantages. They are: (1) the threshold angle α which is unknown and must be chosen by the user, (2) what should be done with the energy that is dissipated within each crack, (3) the robust algorithmic treatment for the tension-compression stress state remains a problem, and (4) implementation is not straightforward in situations where new cracks open or when closing or re-opening of existing cracks occur.

shear retention factor
In smeared crack models the capacity of cracked concrete to transmit shear is expressed in terms of a shear retention factor β, which was first introduced by Suidan & Schnobrich[73] in the finite element formulation. Originally the shear retention capacity of the cracked concrete was assumed to be zero upon crack formation. This caused numerical problems.

The physical motivation for introducing β is that a shear force can be transmitted across a crack due to the interlocking of aggregate particles that protrude from the crack face or by the dowel action of the reinforcement crossing the crack. The shear transfer mechanism of cracked concrete has been an active area of research in the 1980s. So far, few analytical models have been proposed to describe and predict the aggregate interlock phenomenon. Among them are the model based on the frictional sliding of the two rigid crack faces (Fardis & Buyukozturk[79]), the rough crack model (Bazant & Gambarova[80]), and the two phase model (Walraven[80]) and the contact density model (Li et al.[89]), which are all suitable for general use. A comparative study using a discrete crack finite element model has been carried out by Feenstra et al.[91a,b].

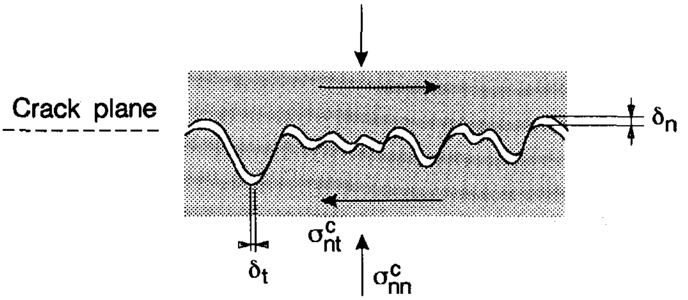

Figure 2.11 Rough Crack.

In Fig. 2.11, a single rough crack is shown. The axes t and n corresponds to the tangential and normal directions respectively and δ_n, δ_t corresponds to crack opening and crack sliding. The associated stresses $\sigma^c{}_{nn}$ and $\sigma^c{}_{nt}$ relate to the normal stress and the shear stress along the crack surface respectively. In its most general form the relation between ($\sigma^c{}_{nn}$, $\sigma^c{}_{nt}$) and (δ_n,δ_t) is given by

$$\begin{vmatrix} \sigma^{c}_{nn} \\ \\ \sigma^{c}_{nt} \end{vmatrix} = \begin{vmatrix} B_{nn} & B_{nt} \\ \\ B_{tn} & B_{tt} \end{vmatrix} \begin{vmatrix} \delta_n \\ \\ \delta_t \end{vmatrix}$$

The matrix **B** is called the secant stress-crack displacement relation. For use within the smeared crack approach the crack displacements can be converted to strains, where the crack is assumed to be distributed over a band width h.

The stress-displacement relation transforms as follows:

$$\begin{vmatrix} \sigma^{c}_{nn} \\ \\ \sigma^{c}_{nt} \end{vmatrix} = \begin{vmatrix} D_{nn}^{cr} & D_{nt}^{cr} \\ \\ D_{tn}^{cr} & D_{tt}^{cr} \end{vmatrix} \begin{vmatrix} \varepsilon_{nn}^{c} \\ \\ \gamma_{nt}^{cr} \end{vmatrix}$$

where $\varepsilon_{nn}^{cr} = \delta_n/h$, $\varepsilon_{tt}^{cr} = 0, \gamma_{nt} = \delta_t/h$, and $D_{ij}^{cr} = hBij$

Aggregate interlock experiments are needed to determine the coefficients of the crack secant stiffness matrix. Walraven & Keuser[87] concluded from experimental observations that $D_{nt}^{cr} \neq D_{tn}^{cr}$. The matrix is therefore non-symmetric.

From the aggregate interlock experiments with a constant crack width (Walraven[80]) a minimum shear displacement δ_t is required in order to activate the normal stress σ_{nn}. According to Walraven & Keuser[87], most structures to be analyzed fall below this range and they assume $D_{nt}^{cr} = 0$. The coefficient D_{tn}^{cr} is also assumed to be zero, so that D_{tt}^{cr} is a function of δ_n only. Therefore, the stress-strain relation is simplified as follows:

$$\begin{vmatrix} \sigma_{nn}^{c} \\ \\ \sigma_{nt}^{c} \end{vmatrix} = \begin{vmatrix} D_{nn}^{cr} & 0 \\ \\ 0 & D_{tt}^{cr} \end{vmatrix} \begin{vmatrix} \varepsilon_{nn}^{cr} \\ \\ \gamma_{nt}^{cr} \end{vmatrix}$$

In chapter 4 the aggregate interlock results obtained by Walraven[80] for specimens with external restraining bars are compared with the results obtained in this study.

It is important to realize the differences between the present study and the aggregate interlock experiments. In aggregate interlock experiments a completely open crack was created in an uncontrolled manner and subsequently loaded in shear. However, when the crack openings are small, the failure mechanism not only involves aggregate interlock but also fracture evolution.

rotating crack model
In the rotating crack model the orthotropic material axes are allowed to rotate such that the material axes coincide with the axes of the principal strain. Rots[88] has shown that the rotating crack concept can be derived as the limiting case of the fixed multi-directional smeared crack concept.

The difference in the three approaches is the way in which the crack direction is treated. It is either kept constant (fixed single), updated in a stepwise manner following a threshold angle (fixed multi-directional) or updated continuously. The advantage of the fixed multi-directional crack concept is that it preserves the permanent memory of the damage orientation whereas the rotating crack concept does not.

Rots[88] has performed analyses incorporating the fixed, rotating and discrete crack concepts on a single notched shear beam, and compared the experimental results of Arrea & Ingraffea[82] (see Fig. 2.12). For the fixed crack, he has assumed the threshold angle $\alpha = 60^0$ with three shear retention values (i.e., $\beta = 0$, 0.05 and variable). As can be seen in Fig. 2.12, the rotating and the fixed (with $\beta = 0$) crack model come close to the experimental findings.

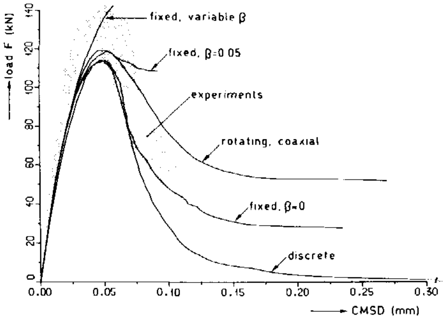

Figure 2.12 Comparison of three different smeared crack models, after Rots[88].

The major advantage of the rotating crack model is that the choice of a value for β is eliminated. A disadvantage is that it is more difficult to make contact with experimental fracture research because one cannot incorporate results from aggregate interlock studies (Rots[88]). The results reported in this study, especially load-path 4, 5 and 6 fall in line with the assumptions made in the rotating crack model.

Another interesting option might be to use numerical micromechanics. In Fig. 2.13, crack patterns obtained by De Borst[86], Rots[88] and Schlangen & Van Mier[91b], based on the smeared crack model, rotating crack model and the recently proposed lattice model respectively, are shown. In Fig. 2.13a, the geometry and the loading arrangements are

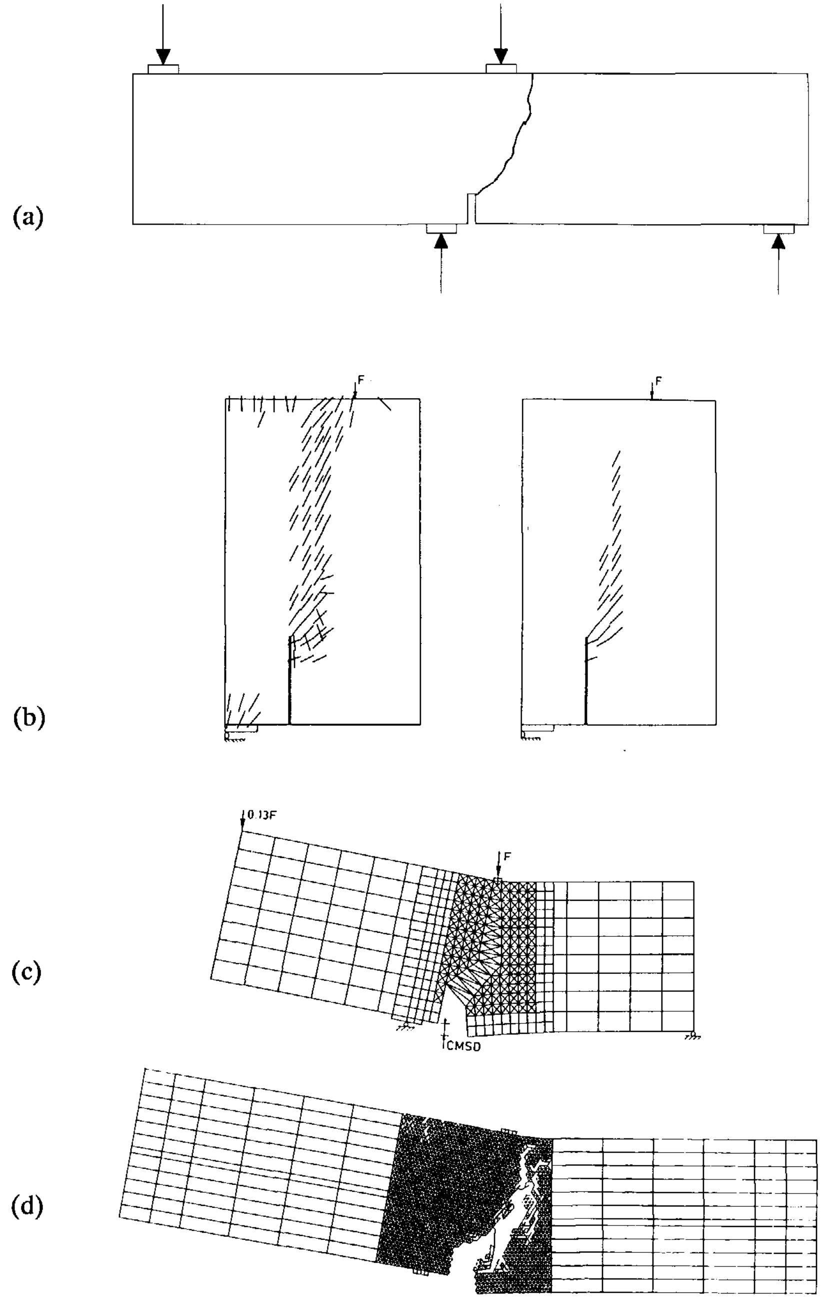

Figure 2.13 Single notched shear beam (a): final crack pattern based on fixed smeared model, De Borst[86] (b); fixed rotating smeared model, Rots[88] (c); and lattice model, Schlangen & Van Mier[91b](d).

illustrated. As can be seen in Fig. 2.13, all three crack patters differ in terms of the final end point. As shown in Fig. 2.13b,c and d, the final crack tip falls between the notch and the load F, at the load F and away from the load for the three simulations respectively. The simulation based on the lattice model resembles the curved crack observed in the experiment. It should be mentioned that the results of the lattice model are independent of the chosen lattice. The deviations in the final crack patterns suggest that, to a certain extent, the classical smeared crack approach fails to capture the localized fracture behaviour. The results suggest that the numerical micromechanics can indeed be a valid tool for mixed-mode crack studies.

2.4 Mixed-mode fracture criteria

A proper mixed-mode criterion, which is applicable to concrete-like heterogeneous material as such is currently not available. The existing mixed-mode fracture criteria are based on the linear elastic, ideally homogeneous materials (metals).

For addressing the mixed-mode fracture in concrete-like heterogeneous materials an extension of the FCM to mixed-mode may be a good option. In this area, not much work has yet been done.

In a mixed mode loading situation, fracture is assumed to occur when the combination of mode I and mode II energies reaches a critical value. Using an energy balance approach the total energy release G_t is given by

$$G_t = G_I + G_{II} \qquad .....(2.3)$$

where $G_I = (1-\nu^2)K_I^2/E$ and $G_{II} = (1-\nu^2)K_{II}^2/E$

Hence, the fracture condition would be

$$K^2_I + K^2_{II} = K^2_{Ic} \qquad .....(2.4)$$

For mode I cracking $K_{II} = 0$, or $K^2_I = K^2_{Ic}$ and for mode II cracking $K_I = 0$ or $K^2_{II} = K^2_{IIc}$. Consequently, equation (2.4) predicts $K_{IIc} = K_{Ic}$ and the locus for combined mode cracking is a circle. However, in practice $K_{IIc} \neq K_{Ic}$ and the fracture condition is more likely to be:

$$(K_I/K_{Ic})^2 + (K_{II}/K_{IIc})^2 = 1 \qquad .....(2.5)$$

The above condition is based on the assumption that the crack propagates in a self-similar manner. In other words, it is assumed that crack extension will be in the plane of the original crack. However, in a combined mode it is not obvious whether fracture proceeds in a self-similar manner. In mixed-mode experiments, it is usually observed that crack extension takes place under an angle with respect to the original crack (Broek[86]). This invalidates the standard expression for the energy release rate G. A modified energy release criterion would be that the crack growth will take place in the direction of maximum energy release rate. In that case, G has to be evaluated as a function of the crack growth angle. This is equivalent to the Maximum Stress Criterion(MSC) (Erdogan & Sih[63]). The maximum stress criterion and the Strain Energy Density Criterion(SEDC) (Sih[74]) are the two criteria for mixed-mode loading that allow crack growth under an angle.

Maximum Stress Criterion

A typical text book problem is shown in Fig. 2.14, where a biaxial remote load is applied to a plate with an inclined crack of length 2a. This is a mixed-mode problem as defined in Chapter 1, where at the tip of an advancing crack a mixed-mode stress state prevails.

The Maximum Stress Criterion (Erdogan & Sih[63]) can be described as follows: the crack extends in a radial direction from its tip and the direction of crack propagation is normal to the maximum tangential stress σ_θ. Equation (2.6) shows the relation

$$\sigma_\theta = K_I{*}f_1(\theta)/\sqrt{r} + K_{II}{*}f_2(\theta)/\sqrt{r} + 0(r^0) \qquad \text{......} (2.6)$$

where f_1 and f_2 are functions of θ and $K_I = \sigma_2\sqrt{\pi a}[s + (1\text{-}s)\sin^2\beta]$ and $K_{II} = \sigma_2\sqrt{\pi a}(1\text{-}s)\sin\beta\cos\beta$ where $\sigma_1/\sigma_2 = \sigma$.

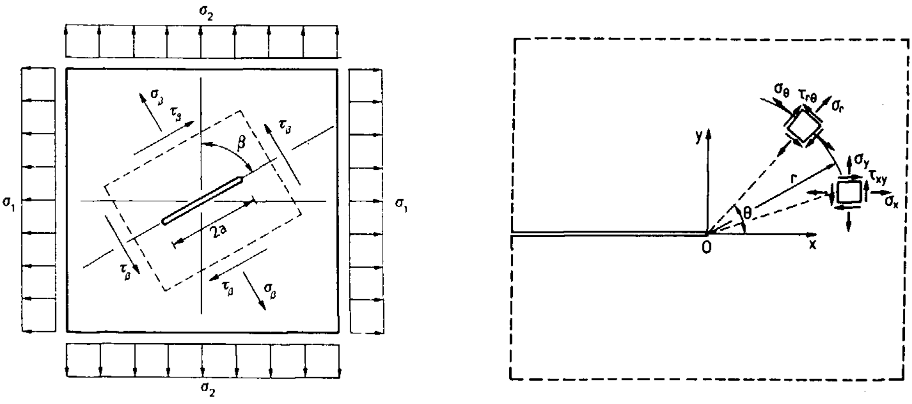

Figure 2.14 Inclined crack subjected to a biaxial stress field(from Carpinteri[86] & Gdoutos[91]).

A relation for the crack extension angle θ and crack angle β can be obtained from the condition $d\sigma_\theta/d\theta = 0$ and $d^2\sigma_\theta/d\theta^2 < 0$ at $\theta = \theta_0$. This will leads to the following relation connecting θ and β.

$$[s+(1\text{-}s)\sin^2\beta]\sin\theta + [1/2(1\text{-}s)\sin 2\beta](3\cos\theta -1) = 0 \qquad \text{......(2.7)}$$

which can be transformed into:

$$2(1\text{-}s)\sin 2\beta\,(\tan\theta/2)^2 -2[s + (1\text{-}s)\sin 2\beta](\tan\theta/2)-(1\text{-}s)\sin 2\beta = 0 \qquad \text{.......(2.8)}$$

Equation (2.8) yields the crack initiation angle with respect to various ratios of σ_1/σ_2.

Strain Energy Density Criterion

A drawback of the Maximum Stress Criterion discussed above is that the process of fracture is not explained in terms of an energy approach. Therefore Sih[74] proposed an alternative method on the basis of energy considerations prior to crack propagation at a possible site of failure. The site of failure can be a crack tip, a notch front, a highly stressed material in an unflawed structure. This theory is developed on the basis of a *strain energy density factor* *S* for a material element at a finite distance r_0 from the point of failure initiation (Fig.2.15). Note that S is defined by

$S = r_0\, dW/dV$, where dW/dV is the strain energy density function per unit volume and given as follows.

$$dW/dV = 1/r[\,a_{11}K_I^2 + 2a_{12}K_IK_{II} + a_{22}K_{II}^2] \qquad \text{.... (2.9)}$$

The coefficients $a_{ij}(i,j = 1,2)$ are given by

$16\mu a_{11} = (1 + \cos\theta)(\kappa - \cos\theta)$

$16\mu a_{12} = \sin\theta\,[\,2\cos\theta - (\kappa\text{-}1)]$

$16\mu a_{22} = (k+1)(1 - \cos\theta) + (1 + \cos\theta)(3\cos\theta -1)$

$\kappa = (3-4\nu)$ for plane strain

$\kappa = (3-\nu)/(1+\nu)$ for plane stress

The strain energy density criterion need to satisfy the following two hypotheses:

(a) The crack initiation direction is toward the point of minimum strain energy density factor S_{min}.

That is $dS/d\theta = 0$, $d^2S/d\theta^2 < 0$ for $\theta = \theta_0$ and

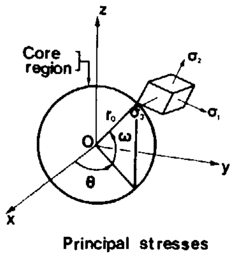

Figure 2.15 A material element and co-ordinate system (from Gdoutos[84]).

(b) Fracture initiation is assumed to occur when S_{min} reaches a maximum valued S_{cr}.

Using the above two hypotheses, it is possible to determine the crack initiation angle and the critical load. For an extensive treatment on the SEDC for mixed mode problems, the reader is referred to Gdoutos[84,90].

The MSC and the SEDC has been proposed for ideally homogeneous, linear elastic isotropic materials. Given the nature of concrete, the applicability of these theories is highly debatable. Another drawback of these theories is their formulation with the crack tip stress intensity factors K_I and K_{II}. For text book type problems closed-form solutions exist for the stress intensity factors. However, for other geometries one has to rely on numerical tools, in order to determine the stress intensity factors.

In spite of these objections, Arrea and Ingraffea[82] concluded that the SEDC predicted the closest initial instability load (for concrete) as compared to the experimental values. The fracture initiation angle predicted by this theory was only 3% higher than the average fracture angle measured in their beam tests.

There exists consensus among the researchers that, by increasing the size-scale of the concrete element the influence of heterogeneity disappears, and the body can be considered macroscopically homogeneous. The influence of the non-linear softening material behaviour vanishes by simply increasing the size of the concrete element and the crack propagation is governed by the linear elastic stress-singularity in the crack tip region (Petersson[81], Carpinteri[85]).

A proper mixed-mode failure criterion which is applicable to concrete-like heterogeneous materials is not available. It may be that a lack of sound mixed-mode test results has made it difficult to formulate a theory.

2.5 Mixed-mode test geometries

A compilation of mixed-mode geometries adopted world wide is given in the RILEM reports: 90-FMA (chapter 4, Hordijk et al.[90]) and 89-FMT (chapter 3, Carpinteri & Swartz[91]). Various specimen geometries have been proposed for mixed-mode studies of concrete. They can be classified into two broad categories, namely the beam geometry and the quadratic or rectangular prism or cube geometry.

beam geometry

The Iosipescu[67] single edge notched beam geometry was first adopted by Arrea & Ingraffea[82] for mixed mode testing of concrete (Fig. 2.16). The loading arrangement, shown in Fig. 2.16, is such that the tip of the crack propagates in a mixed-mode stress field. By changing the load and the reaction point the stress field at the crack tip could be varied from mode I to almost pure mode II. The chosen loading system introduces a high K_{II}/K_I ratio at the tip of the sawn notch. As the crack propagates from the notch, this ratio decreases and the mode I stress intensity factor begins to dominate. Numerical analyses on the above geometry based on the various smeared crack models have been reported by De Borst[86] and Rots & De Borst[87], and numerical micromechanics by Schlangen & Van Mier[91b]. Some of the experimental and numerical results are shown in Fig. 2.13.

In order to study shear fracture of concrete, Bazant & Pfeiffer[85] proposed a double notched beam geometry as shown in Fig. 2.17. The loading arrangement chosen in this geometry allows a narrow band of confined shear crack near the notch. This specimen geometry and the results obtained by Bazant & Pfeiffer[85] brought much controversy and discussion among the researchers.

Bazant & Pfeiffer[86], carried out their test at a constant displacement rate of the piston. This implies that the deformation in the actuator is controlled which corresponds to a load control testing. Therefore, the final failure may have been of a dynamic nature.

The main conclusions drawn by Bazant & Pfeiffer[85] are: (1) shear fracture exists, (2) the shear (mode II) fracture energy is thirty times larger than the mode I fracture energy, and (3) the direction of propagation is not mode I, rather in a direction where the energy release rate for the entire structure is maximized.

Regarding the existence of shear fracture they remark that "microscopically, of course, the shear fracture is likely to form as a zone of tensile microcracks with predominantly 45^0-inclined which only later connect by shearing; but the fact is that in the macroscopic sense the observed fractures must be described as mode II"(see Fig. 2.17b).

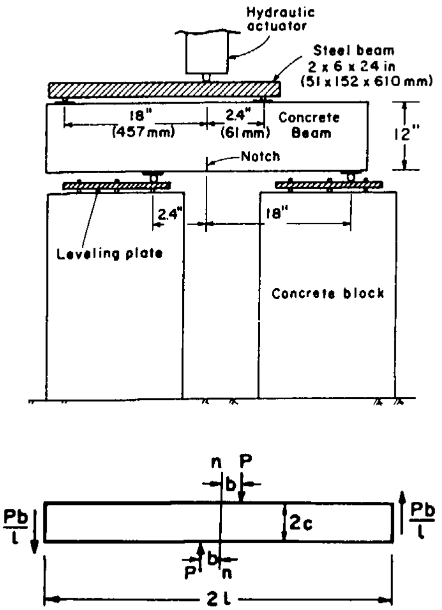

Figure 2.16 Iosipescu beam geometry adapted by Arrea & Ingraffea[82].

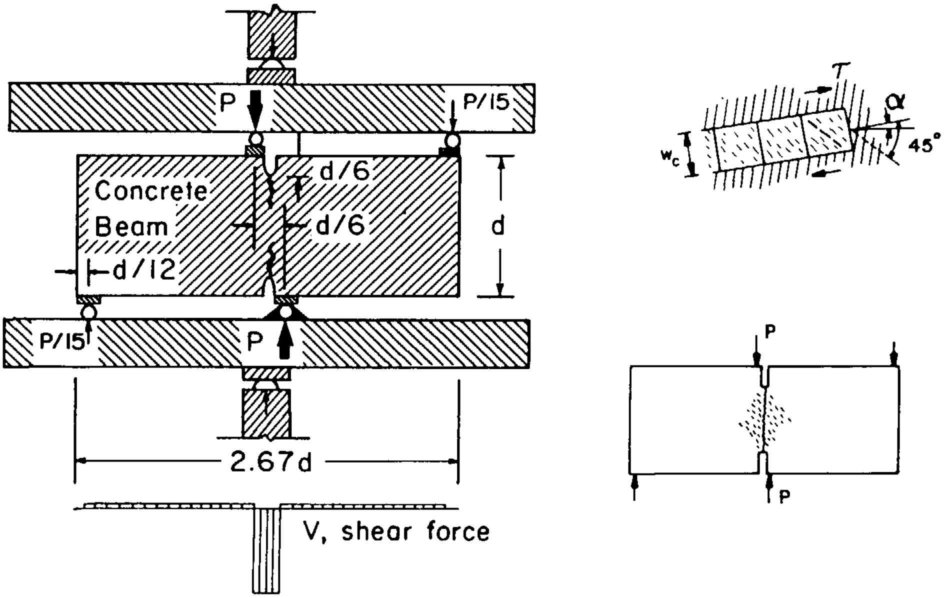

Figure 2.17 Double-edge-notched beam tested by Bazant & Pfeiffer[85].

Ingraffea and Panthaki[85] were the first to negate the findings of Bazant & Pfeiffer[85,86] and concluded that the beam tested by the latter failed by tensile cracking and not through a shear failure. Moreover, the tensile crack nucleated in the central region of the beam, roughly vertical just, as in the Brazilian test and propagated towards the notch tips. Ingraffea & Panthaki[85] came to the above conclusion using a numerical analyses based on linear elastic fracture mechanics concepts. Recently the same geometry was repeated by Van Mier et al.[92].

In addition, Rots & De Borst[87] also analyzed the Iosipescu beam tested by Arrea & Ingraffea[82] and the double notched shear beam tested by Bazant & Pfeiffer[85,86], using the smeared crack approach with shear softening. Rots & De Borst[87] concluded that their study does not reveal the existence of pure mode II fractures in concrete, nor did it confirm the idea that concrete always fracture in mode I. They suggested a mixed-mode mechanism in which tensile softening dominates before peak and shear softening effects take over in the post peak regime.

Among all the beam geometries adopted so far, the aim was to extract global fracture mechanics parameters, such as mixed-mode fracture energy and/or, mode II fracture energy $G_{f,II}$ in accordance with the classical fracture mechanics concepts. However, there is a growing concern over the terminology mixed-mode fracture. Some researchers believe, that only tensile fracture matters in concrete. If there is a mixed-mode fracture energy called G_{mixed}, then what percentage of $G_{F,I}$ and $G_{F,II}$ constitute that mixed-mode fracture energy?

It is not yet clear whether one can extract a G_{mixed} from the present day test configuration. However, Carpinteri et al.[90] estimated the mixed-mode fracture energy from their single edge notched Iosipescu beam tests and conclude that G_{mixed} is approximately 19-31% higher than the mode I fracture energy $G_{F,I}$, depending on the size of the specimen and the size of the aggregates in the mix. Intriguingly, Schlangen & Van Mier[91a] argued that Carpinteri et al.[90] neglected the friction at the loading points and supports in the experiment, thereby overestimating the so called G_{mixed}. In Schlangen & Van Mier[91a] it was shown that the contribution of $G_{F,II}$ for this case is negligible.

quadratic or rectangular prism or cube geometry

Fig. 2.18a shows the push-off type specimen used by Reinhardt et al.[87]. To accommodate the push-off type specimens, a mixed-mode loading frame discussed in Chapter 3 was built. The purpose at that time was to uniformly open a crack and to obtain global mixed-mode parameters. However, from uniaxial experiments, non-uniform crack opening was observed until average crack openings $\delta = 40\,\mu m$, see Van Mier and Nooru-Mohamed[88]. This was one of the reasons to adopt the Double-Edge-Notched(DEN) (Fig. 2.18b) geometry with larger area in between the notches. Another reason was that shear in push-off specimen was not clear enough, see Watkins and Liu[85]. In the initial tests S-shaped cracks were observed, which suggest dominant mode I behaviour. Due to the larger ligament area in the DEN specimens, crack propagation could easily be followed and any eccentricities in the machine could be traced.

In Fig. 2.19, the grooved cube specimen adopted by Hassanzadeh[89] on mixed-mode testing is shown. The main aim in their work was to determine the properties of a fracture process zone subjected to mixed-mode loading. They achieved this by first creating a fracture process zone in tension and later applying shear in along pre-defined straight or parabolic paths. The results obtained by Hassanzadeh[89] following the linear path are compared with some of load-path results obtained in the present study, see chapter 4.

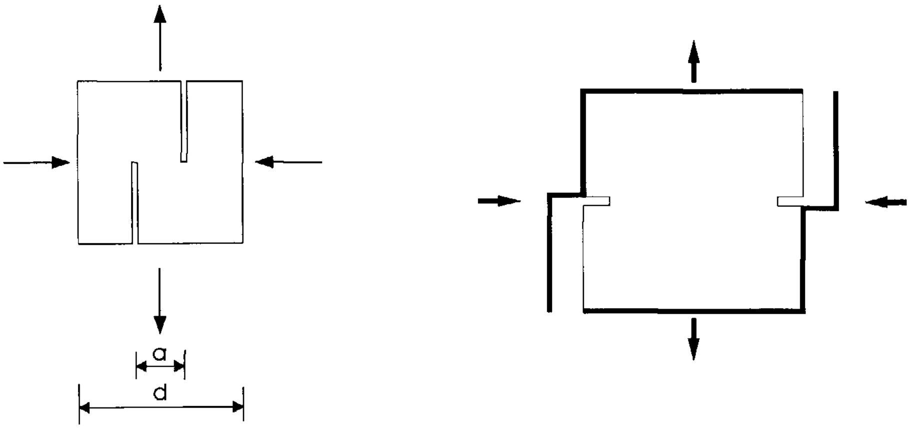

Figure 2.18 Push-off (a) and Double-Edge-Notched specimen (b).

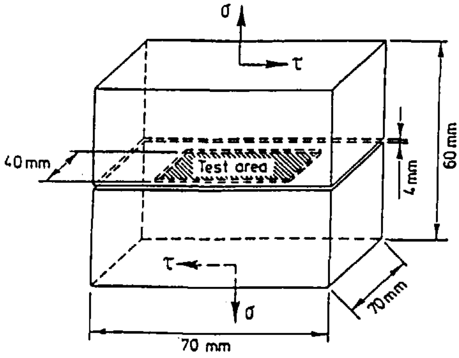

Figure 2.19 Quadratic prism or cube geometry for mixed-mode testing.

hollow cylindrical geometry

Hollow cylindrical specimens were adopted by Keuser & Walraven[89] for mixed-mode studies of concrete, see Fig. 2.20. The inner diameter and the thickness of the specimen were 250 and 20 mm respectively. The upper and the lower part of the specimen were glued in a steel holder such that a free length of 20 mm remained for crack propagation. The specimen was precracked to a desired crack opening. Thereafter an axial tension and a torsional moment were applied simultaneously. Keuser & Walraven[88] were convinced that a torsional moment would create a uniform distribution of shear stress along the circumferencial direction of the specimen.

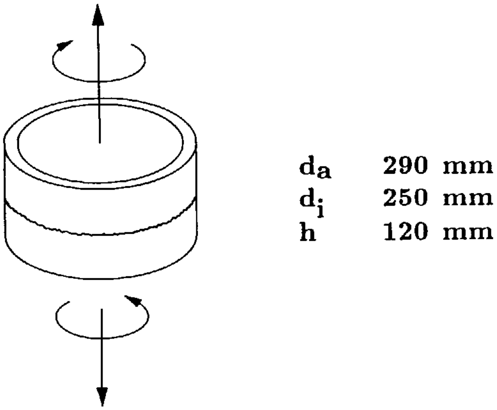

Figure 2.20 Hollow cylindrical specimen adopted by Keuser & Walraven[88].

3 Experimental procedure

At the beginning of this chapter, the material aspects and the specimen preparation are discussed. Afterwards, the biaxial loading frame, measuring system, test control, data acquisition system, and the local deformation measurements are described. Also the difficulties in the testing machine are considered and the behaviour of the frame assembly is outlined.

3.1 Materials and Specimens

Most of the experiments were conducted using mortar matrix of 2 mm maximum aggregate size. But also normal weight and lightweight high strength concrete of maximum aggregate size d_{max} of 16 and 12 mm respectively were used for a material related study. The different mix designs are shown in Table 3.1. The strength results and the maximum aggregate size corresponding to each batch are shown in Table 3.2. Five plates of size 300x300x50 mm were cast in a battery mould in the vertical direction. After two days of casting the plates were demoulded and cured under water. The plates were sawn (using a rotating diamond saw) after 14 days into square Double-Edge-Notched (DEN) specimens of dimension 200x200x50 mm with a notch depth of 25 mm and a width of 5 mm as shown in Fig. 3.1(a).

Table 3.1 Concrete Mix Design

	Normalweightconcrete		Lytag LHSC
d_{max}	2 mm	16 mm	12 mm
Mix proportion	(kg/m^3)	(kg/m^3)	(kg/m^3)
Portland Cement	500	375	330
Water	250	187.5	110.5
Super plasticizer - (Type Melment L10)	-	-	5.0
air content(vol.%)	2.24	1.3	3.75
River Gravel and Sand			
0.125- 0.25	303	128	158
0.25 - 0.50	197	165	237
0.50 - 1.0	515	202	158
1.0 - 2.0	500	256	158
2.0 - 4.0	-	256	79
4.0 - 8.0	-	365	-
8.0 -16.0	-	457	-
Lightweight aggregate			
4.0 - 8.0	-	-	264
8.0 -12.0	-	-	484

In a later test series (46,47 and 48) specimens with different sizes were used, in order to study the size effect in mixed-mode fracture. For this purpose two different battery moulds were used. Each batch consisting of six plates of size 300x300x50 mm and 200x200x50 mm were cast. They were cured as before and sawn after 14 days into specimens of dimension 200x200x50, 100x100x50 and 50x50x50 mm (each having a constant notch to depth ratio a/d = 0.125), see Fig. 3.1b,c. After this, the sawed specimens were placed in a fresh water basin again. At an age of 28 days, the specimens were taken out of the water and left in the laboratory to dry until testing at an ambient temperature of 17-18°C and 50% RH. The drying time varied from 14 to 216 days depending on the test series and the age of loading from 42 to 216 days as shown in Appendix A0.

In Table 3.2, the 28 day cube compressive strength and the splitting tensile strength of the three materials are given. The strength results were obtained from 150 mm cubes as specified in the Dutch codes VB 74/84.

Table 3.2 Strength Results and specimen batch

Batch	Number of Specimens	Max Aggregate d_{max}[mm]	f_c [Mpa]	f_{spl} [Mpa]	Size [mm]
14	5 (14-01/05)	2	46.59(1.37)	3.38(0.27)	200x200x50
15	5 (15-01/05)	2	47.86(0.20)	3.68(0.07)	200x200x50
17	5 (17-01/05)	2	46.49(1.58)	3.95(0.24)	200x200x50
18	5 (18-01/05)	2	48.17(0.36)	3.56(0.27)	200x200x50
26	6 (26-01/06)	2	46.68(0.48)	3.58(0.13)	200x200x50
27	6 (27-01/06)	16	52.47(1.03)	3.61(0.15)	200x200x50
28	6 (28-01/06)	12	49.59(0.41)	3.16(0.18)	200x200x50
29	6 (29-01/06)	12	60.17(0.35)	4.15(0.64)	200x200x50
30	6 (30-01/06)	16	58.75(2.62)	3.97(0.33)	200x200x50
32	6 (32-01/06)	2	46.53(0.69)	3.47(0.28)	200x200x50
46	6(46-01/06)		49.66(2.23)	3.76(0.29)	200x200x50
	6(46-07/12)	2	"	"	100x100x50
	12(46-13/24)		"	"	50x50x50
47	6(47-01/06)		46.19(0.32)	3.78(0.23)	200x200x50
	6(47-07/12)	2	"	"	100x100x50
	12(47-13/24)		"	"	50x50x50
48	6(48-01/06)		46.24(0.37)	3.67(0.29)	200x200x50
	6(48-07/12)	2	"	"	100x100x50
	12(48-13/24)		"	"	50x50x50

N.B. numbers between brackets are the standard deviation in [MPa].

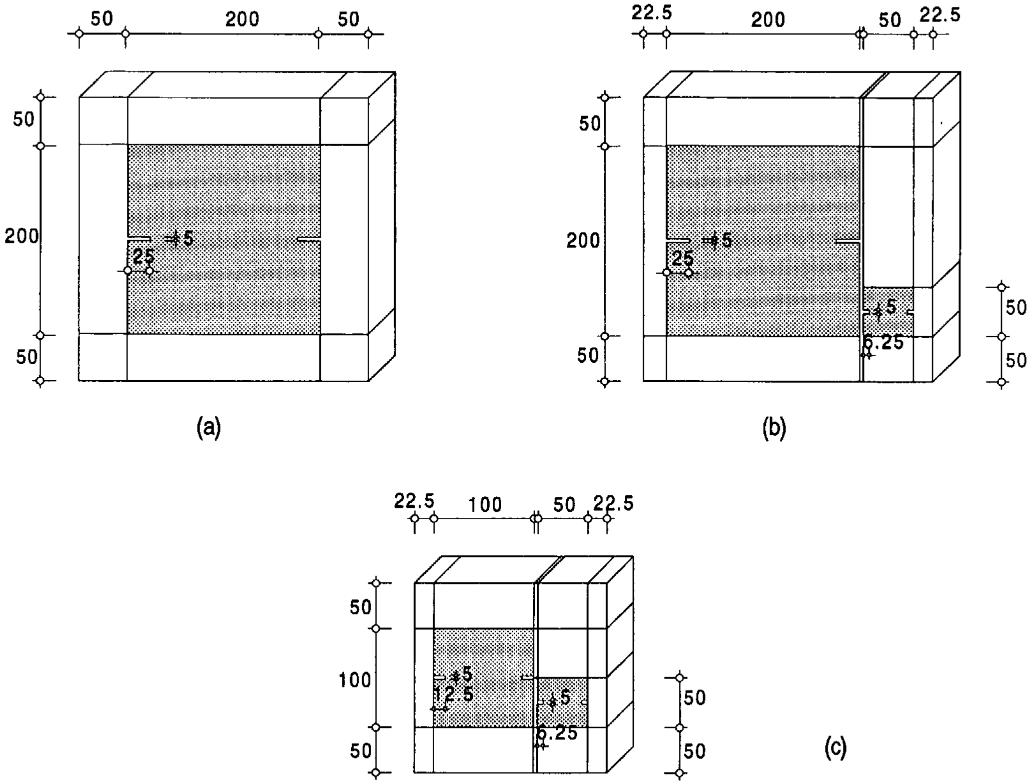

Figure 3.1 Sawing of DEN specimens from rectangular plates of 50 mm thickness.

3.2 Loading frame

In order to study the mixed-mode fracture of concrete several testing arrangements have been proposed. After a survey of equipment Reinhardt et al.[87] concluded that the existing testing arrangements were not suitable for obtaining the necessary data in a physically clear and independent way. Therefore, a new mixed-mode machine was developed at the Stevin Laboratory of Delft University of Technology. The main aim at that moment was to extend the fictitious crack model to a mixed-mode situation.

The loading frame, the data acquisition system, the extensometers and the substantial part of the test control system were developed and built by the Measurement and Instrumentation group of the Stevin Laboratory, except for the regulation system (SCHENK-hydropuls-PEZ 7111).

The mixed-mode machine consists of two independent stiff square loading frames. The exploded view of the machine is shown in Fig. 3.2. The outer frame A is a coupled frame and it is capable of moving along the horizontal direction. The inner frame B can also move along the vertical direction. Moreover, frames A and B can move independent of one another. The outer frames and the inner frame are fixed to the overall frame via 8 vertical and 4 horizontal plate springs as shown in Fig. 3.3. The required assumption is that the plate springs prevent the frames from rotation. They have a limited bending capacity (1 N = 1.08 μm/m). On each side of the plate spring two strain gauges are mounted and connected in a full Wheatstone bridge configuration (6 Volt potential) to the data acquisition system. Any eccentricity which may occur during a test in the frame assembly could be traced back from the plate spring readings. Two hydraulic actuators (A,B) and two load cells (A,B) are situated outside the loading frames in order not to hinder the overall stiffness of the loading frame. The frame assembly is shown in Fig. 3.4.

The specimen was fixed to the double and single frame using F-88 (Tridox) self-curing non-epoxy plastic adhesive cement. To properly glue the specimen into the machine there must be enough space surrounding the specimen. There are two types of displacements possible in the frame. A large displacement to the frames can be inflicted via roller bearing units connected to guiding bars (Fig. 3.5). The roller bearing guiding unit was blocked

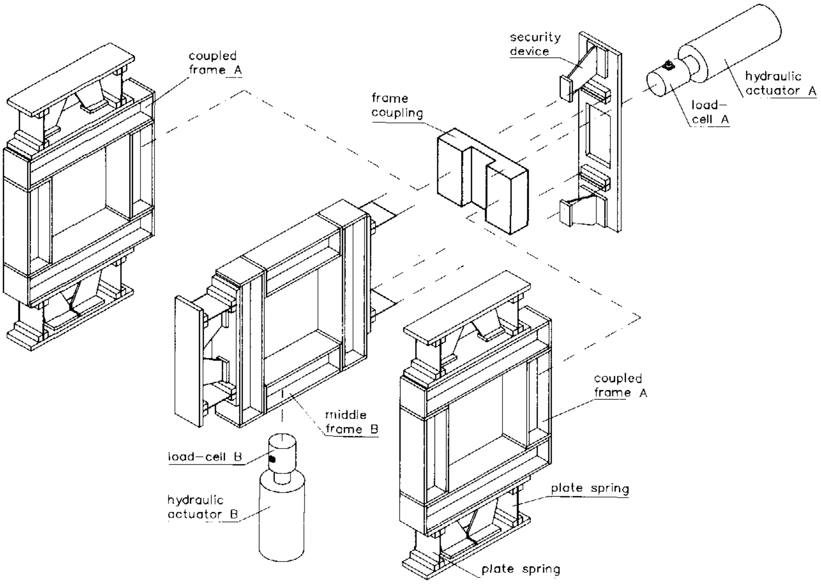

Figure 3.2 Exploded view of the loading frames.

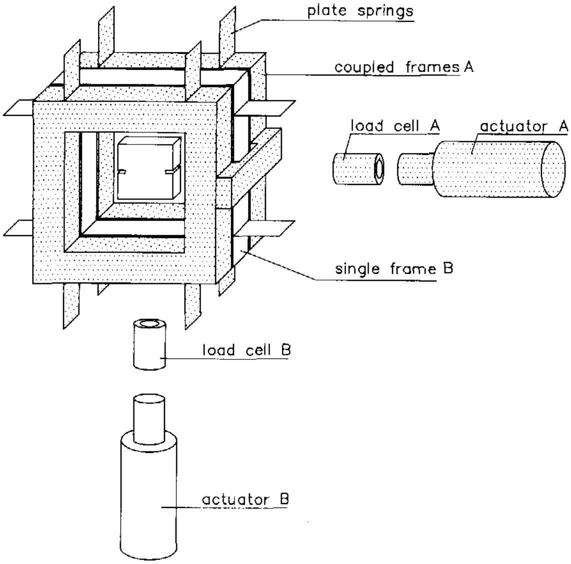

Figure 3.3 Another view of the loading frames, combined situation.

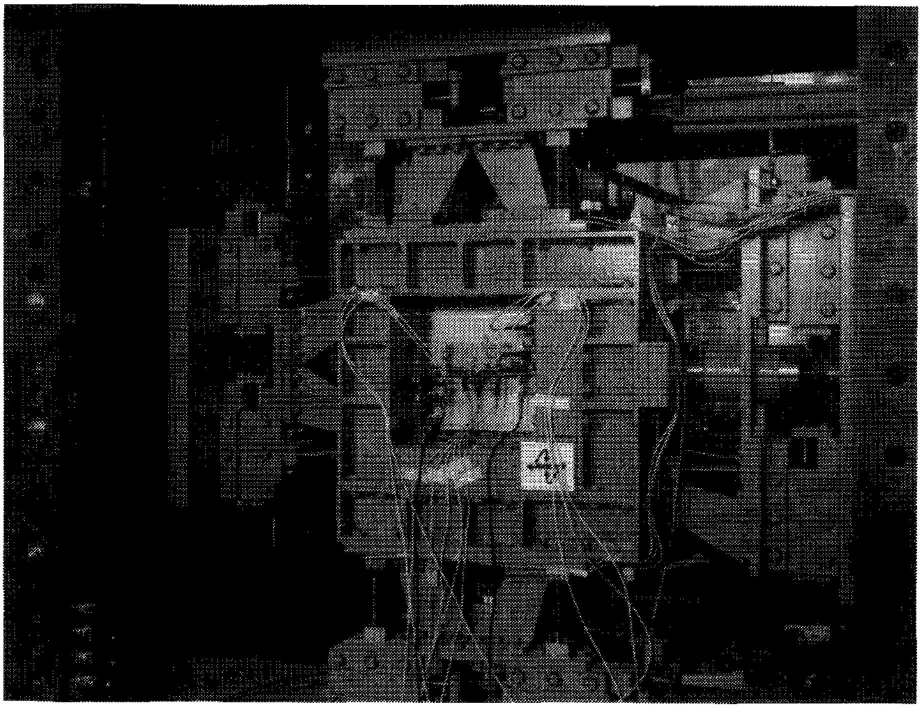

Figure 3.4 Photograph of the mixed-mode frame assembly.

during the execution of a test, and small displacements were possible due to the plate springs which have a limited bending capacity. To glue the specimen into the machine, a small compressive force (±5 kN) was applied. After the specimen was properly glued to the loading platens, and the adhesive was allowed to set for approximately 90 minutes, the roller bearing units of the double and single frames were fastened using bolts. Damage to the plate springs due to an undesirable movements of the frames is prevented through several security devices which are made of steel plates as shown in Fig. 3.2.

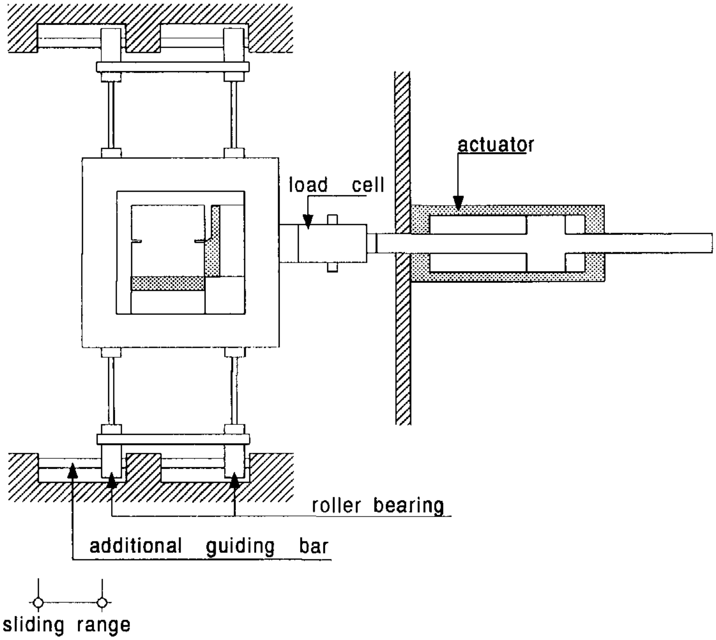

Figure 3.5 Roller bearing guiding unit for large displacements of the frame.

In Figs. 3.6a and b, the sectional view of the loading frame is shown in two stages. Here a Double-Edge-Notched (DEN) specimen is glued to the frames. As can be seen from the figures, the top of the specimen is glued to the inner frame and the bottom of the specimen to the coupled outer frame. The inner frame can slide in between the coupled frame as shown in Fig. 3.6a. The specimen is loaded by moving the middle frame upward. A tensile stress develops in the concrete specimen, because the coupled outer frames are fixed in the vertical direction. A tensile crack always nucleates in the notched region which is located at the half height of the DEN specimen (Fig. 3.6b), so that crack evolution can be followed at a known location. This enables deformation controlled testing. In Fig. 3.6b, bending of the horizontal plate spring is indicated after the crack formation in a DEN specimen.

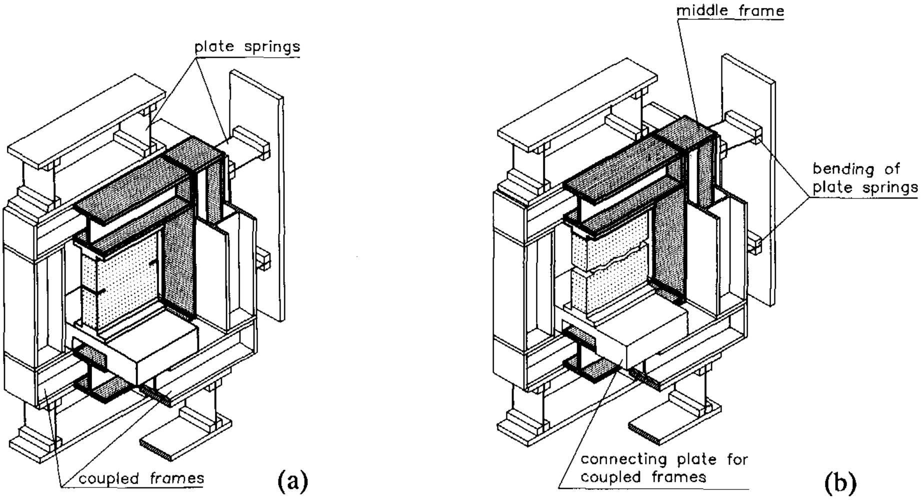

Figure 3.6 Sectional view of the mixed-mode loading frames in two stages: (a) before and (b) after the speciemen is cracked.

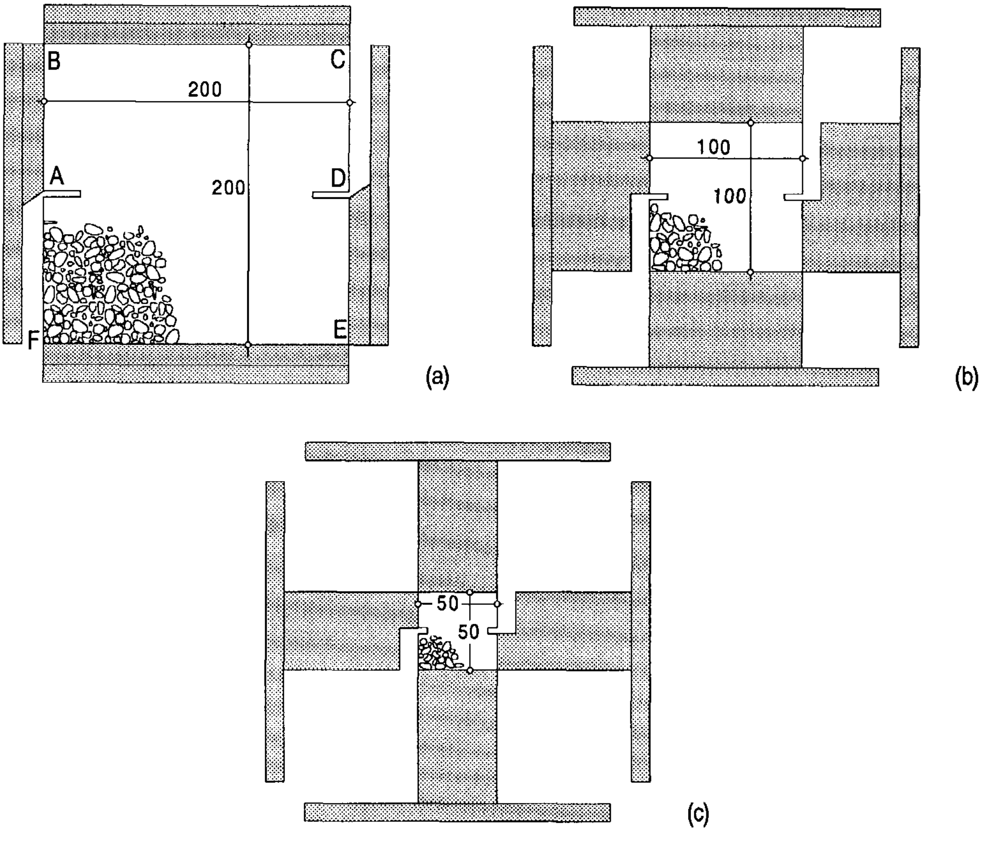

Figure 3.7 Glue platen assembly for 200, 100 and 50 mm specimens.

The DEN specimens are fixed to the frames via loading platens. For a uniaxial tensile test only two loading platens are required. However, for a biaxial test two additional loading platens are needed in order to apply a lateral in-plane shear load. They are glued to parts of the left and right edges of the specimen as shown in Fig. 3.7a. Moreover, the glue platens at the edges ABC and DEF of the 200 mm specimen are fixed to the inner and outer coupled frames. Any shear force acting at the specimen edge DE is counter balanced by the reaction exerted at the edge AB, since the inner frame is fixed along the horizontal direction. Some modification in the loading platen assembly is required in order to accommodate the specimens with two other sizes (100 and 50 mm) in the test rig. Accordingly, two different loading platen arms made of stainless steel were designed to fix the specimens into the frames as shown in Fig. 3.7b and c. Especially for the 50 mm specimen this results in rather slender loading platens. The influence of the loading platen arms in the specimen behaviour is not yet known. In Fig. 3.8 once again the loading platen arrangement is clarified through photographs. The assumed boundary condition for a DEN specimen is outlined in a schematic manner in Fig. 3.9. The boundary conditions allow for parallel end plate movement in the vertical and horizontal directions during the test.

3.3 Measuring system

The signals related to the movement of the two loading frames A (the outer frame, capable of moving in the horizontal direction) and B (the inner frame, which can move in the vertical direction) were connected to two independent regulation circuits 1 and 2 of the SCHENCK regulation system.

3.3.1 Load and displacement measurements

The machine contains two actuators and two load-cells as shown in Figs. 3.2 and 3.3. The capacity of the hydraulic actuators is 100 kN in compression and tension with a maximum stroke of 40 mm. The actuator is connected to the load cell via spiral washers. The capacity of the load-cell is restricted to 50 kN in the vertical and horizontal directions. The loads are measured using the calibrated load cells (40 μm/m/kN and 20 μV/V/kN) with four strain gauges in a full Wheatstone bridge configuration. The signals from the vertical and horizontal load cells were amplified via two standard amplifiers (SCHENCK MV 318) to the servo controllers. A 10 V signal corresponds to a load of 50 kN in both directions. The maximum load capacity is restricted to 50 kN because of the limited strength of the plate springs.

For the deformation measurements in the vertical directions, LVDTs (Sangamo, A6G1) with a gauge length of 65 mm were used. The position and the number of LVDTs

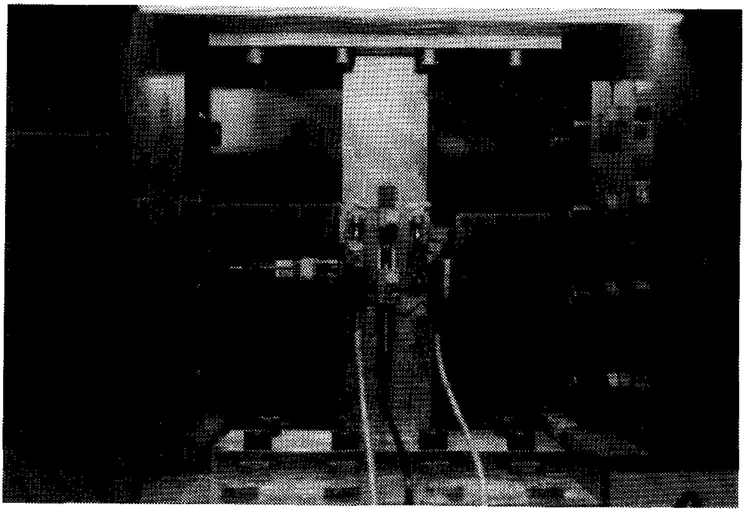

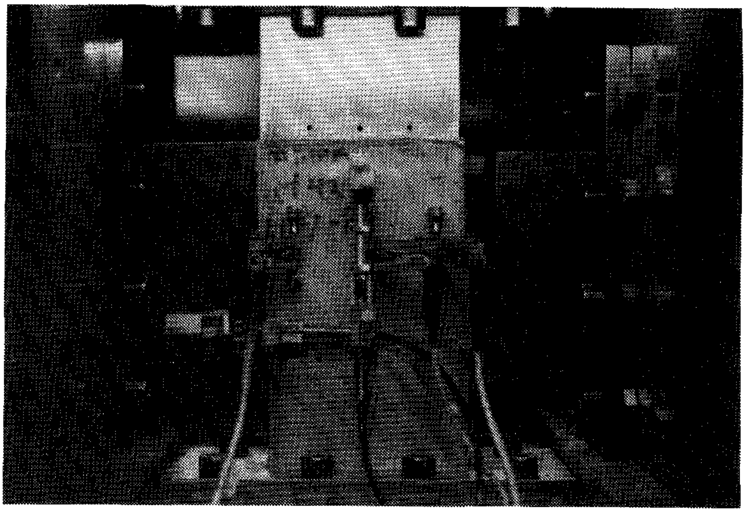

Figure 3.8 Photograph of the loading platen assembly for 50 and 100 mm specimens.

varied depending on the type of tests performed. In the early part of the investigation, in test series 14 to 18 (see Table 3.2), two vertical LVDTs were placed at the middle of the specimen, one at the front and the other at the rear face of the specimen as shown in Fig. 3.10. However, from test series 28 onwards four vertical LVDTs were placed, two on each face near the notch as shown in Fig. 3.11a. Due to a change in the load-path the fracture

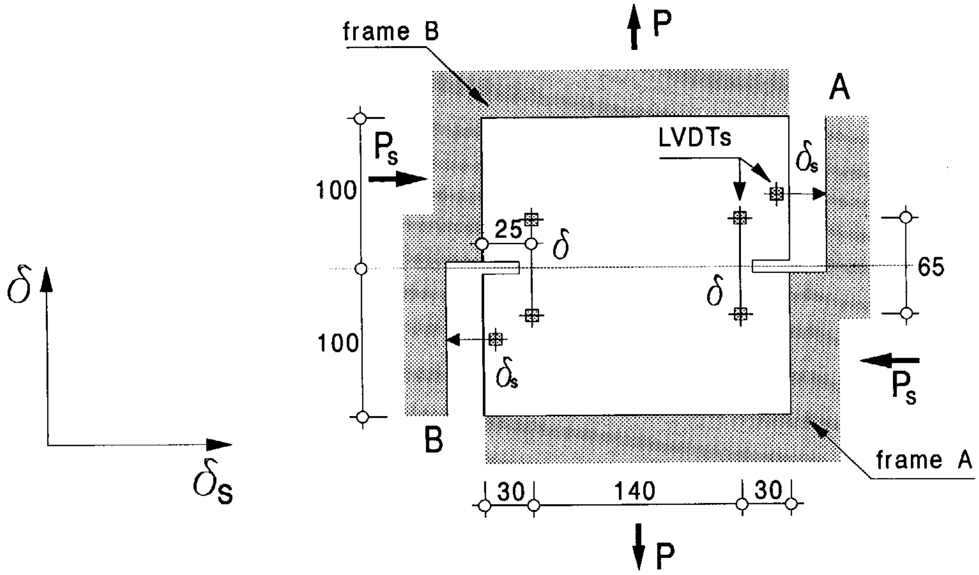

Figure 3.9 Boundary condition for a DEN specimen, subjected to combined tension and shear.

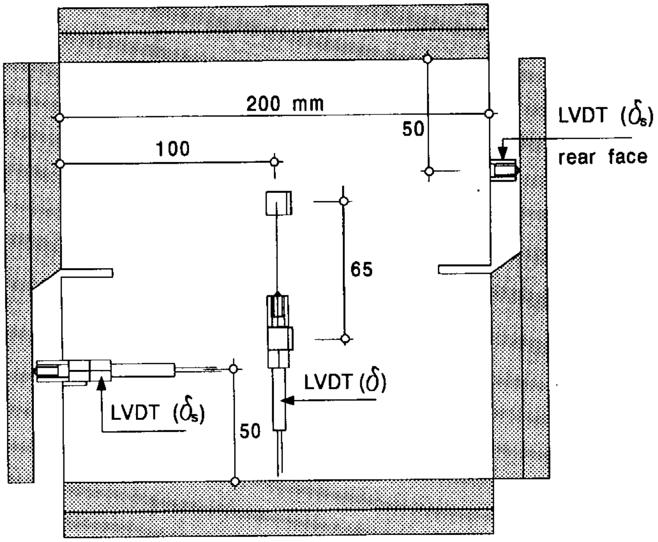

Figure 3.10 The arrangement of two vertical and two horizontal LVDTs on a 200 mm specimen.

mode changes and often the crack grows outside the control region once the LVDT is at the middle of the specimen. Therefore, it is required to place the LVDTs near the notch in order to obtain a stable test (for the 200 and 100 mm specimens only). Accordingly, for the 200 and 100 mm specimens, four LVDTs (gauge length = 65 mm), and for the 50 mm specimen two LVDTs (gauge length = 35 mm) were used. (see Fig. 3.11b,c). The LVDTs were calibrated using a device containing a Mitutoyo micro-screw with 0-50 mm movement and a 5μm accuracy. The LVDT has a linear stroke of ±1 mm with a nonlinearity of 0.3. (Calibration: a 10 V signal corresponds to 400 μm vertical/horizontal deformation). The photographs in Fig. 3.12 shows the front face of a 100 mm specimen in a fully instrumented situation.

For the lateral deformation measurements two LVDTs (Sangamo, A6G1) were used in the horizontal direction. At the front face of the 200 mm specimen, one LVDT was

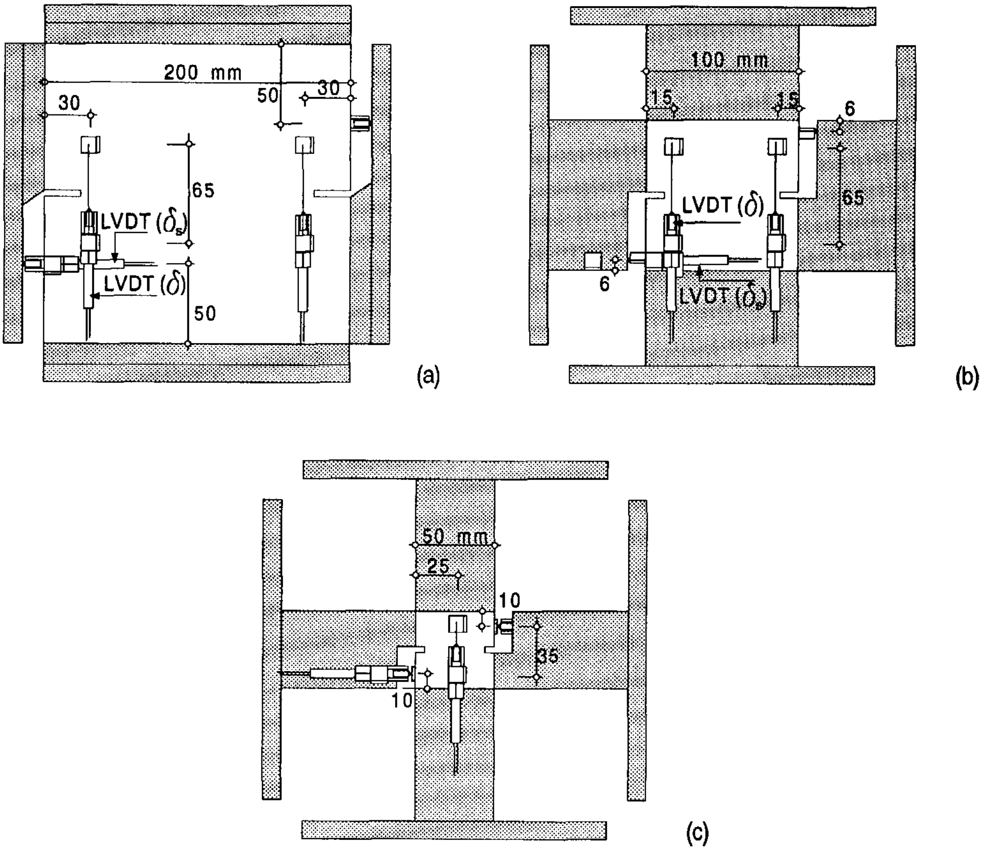

Figure 3.11 The arrangement of vertical and horizontal LVDTs for specimens of three different sizes.

mounted at the center of the bottom half as shown in Fig. 3.11a; the second LVDT was fixed to the diagonally opposite position at the rear face of the specimen. The global shear displacement δ_s was defined as the average displacement between the two halves measured by the two LVDTs. In Figs. 3.11b and c the positions of the horizontal LVDTs for the 50 and 100 mm specimens are shown.

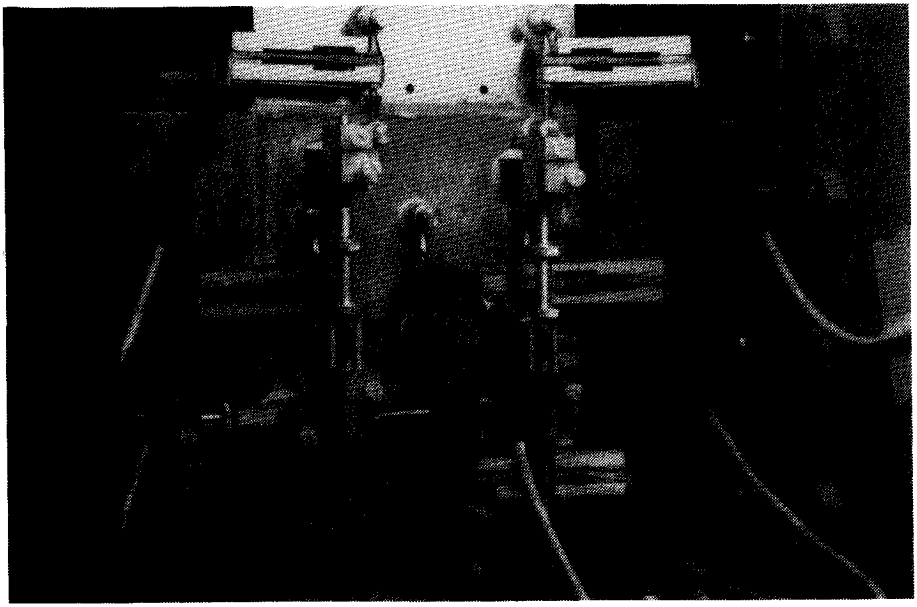

Figure 3.12 Photograph of a 100 mm specimen in a fully instrumented situation.

In addition to the LVDTs, a number of extensometers (mechanical- electrical transducers of the cantilever type (dimension 15x50 mm), developed and constructed by the Measurements and Instrumentation group of the Stevin Laboratory), were used to measure local deformations. To convert the mechanical displacement into an electrical signal, two strain gauges were used in this extensometer assembly as shown in Fig. 3.13. They were connected to the data acquisition system in a full bridge connection with a 6 V potential. The extensometer has a range of 0-2 mm, a resolution of 1 μm, a linearity of 0.5% and an accuracy of 5 μm. The same calibration device mentioned above was used to calibrate the extensometers. The number of extensometers used varied depending on the type of test and the size of the specimen.

For the local deformation measurements, a total of six extensometers (three extensometers at each face), with a gauge length of 35 mm were used as shown in Fig. 3.14a.

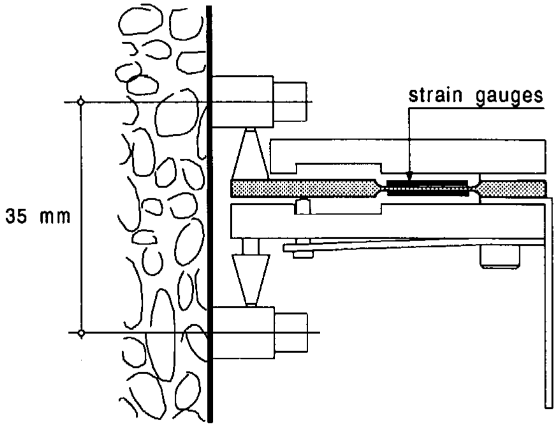

Figure 3.13 Schematized diagram of the extensometer; developed by the Measurement and Instrumentation group of the Stevin Laboratory.

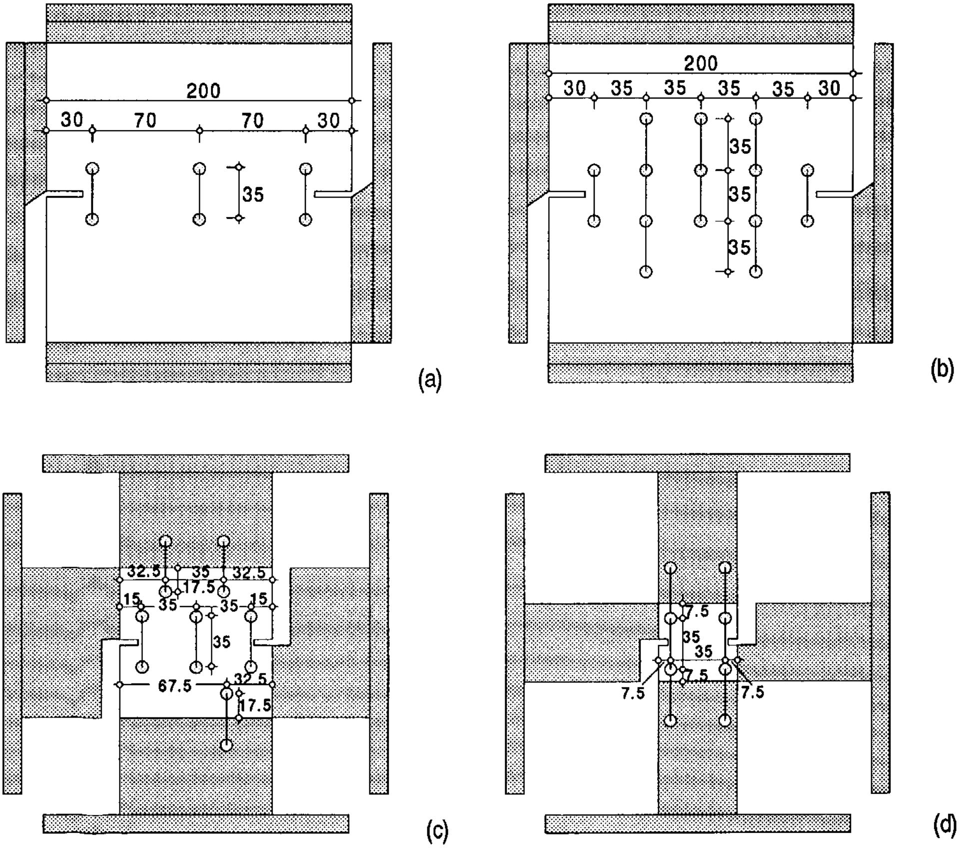

Figure 3.14 Extensometer arrangement for specimens of three different

(Corresponding to test series 14 to 32). However, for the test series with three different sizes (see Table 2), the number of extensometers used varied in order to capture the evolution of overlapping cracks which is the most dominant fracture mode for some load-paths.As shown in Fig. 3.14b,c and d, the number of extensometers used for the 200, 100 and 50 mm specimens were 20,14,12 respectively. In 50, 100 mm specimens additional extensometers were placed over the glue layers in order to record any crack initiation in the glue layer.

3.3.2 Test control

The SCHENCK loading installation as available at the Stevin Laboratory is an energy transmission system, that is, electric energy is transformed into hydraulic and regulatable mechanical energy. Eventually this mechanical energy can be used to load a test specimen. The loading can be applied to a specimen in a desired manner with a closed loop servo controlled system.

The hydraulic power is supplied to the loading installation through the hydraulic power package unit, which consists of an electrical motor, an oil pump cooler, a filter, electrical switches etc. The hydraulic power package unit regulates the oil in the main supply line at a pressure of 220 bar and a flow rate of 40 l/min. The hydraulic pressure unit and the total current is regulated by SCHENCK DU 312 unit. In case of an emergency this unit is capable of shutting off the hydraulic supply and the flow of current for the closed loop system. However, it is modified by the measurement group of the Stevin laboratory such that in case of an emergency only the hydraulic supply is terminated and the electrical current remains in the circuit. The purpose of this is to save the specimen to be tested from any damage due to the termination of the power supply. The SCHENCK steering monitor DP 317 controls the hydraulic supply from the main hydraulic line to the actuator. Also it is capable of linking the steering monitor to external devices such as a computer. In this manner a fully automated system can be built, capable of testing along pre-determined load-paths.

Testing can be either in load or in deformation control. For a stable uniaxial tensile test (stable crack growth), deformation control is essential. The mixed-mode machine has two independent frames connected to two independent regulation circuits, and it is therefore possible to control the vertical and horizontal deformations separately in a test. Moreover, tests can also be performed with deformation control in the vertical direction and load control in the horizontal direction and vice versa.

The average signal of the control LVDTs was amplified via a standard amplifier (SCHENCK MV 318, with possibilities of 1:1, 1:2, 1:5 and 1:10 magnification and a carrier frequency 5 kHz) to the servo controller unit. The servo controller-unit consisted of a two part unit, an adaptable digital controller (SCHENCK RA 311) and a standard control signal unit (SCHENCK FP 312). To this servo controller a function generator was connected. The function generator consisted of two identical linear time base generators A and B connected to the servo controllers of the circuits 2 and 1 respectively(Fig. 3.15). At the beginning of a test the function generator, generates the program signal f(t) [V/s] which represents the desired condition. In a deformation controlled test, the average vertical deformation w (in Volt) was used as the feedback signal. A comparison was made between the feedback signal and the program signal and a control signal was supplied by the servo-controller to the servo valve (type MOOG D-7030, $\Delta p = 70$ bar, flow rate = 5 l/min) through a power amplifier (SCHENCK RL 311). If the two signals are equal, the experimental condition corresponds to the programmed condition and the valve remains stationary. As soon as the feed back or the program signal changes, a control signal is generated and the discrepancy is corrected.

Depending on the type of test, the signals of either the average vertical deformation δ_S or the average global shear deformation ws can be used as the feed back signal in the closed loop servo control system. When the average signal δ_S is used, a comparison is made with the program signal from the generator B. Apart from that the principle is the same. Fig. 3.15 shows the schematic representation of the closed loop system.

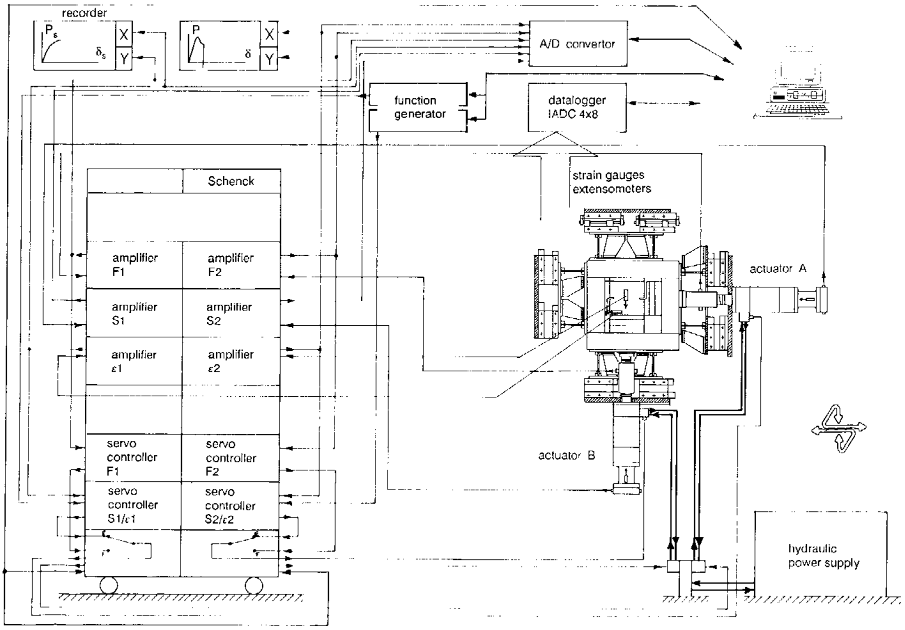

Figure 3.15 An overview of the biaxial testing arrangements.

3.3.3 *Data acquisition system*

The measurements during a test can be divided into three categories: (1) the load cells (vertical and horizontal), (2) the LVDTs (vertical and horizontal) and (3) the extensometers and strain gauges. All of these signals were in an analog form. First the signals from the load cells and the LVDTs were amplified to the SCHENCK regulation circuit and each of the output signals corresponding to two loads and two deformations (LVDT) were split into two. One part of the split signal was connected to a HP Vectra ES/12 personal computer via a 12 bit fast analog digital converter. The other part of the analog signal from the SCHENCK was connected to two plotters. The vertical load P and the vertical deformation δ were plotted on a XY recorder type HP-7046A and the lateral load P_s and the lateral shear deformation ws were plotted on a $X_tY_1Y_2$ recorder type PHILIPS PM-8132. Second, a 32 channel programmable data logger (designed by the Measurement and Instrumentation Group of the Stevin Laboratory) was used to retrieve the data from the extensometers and strain gauges. In this data logger, a sum of 32 individually programmable amplifiers (with a factor of 1, 10 or 100), four multiplexors and four integrating analog digital converters (maximum resolution 0.38 μV (18 bits)) were used. A 6 Volt bridge power was applied to either a full, half or quarter bridge Wheatstone configuration, with an internal resistance of 120 Ω. However, for the present data acquisition a full bridge configuration was used. The total scan time for 32 channels is 976 ms. A micro computer was required to program the data logger. Transmission of commands and data was provided by a simple RS 232 serial channel. The output from the data logger was stored on a floppy (0.7 MB).

Dedicated software was developed, which allowed fully automatic testing. The personal computer controls the datalogger, the SCHENCK regulation system, the A/D converter and the function generator as shown in Fig. 3.15. During a test scanning was done at fixed time intervals. The load was applied continuously, no stops were made for scanning of the measuring devices. The data logger was programmed to scan every 10 seconds from the beginning of a test, with the capability of changing the scan time (usually 30 to 60 seconds). The floppy can accommodate 600 scan steps, so that a change in scan time was required to include a complete test on a single floppy (0.7MB).

A typical scan consists of signals from two loads (P, P_s) [mV], two deformations (δ,δ_s) [mV], six to twenty extensometers [μV], and twelve strain gauges [μV] from the vertical and horizontal plate springs. However, the vertical and horizontal forces and deformations, the scan-number and the elapsed time were printed for each scan. Through a simple program the stored data were transformed into an advanced Symphony spread sheet format and the results of the test were obtained on the same day.

3.4 Experimental problems

When fracture properties of materials are to be determined, it is extremely important to have the desired boundary conditions. In almost all the tests, the plate boundaries were kept parallel to each other (Fig. 3.7). Concerning possible eccentricities of the machine, it was found that cracking always initiated at the front left notch, see Van Mier and Nooru-Mohamed[90]. As observed before, non-uniform crack opening is prevalent in heterogeneous materials such as concrete. Because of this, rotation of the frame is unavoidable even though stiff (in the direction of the load) plate springs were applied to avoid them.

3.4.1 Influence of glue platens

Fig. 3.16 shows the uniaxial P-δ diagram for two DEN specimens (200mm) glued between two and four loading platens respectively. The results indicate that the specimen 47-05 with two loading platens gives a higher tensile strength than the specimen 46-03 glued between four platens. This was consistent throughout the entire test series. Previous results showed the same trend Nooru-Mohamed et al.[90]. Gluing of the lateral loading platens results in a more eccentric loading on the specimen compared with the case of two glue platens. The specimen with two platens gave a sharp peak compared to the one with four platens which gave a rounded peak. Additional eccentricities may be created when a specimen is glued between four platens.

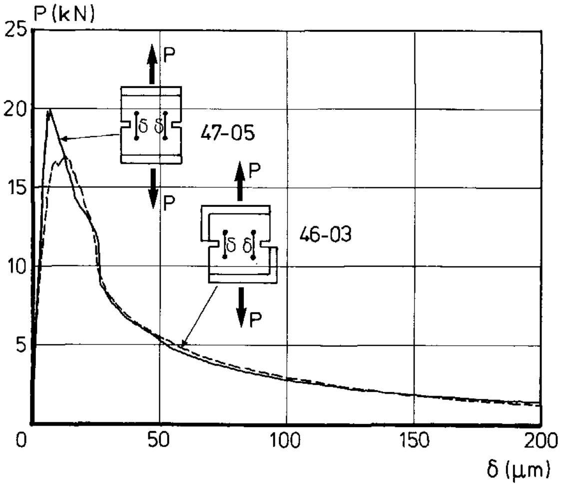

Figure 3.16 P-δ diagram for a two 200 mm specimens loaded in uniaxial tension.

The eccentricities that are caused by non-uniform cracking can be derived from plots of the local deformation δ_i versus the "global" deformation δ in Fig. 3.17. The axial load P was plotted in the same graph for the specimen with two loading platens. Numbers 1 - 8 correspond to 8 extensometers glued at the front and rear faces in order to measure local deformations. Fig. 3.17a, which gives the results for the specimen glued between two platens, show that the crack is initiated at extensometer 1 and subsequently at the locations of extensometers 5,2,6,3,7 and 8 (for example at $\delta = 10\mu m$). The eccentricity in the machine caused the crack to initiate at the left notch, at the location of extensometer 1. The deformation measurements demonstrate the non-uniform crack opening in uniaxial tensile tests and confirm the observations made by Van Mier[86] and Hordijk et al.[87].

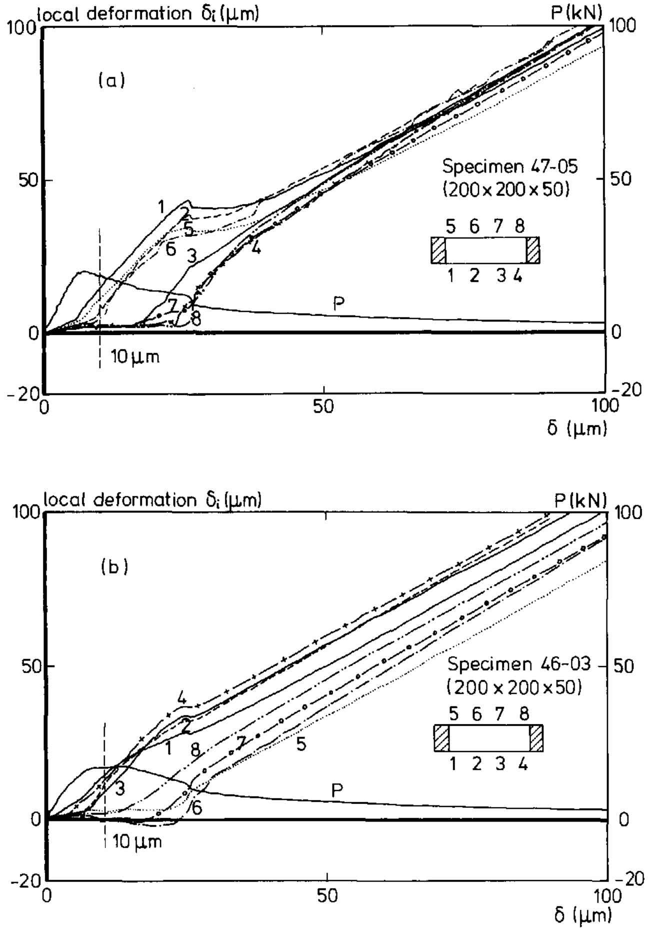

Figure 3.17 δ_i-δ plots for a uniaxial test with (a) two glue platens and (b) four glue platens (specimen size 200 mm).

A different phenomenon was observed in specimen 46-03 with four sides glued. Fig. 3.17b shows the δ_i-δ plot in which the fracturing process is completely different from that of specimen 47-05. In Fig. 3.17a the largest local deformation also occurred (for example at $\delta = 10\ \mu m$) at extensometer 1 as discussed before, subsequently large deformations occurred at extensometers 4, 2 and 3 between the first and the second load drop. However, extensometers 6 and 7 were in compression in this process, and it seems that out of plane bending occurred in this specimen.

From the above discussion it is obvious that the fracture evolution becomes different when the specimen is glued either between two or four loading platens. The effects of eccentricities in the frames seem more pronounced when four platens are glued.

3.4.2 Frame rotations

The frames in the biaxial loading rig can rotate in a number of ways. A possible situation is shown in Fig. 3.18, where the inner frame rotates and the outer frames are fixed. If this is the case, then the lateral shear deformation measurement δ_S defined as the relative horizontal displacement between the two frames, may include some part of the frame rotation. Therefore, it can not be concluded at this stage δ_S is the true shear deformation. In order to measure the in-plane frame rotation an independent frame of reference is required.

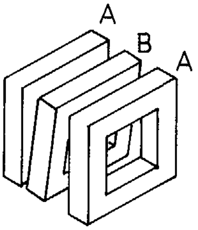

Figure 3.18 A hypothetical out-of-plane rotation of frame B with respect to frame A.

Initially, relative out-of-plane displacements of the frames were measured using four dial gauges as shown in Fig. 3.19. A 100 mm specimen (46-20) was glued in the machine between four loading platens, and four dial gauges were mounted (see Fig. 3.19). A lateral shear load P_S was applied to the specimen in displacement control until $P_S = -2.5$ kN; subsequently, the lateral test control was changed to load control and an axial tensile load was applied in displacement control. (This corresponds to the load-path 4 discussed in Chapter 4). Fig. 3.20 shows the gauge reading versus scan number for this test. In the same

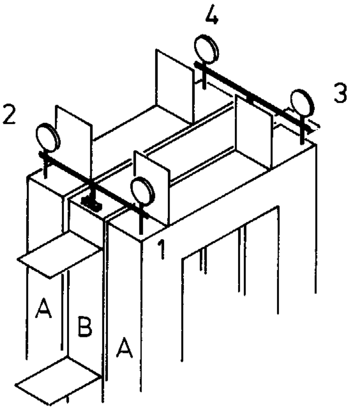

Figure 3.19 Location of the four dial gauges to measure the out-of-plane frame rotation.

graph, the lateral deformation δ_S and the vertical deformation δ are plotted. As can be seen in Fig. 3.20, δ_S is linear up till scan number 53 (see Fig. 3.20). During this stage, the gauge readings were almost zero except for gauge 1. This means that there is not much out-of-plane frame movement during the first shearing regime. However, as soon as the axial force is activated, the gauge readings differed significantly, which suggests that much of the frame

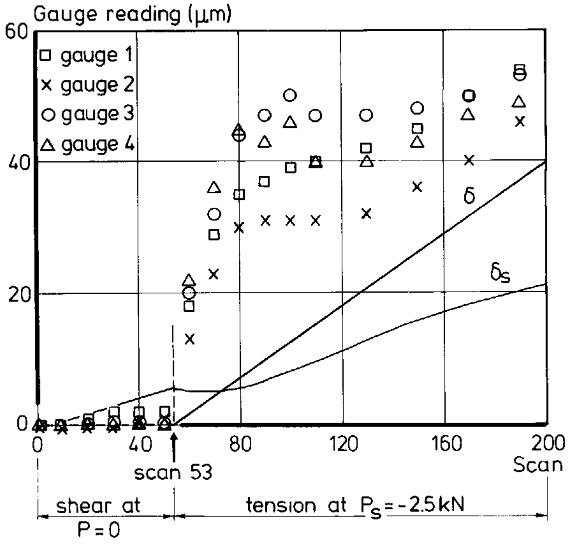

Figure 3.20 δ,δ_S and the frame movement measured by the dial gauges shown in Figure 3.19.

movement occurred during the initial period. The largest difference in gauge readings was recorded at the scan number 100 between gauges 2 and 3. This suggests that both the coupled frames, (front and rear) were not moving by the same amount with respect to the inner frame. Moreover, at the 100th scan the difference in local deformations on the specimen, corresponding to the position of the gauges 3 and 2 were the largest. At this stage, the movement of the frame more or less corresponds to the deformations in the specimen. In fact, it is not clear, whether the specimen follows the machine or vice versa.

3.4.3 Plate spring behaviour and the development of bending moments in the frame assembly

The plate spring assembly shown before in Fig. 3.3 is illustrated in Fig. 3.21. A total of 12 plate springs is shown, where RR1-RR8 and RR13-RR16 correspond to the vertical and the horizontal plate springs respectively. As shown in Fig. 3.21b and c, the top and the bottom of the DEN specimen is glued to frames B and A. Note, that the frame A can move along the horizontal direction, the frame B along the vertical direction. Suppose, that frame B is pushed along the vertical direction with a compressive force P, then the top of the DEN specimen is pulled with a tensile force of magnitude P_1. Subsequently, the bottom of the specimen is held back since it is glued to the frame A which is fixed in the vertical direction. Therefore, a tensile stress state arises in the specimen due to the action and the reaction caused by both frames. Considering the equilibrium of the frame B would lead to $P = P_1$, where P_1 is the reaction (Fig. 3.21d) inflicted on the frame B by the specimen. A similar reaction P_1 is also transmitted by the specimen to the frame A, see Fig. 3.21e. In order to maintain the frame A in equilibrium, the force P_1 needs to be balanced by the reactions evolved in the vertical plate springs. The four bottom plate springs RR5-RR8 elongate and impose tensile forces on the frame. However, the four top plate springs (RR1-RR4) are compressed due to the elongation of the bottom plate springs and exert compressive forces on the top of the frame. For the equilibrium of the frame A: P_1 = summation of the reaction loads of plate springs $[(RR5+RR6+RR7+RR8) + (RR1+RR2+RR3+RR4)] = P$.

In Fig. 3.22, the plate spring reaction versus vertical deformation (δ) is shown. The four bottom plate spring reactions RR5-RR8 are positive (tension) and the other four top plate spring reactions are negative (compression). The average peak reaction of the top and the bottom plate spring is -1 and 4 kN respectively. Therefore, the load distribution in the bottom and the top plate spring is 4:1. Suppose the axial load is P, then in an ideal situation each of the bottom and the top plate springs carries P/5 kN and P/20 kN. In reality this may not occur. In the pre-peak region, all four bottom plate springs had almost equal reactions. However, in the post-peak region, for example at $\delta = 20\mu m$, the reactions are not the same. Hence, the difference in the plate spring reactions leads to the occurrence of bending moment in the frame assembly.

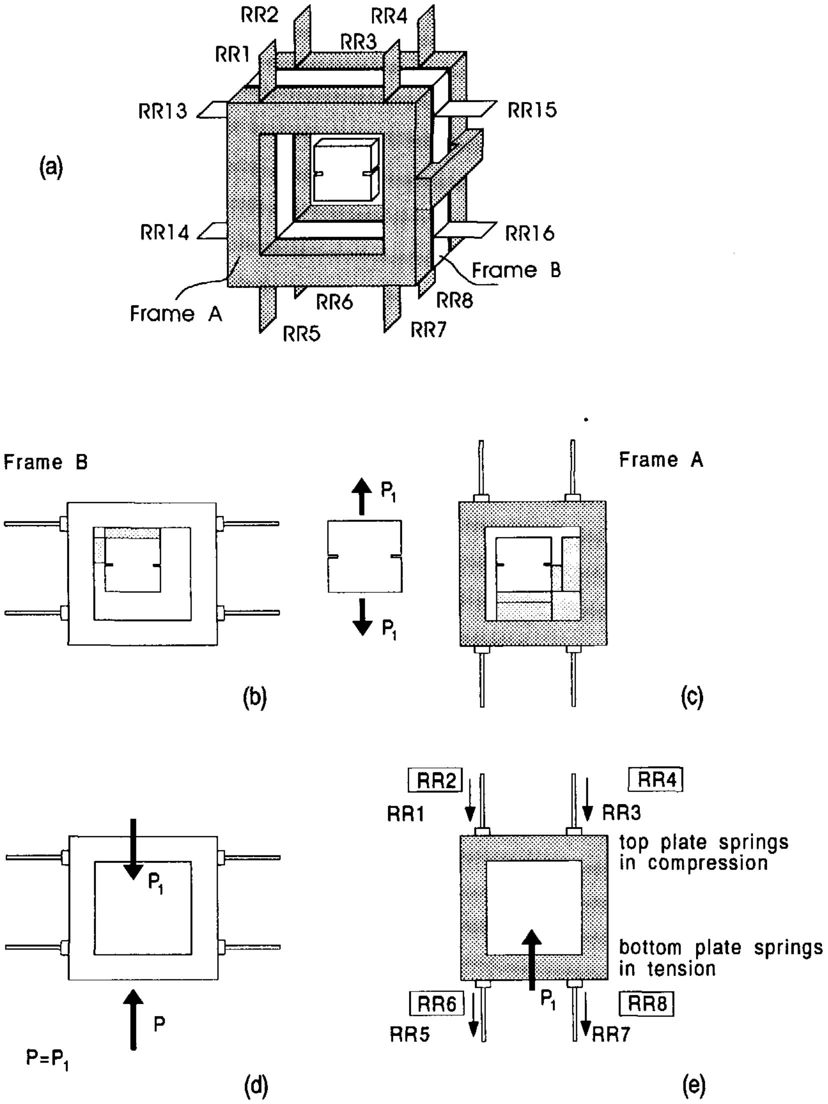

Figure 3.21 Plate spring assembly and the reaction loads in the vertical plate springs.

In Fig. 3.23a, the in-plane bending moments that arise due to unequal load distribution in the plate springs are schematically identified as M_1- M_4. The in-plane bending moment is computed based on the vertical center line of the specimen and always clockwise moment is assume positive. For example M_3 = Reaction(RR7-RR5)*320/2 N-m; where 0.32m is the horizontal distance between the plate springs RR5 and RR7.

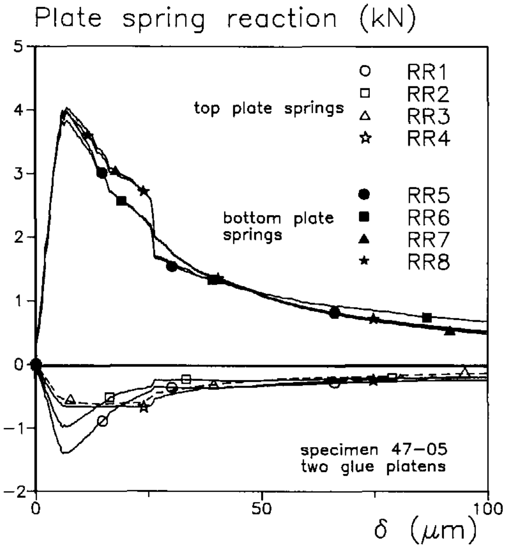

Figure 3.22 Reaction load in the vertical plate spring versus axial deformation.

The P-δ and the Moment-δ plots for a uniaxial experiment with two glue platens are shown in Fig. 3.23b. In the P-δ diagram three regions can be identified: (1) the pre-peak region, (ii) the post-peak region with non-uniform crack opening, and (iii) the post-peak region with uniform crack opening. In regions (i) and (ii) the top and the bottom bending moments vary in a number of ways. The largest bending moment was at the peak load (Fig. 3.23b). The first axial load drop occurred at $\delta = 27\,\mu$m, which corresponds to the end of the plateau in the P-δ curve. From $\delta = 27$ till 40 μm, the crack openings gradually became uniform and the δ_i - δ plots were parallel, see Fig. 3.17a. In this region the top and the bottom bending moments gradually decreased and moments M_1 and M4 reached a stable value aroune +20 and -20 N-m respectively while M_2 and M_3 attained zero.

The boundary condition in the DEN speciemen is such that the loading platens are forced to remain paralled during the test. This condition depends to a certain extent on the stiffness of the plate springs. In Fig. 3.22, the bottom plate springs showed equal load till the axial peak load, however, the top plate springs had unequal load distribution. This is also evident in Fig. 3.23b, in which M_1 and M_2 had the largest in-plane moment before the axial peak. In the post-peak region, during subsequent non-uniform cracking the load distribution in the plate springs became non-uniform and contributed to the existing in-plane moment.

From the local deformation measurements it was demonstrated that the crack initiation was at the front left notch (near measuring point 1, Fig. 3.17) for both specimens with

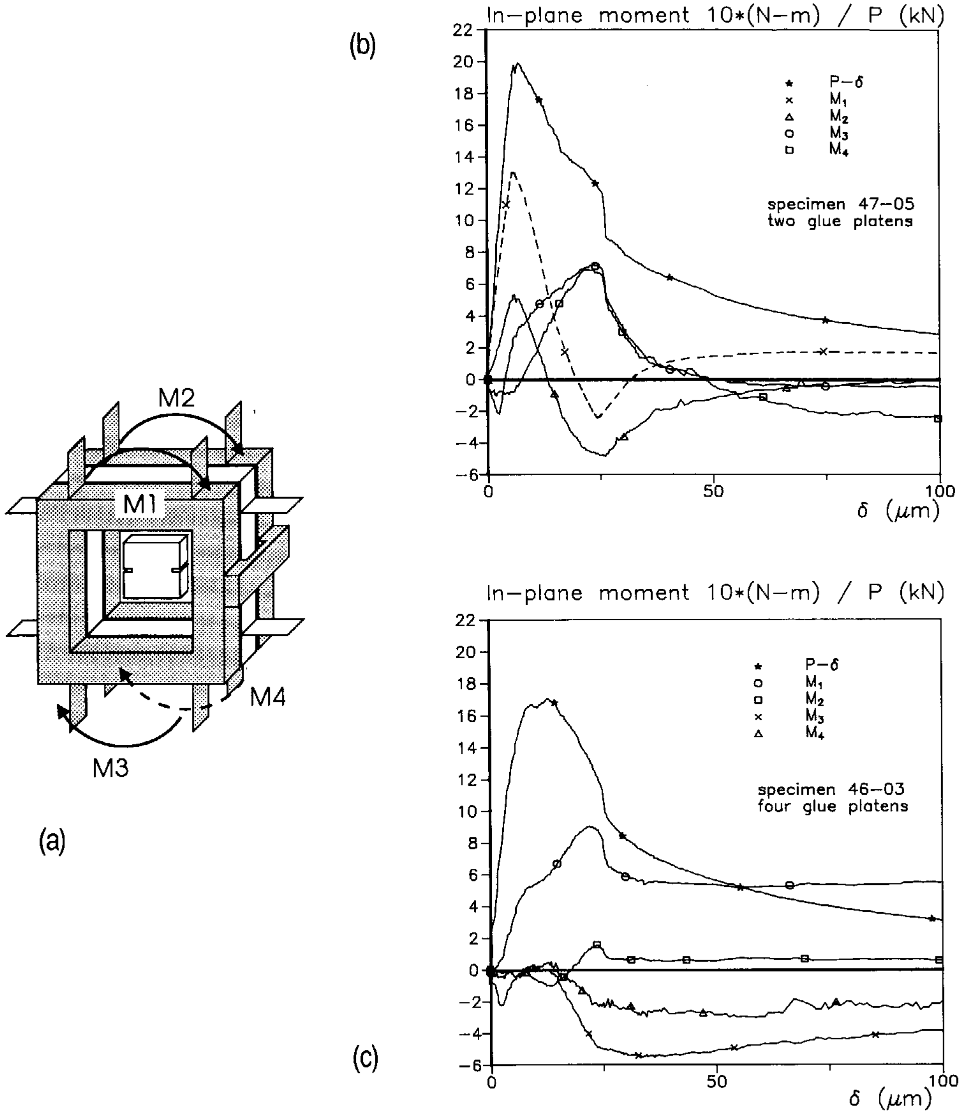

Figure 3.23 In-plane moment in the frames (a), P-δ and Moment-δ plots for specimen with two glue platens (b), and specimen with four glue platens (c).

two and four loading platens. Also note that in Figs. 3.23b and c, moment M_1 is the largest. However, the crack evolution was different in both specimens: through the specimen thickness in the case of two glue platens, and in the case of four glue platens first along the front face and subsequently on the rear face . From the local deformation measurements it was inferred that out of plane bending occurrred when four loading platens were glued.

In Fig. 3.23c the P-δ and Moment-δ plots for a uniaxial tension test with four loading platens are shown. Here moment M_1 was the largest too. In Figs. 3.23b and c, the difference in moment distribution in the two boundary conditions (two and four loading platen) can be seen. As shown in Fig. 3.23c, a variation in in-plane bending moment also occurred in the non-uniform crack opening region, however, the bending moments stabilized and maintained a constant value in the uniformly opened region.

In Fig. 3.24a, out-of-plane Moment - δ plots are shown. In the same figure, P-δ plot is also drawn. In Fig. 3.24b, the out-of-plane Moments are schematically shown. As can be seen in Fig. 3.24a, the largest out of plane moments were M_5 and M_7 corresponding to the right notch. Since M5 and M7 are external moments, internal moment in the outer plane of the specimen cause compression on the rear side and tension on the front side. This is the reason for observing compression in measuring points 6 and 7 (Fig. 3.17) on the rear face of the specimen.

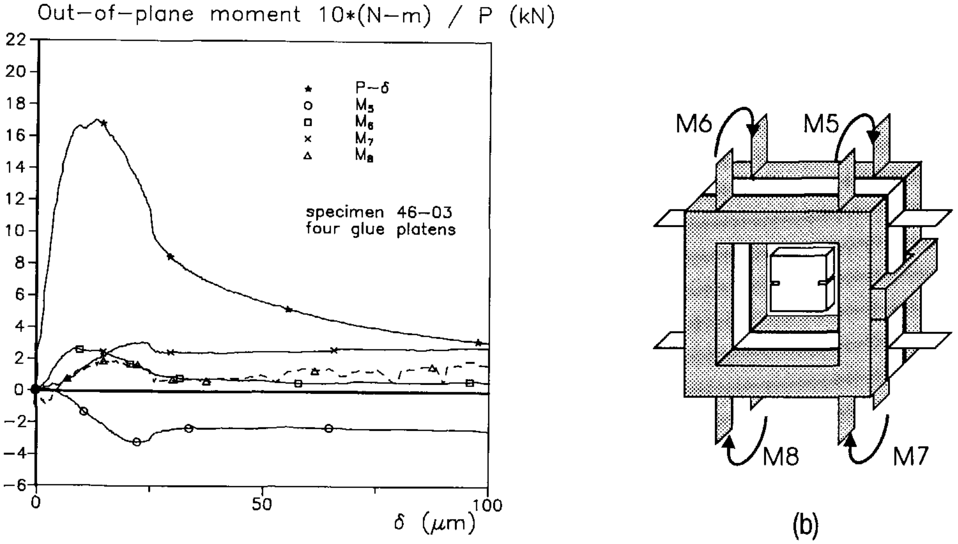

(b)

(a)

Figure 3.24 Out-of-plane moment versus axial deformation (a), and the schematic representation of the out-of-plane moments.

4 Experimental results and discussions

Introduction

Nucleation and growth of cracks under combined tension and shear are studied using the biaxial machine at the Stevin Laboratory. Seven load-paths have been examined in order to come to a better understanding of the underlying failure mechanism under biaxial loading. A unique feature of the biaxial machine is that any combination of vertical and lateral loads or deformations can be imposed.

The early mixed-mode studies at the Stevin Laboratory were launched with two aims: (1) to extend the fictitious crack concept of Hillerborg and co-workers (Hillerborg et al.[76]) to a mixed-mode situation, and (2) to obtain the aggregate interlock results for relatively small crack openings. For these purposes, push-off specimens were used by Reinhardt et al.[89] in order to obtain shear stress-shear deformation (τ - δ_s) relations for various crack openings(δ). They presumed that the stress distribution in the critical cross-section of the specimen was uniform. This made them choose push-off specimens with a certain notch depth to specimen width (a/d) ratio. Due to the heterogeneity of the concrete, non-uniform cracking already occurred in specimens subjected to uniaxial tension as discussed before in section 3.4. For this reason the push-off type specimens were abandoned and specimens were studied with a larger concrete cross section than originally intended. Another reason is that the concept of shear in push-off specimens is not clear enough, see Watkins & Liu[85]. The final crack pattern obtained in push-off specimens is of an S-shape. This suggests that tensile stresses play a dominant role. Keeping the above facts in mind, DEN specimens were chosen for the present studies. Another advantage of the DEN specimens is that a larger concrete cross-section is available between the notches for fracture evolution studies. By adopting such a geometry cracking processes, including all related non-uniformities could be studied much better. Furthermore, eccentricities in the loading equipment could be detected in a better way.

4.1 Load-path description

The following terminologies are used in this chapter.

Tensile and Compressive Shear: In this thesis, a shear force is called *tensile shear* when the lateral shear force is as shown in Fig.4.1a. Similarly, it is called *compressive shear* when the lateral shear is as shown in Fig. 4.1b.

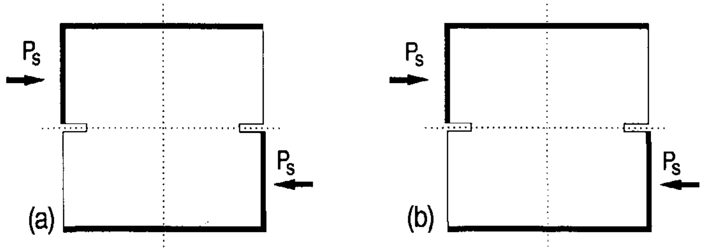

Figure 4.1 Definition of (a) Tensile shear, and (b) Compressive shear.

Crack Opening: Suppose that the total deformation over the gauge length measured across a crack is δ, then it can be subdivided into an elastic part δ_{el} (between the gauge length) and a true crack opening w, such that $\delta = \delta_{el} + w$. Nevertheless, when referring to the crack opening in this thesis, it will be implied that no correction was made for the linear elastic deformation mentioned above.

In Fig. 4.2, the various load-paths pursued in this study are shown schematically in terms of P-P_s, P-δ and δ-time diagrams.

Load- path 0: *Uniaxial tension* (Fig. 4.2a).

In this case, the specimen is glued between loading platens and is subjected to an axial tensile force P. With regard to the gluing of the loading platens two cases are distinguished: (1) two loading platens are glued on the top and the bottom of the specimen respectively (Fig. 4.3a), and (2) four loading platens are glued with two as above and the other two at diagonally opposite edges of the specimen as shown in Fig. 4.3b.

load-path 1:(a) *Compressive shear at a constant crack opening* (Fig. 4.2b).

The specimen was first loaded in axial tension to an arbitrary point in the descending branch. Subsequently, the crack opening δ was kept constant, and a lateral compressive shear load P_s was applied for different axial crack opening. In the axial direction deformation control and the lateral direction load control were used.

(b): *Tensile shear at a constant crack opening* (Fig. 4.2c). In this load-path everything was the same as in load-path 1(a) except that instead of a compressive shear, a lateral tensile shear load was applied.

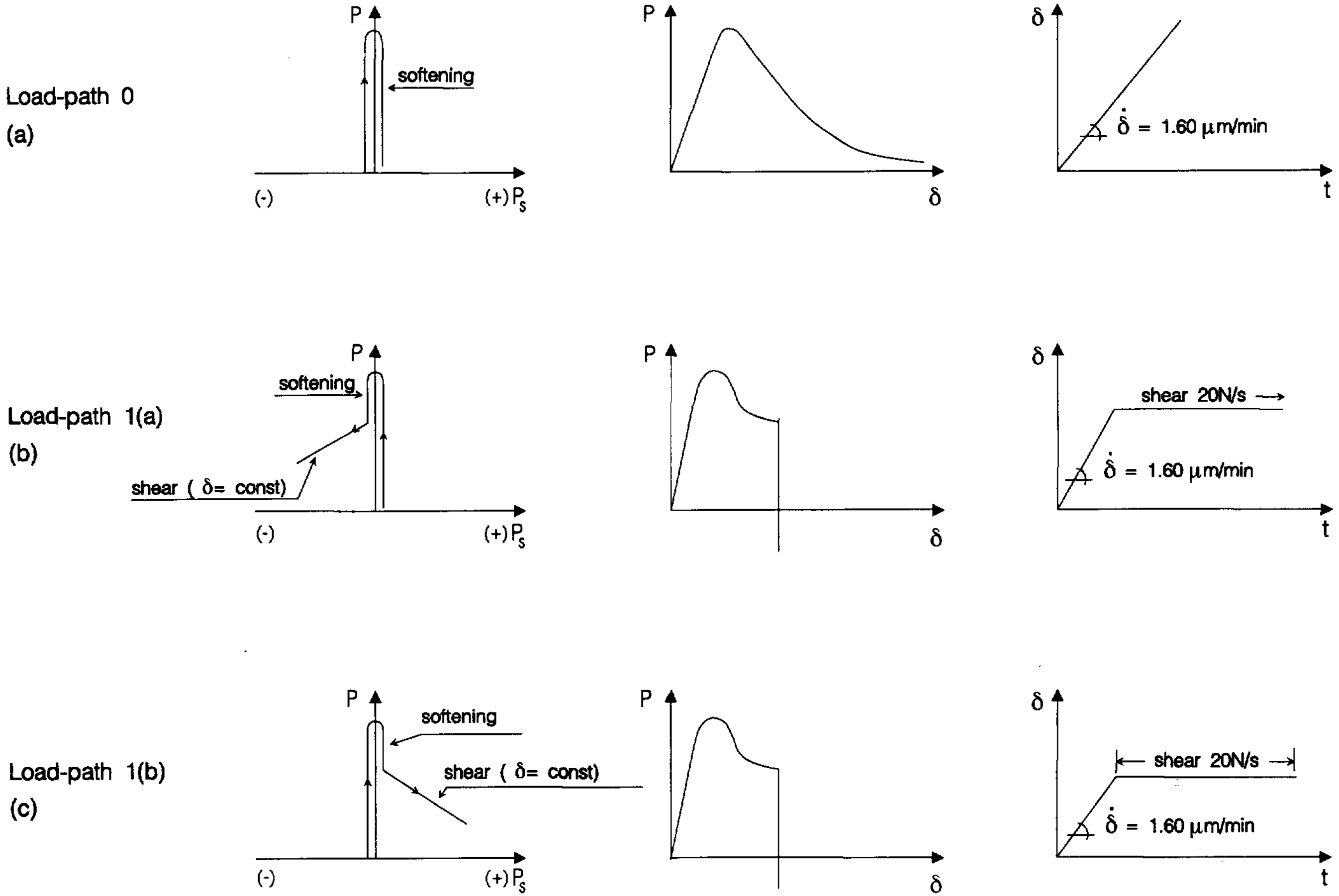
Load-path 0
(a)
P
softening
(-)
(+) P_s
P
δ
δ
$\dot{\delta}$ = 1.60 μm/min
t
Load-path 1(a)
(b)
P
softening
shear (δ= const)
(-)
(+) P_s
P
δ
δ
shear 20N/s →
$\dot{\delta}$ = 1.60 μm/min
t
Load-path 1(b)
(c)
P
softening
shear (δ= const)
(-)
(+) P_s
P
δ
δ
shear 20N/s
$\dot{\delta}$ = 1.60 μm/min
t

Load-path 2
(d)

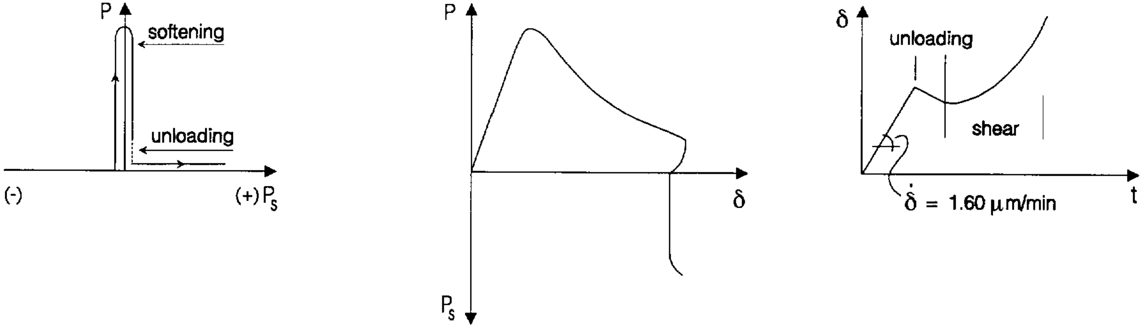

Load-path 3(a)
(e)

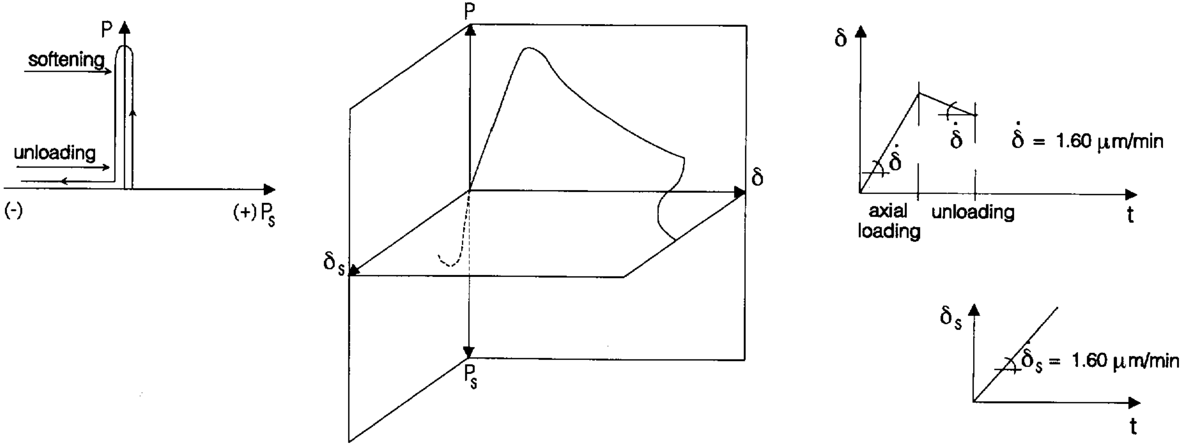

Load-path 3(b)
(f)

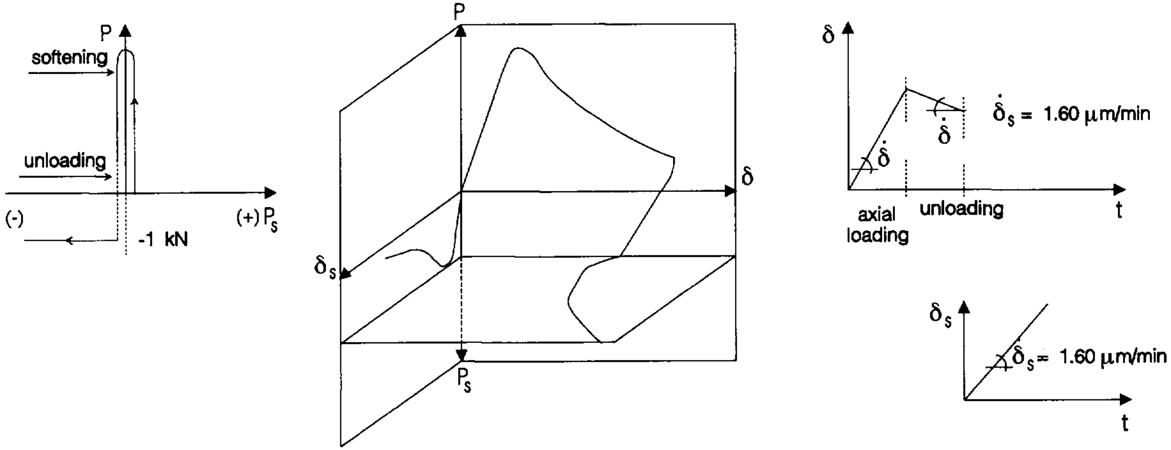

Load-path 4
(g)

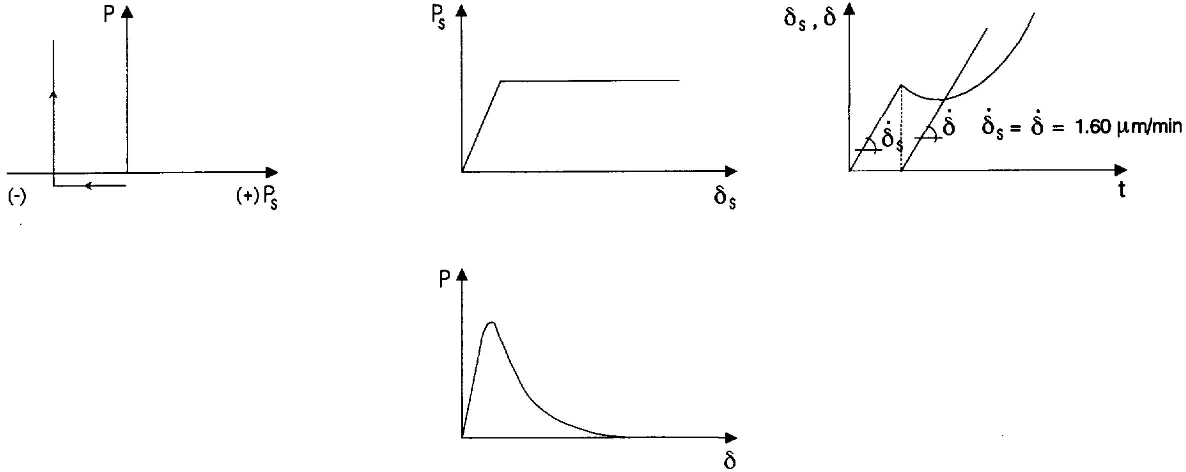

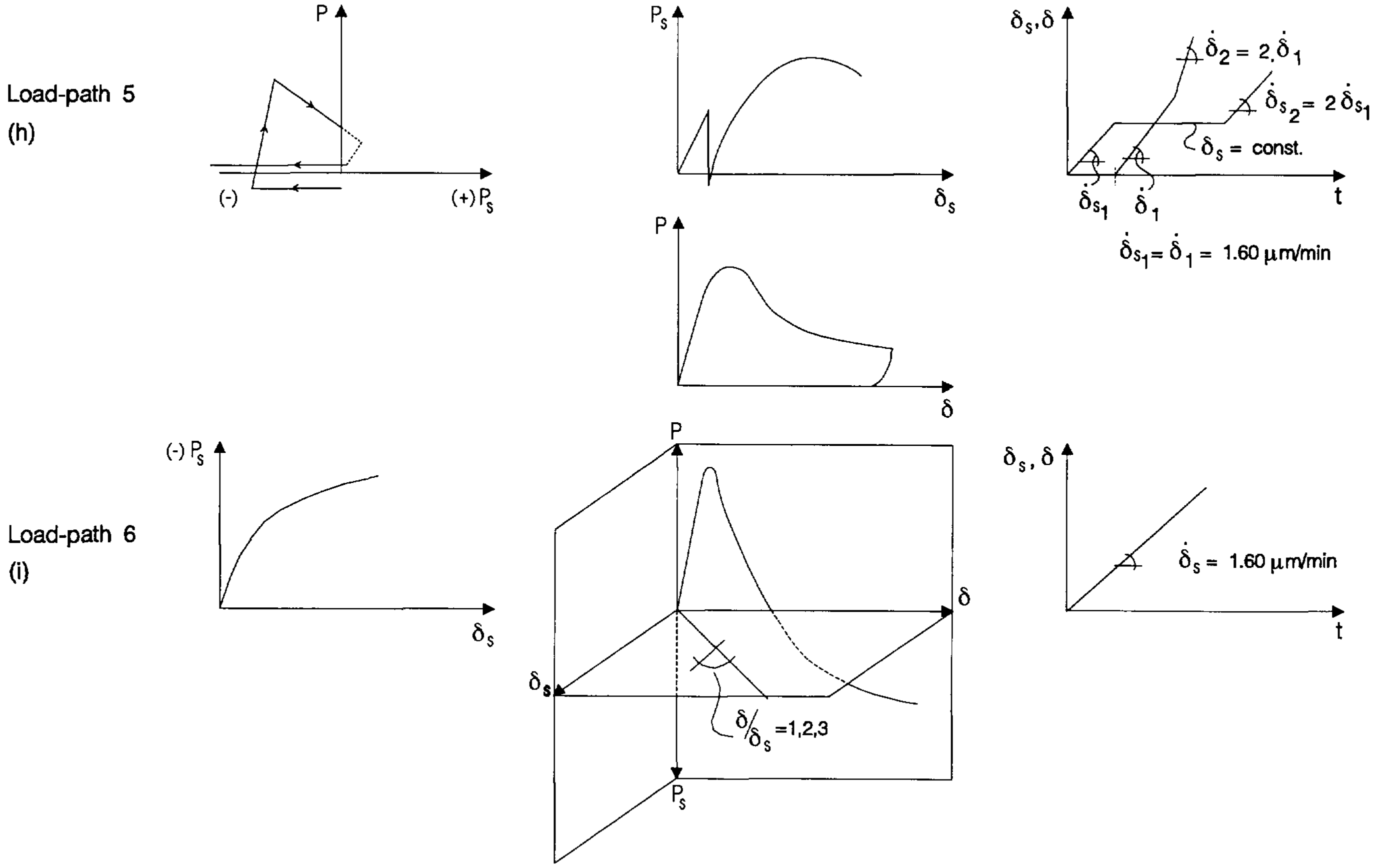

Figure 4.2 Schematic representation of the load-paths pursued.

Load-path 2:*Tensile shear at zero axial load ($P=0$)*(Fig. 4.2d).

The specimen was first subjected to tension, in displacement control. After loading to a prescribed axial crack opening, the specimen was unloaded until $P=0$. Subsequently, the test control was changed from displacement control to load control. Following this unloading, a lateral tensile shear load P_S was applied to the specimen in load control maintaining $P=0$ constant.

Load-path 3:(a) *Compressive shear at zero axial load ($P=0$) (Unconfined shear) (Fig. 4.2e).*

The specimen was pre-cracked to a prescribed average crack width δ. Subsequently, the specimen was unloaded in the axial direction until $P=0$, and the axial test control was changed to load control. Next, a compressive shear was applied in displacement control.

(b) *Compressive shear at a constant axial confinement ($P=-1000$) (Confined shear)(Fig. 4.2f).*

Here, the procedure was identical to that of load-path 3(a). The only exception is, that shear load was applied while the axial load was kept constant at $P=-1000$ N (average σ=-0.13 MPa).

Load-path 4: *Axial tension at a constant shear force*(Fig. 4.2g).

(a) *Shear force $P_S= -5$ kN.*

A compressive shear load P_S was applied to the specimen in displacement control until $P_S= -5$ kN. During the first shearing regime, a zero axial load ($P=0$) was maintained while the vertical deformation is free to move. Subsequently, the lateral test control is changed to load control and an axial tensile load is applied in displacement control till failure.

(b) *Shear force $P_S= -10$ kN.*

In this case the procedure is completely identical to that of load-path 4a except that the shear load P_S is equal to -10 kN.

(c) *Shear force $P_S=$ maximum shear.*

Here, everything is similar to load-path 4a except that the shear load P_S was equal to the maximum shear load the specimen could sustain.

Load-path 5: *Axial tension at a constant shear deformation*(Fig.4.2h).

(a) *Shear force $P_S= -5$ kN.*

This load-path is similar to load-path 4 except that in both directions (axial and lateral) displacement control was maintained. Here, P_S was applied first and at P_S = - 5 kN the axial load was activated while maintaining displacement control in both directions.

(b) *Shear force P_S = -10 kN.*
Again this is identical to load-path 5a except that the maximum shear was -10 kN.

(c) *Shear force P_S = maximum shear.*
This too is identical to load-path 5a except that the shear force was equal to the maximum shear load the specimen could sustain.

Load-path 6: *Proportional loading (Fig.4.2i).*
(a),(b) and (c) An axial tensile and a lateral compressive shear load were applied to the specimen such that the ratio of axial (δ) to lateral deformation (δ_S) remains constant throughout the test. The δ/δ_S ratio for load-path 6a,6b and 6c were 1.0, 2.0 and 3.0 respectively.

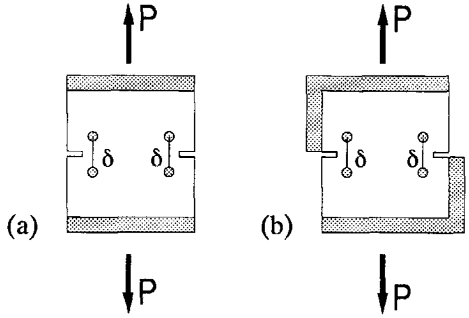

Figure 4.3 Two (a) and Four (b) loading platens in a load-path 0 (uniaxial tenslile) test.

4.2 Compressive shear versus Tensile shear

A significant difference exists between the final crack geometries and the mechanical strength of a specimen due to the choice of a compressive or tensile force. In the following paragraphs this aspect is addressed.

lateral compressive shear at a constant δ; load-path 1a
Results of tension-compression tests for 200 mm DEN specimens are shown in Figs. 4.4, 4.5, 4.6. In Figs. 4.4a and 4.5, the axial load-displacement diagrams P-δ, and the load-paths P-P_S are shown for specimens 14-01 and 14-02. The crack pattern corresponding to specimen 14-02 is shown in Fig. 4.6.

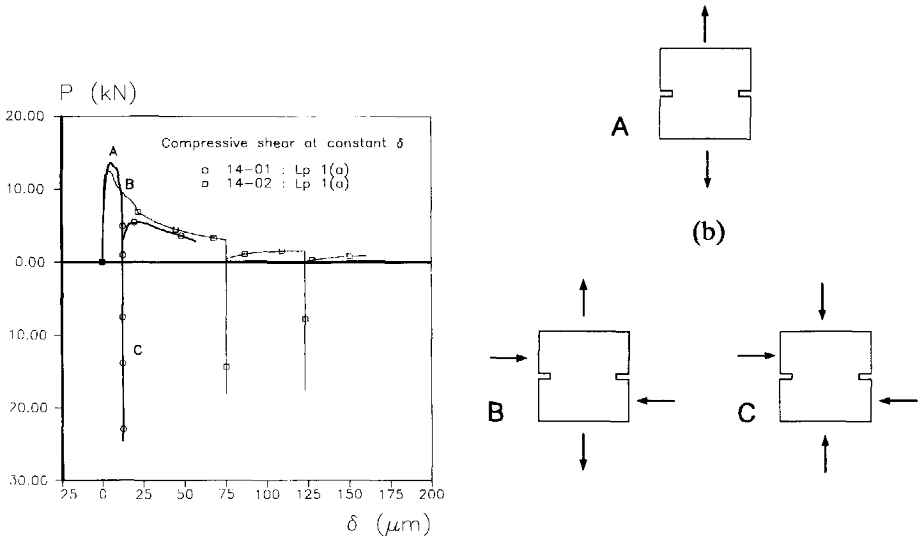

(a) (b) (c) (d)

Figure 4.4 P-δ response (a) and the loading sequence; tension (b) tension-compression (c) and compression-compression (d) in the load-path 1(a) experiments.

In Fig. 4.4a, changes in the loading sequence are clarified for this load-path with compressive shear. As shown in Fig. 4.4a, the specimen (14-01) was loaded in uniaxial tension up to point B. Subsequently, at point B on the descending branch, a compressive shear was applied under a constant deformation (i.e., a constant crack width). The vertical deformation δ is the average of the two LVDTs mounted at the front and rear faces of the specimen centers. By keeping the crack width at a constant value during the shear load, a compressive reaction developed in the axial direction. As can be seen at points A, B and C on the P-δ plot (Fig. 4.4a), the specimen was subjected to tension (Fig. 4.4b), tension-compression (Fig. 4.4c) and compression-compression (Fig. 4.4d) during the loading regime. Due to the restriction of the machine, the maximum lateral compressive shear (P_S) was 50 kN, but the specimen could carry a higher shear load than 50 kN. At point C a clear biaxial compressive stress state has evolved in the specimen as shown in Fig. 4.7. For example the maximum axial (P) and lateral (P_S) load reached before unloading the specimen (14-01) was -24.6 and -48 kN respectively. It is impossible to fail the specimen at these load levels. Failure would occur only when the biaxial strength envelop is reached.

As can be seen in Fig. 4.4a, at $\delta = 12.5\,\mu m$ and 75 μm, the lateral compressive shear force was applied for specimens 14-01 and 14-02 respectively. In both specimens, the lateral shear load P_S was unloaded when P_S was close to 50 kN. As soon as P_S = 0, the axial force was activated for the second time. During the subsequent axial loading, both specimens reached their original envelop curves (P-δ). Therefore, it is concluded that the lateral compressive shear has little effect on the axial capacity of a partially cracked specimen.

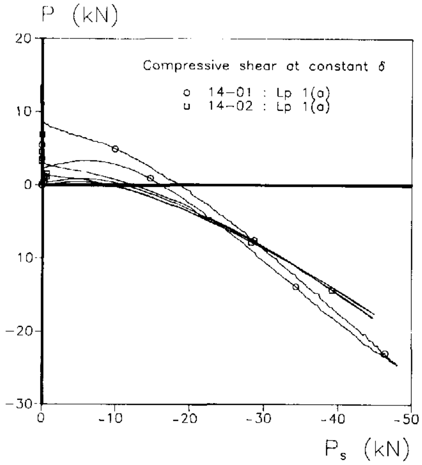

Figure 4.5 P-P_S relation for the load-path 1(a) experiments.

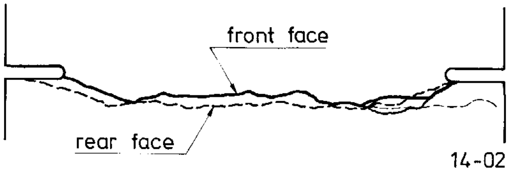

Figure 4.6 Crack pattern for the specimen 14-02, load-path 1(a) experiment.

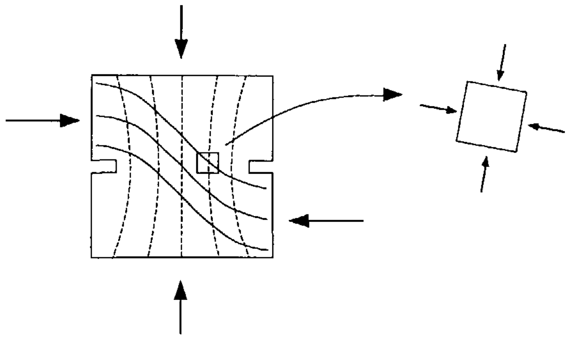

Figure 4.7 Rotated biaxial stress state in a DEN speciemen.

From these observations, it is concluded that the behaviour of the two specimens was almost similar, irrespective of the different initial crack widths. Moreover, the shear loading does not seem to have affected the tensile softening envelop. In this type of partially cracked specimens, basically the behaviour of concrete plates subjected to rotating principal state of stress was tested. The decrease in shear-stiffness at increasing crack width observed by Reinhardt et al.[89] might be attributed to the changing biaxial state of stress in the specimen.

lateral tensile shear at a constant δ ; load-path 1b

Results of a tension-tension experiment on a 200 mm DEN specimen are shown in Fig. 4.8. In Figs. 4.8a,b and (c-e), the P-δ, P-P_S diagrams and the crack patterns are shown. For example, the specimen 14-04 was loaded first in axial tension, and subsequently at three stages on the descending branch, that is, at A, B and C (Fig. 4.8a) the specimen was loaded in lateral tensile shear. During the first shearing regime at A, the specimen 14-04 was in a tension-tension state. As discussed above, maintaining a constant crack width while shearing decreases the axial load. Nevertheless, there is a restriction in the application of the lateral tensile shear. A higher tensile shear would create cracking along the glue layer, that is between the specimen and the loading platen. Therefore, it was decided to limit the lateral tensile load to 6 kN during the first loading regime at A. When $P_S = 6$ kN, the shear load was reversed for the first time and as soon as $P_S = 0$, the axial load was activated for the second time. It can be seen in Fig. 4.8a that during subsequent axial loading the original P-δ curve was reached. This procedure was repeated at points B and C on the descending branch. Even after the second and the third shearing cycle, the original envelop curve was reached again.

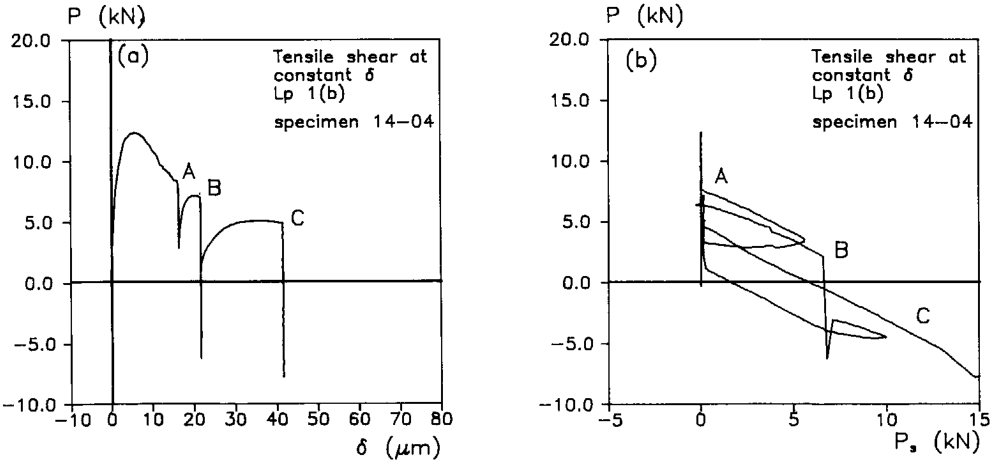

Figure 4.8 P-δ (a) P-P_S (b) response for specimen 14-04: load-path 1(b) experiments.

Fig. 4.8c shows the two cracks that evolved during the test. Crack 1 in Fig. 4.8c initiated at the right notch when axial tension was applied. However, the second crack identified as 2 in the same figure arose as a result of the lateral tensile shear load. Note that crack 2 initiated at the left notch as shown in Fig. 4.8c. The final failure was along crack 2 and was uncontrollable. The specimen was in a clear tension-compression loading state of stress at the time of failure.

Intermittent loadings in the axial and lateral directions hardly seem to influence each other. When the lateral tensile shear was applied, further crack growth along the previously formed tensile crack was not observed. However, tensile shear loading in the lateral direction leads to a completely new set of cracks.

In Fig. 4.8 d and e, the crack patterns for two more identical tests are shown (specimens 14-05 and 15-02). The corresponding P-δ, P_S-δ_S plots are shown in Appendix A1. As can be seen in Figs. 4.8c,d and e, three identical tests gave three different crack patterns, however, the mechanisms are similar. In Fig. 4.8d, first crack "a" formed during the axial tension and subsequent lateral shearing a new crack "b" originated near the right notch and ran towards the bottom loading platen. However, in Fig. 4.8e, first, crack "c" formed during the axial tension, followed by crack "d" and afterwards crack "e". The random occurrence of discontinuity in the primary tensile crack at a large particle can cause stress concentration and eventually leads to diagonal cracking.

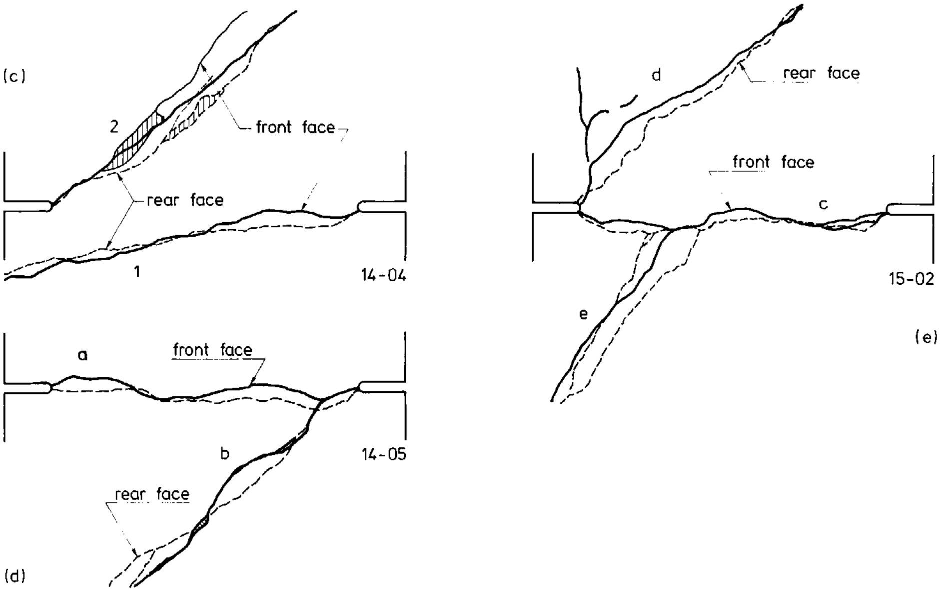

Figure 4.8 (c)-(e) Three different crack patterns for three identical load-path 1(b) experiments.

Summarizing, it is concluded that, at a constant crack opening, tensile shear causes a splitting diagonal failure whereas the compressive shear leads to a change in the specimen stiffness. It is not possible to say whether there was any shear deformation, since during these experiments such a facility was not available in the experimental set up.

Crack growth in biaxial tension-tension experiments can also be studied using reflection photoelasticity as an alternative to the traditional deformation measurements (Van Mier[88]). A thin photoelastic coating was glued to both sides of the specimen. The isochromatic fringes which arise during testing are used as a qualitative measure to study the surface cracking on the specimen. A change in the isochromatics under polarized light corresponds to cracking in the appropriate location. An advantage of the photoelastic technique is that the crack growth can be monitored during the entire testing process.

In Figs. 4.9a and b, the P-δ, P-P_s diagrams for another tension-tension experiment is shown. A photoelastic coating was glued to the front and the rear faces of the specimen 15-04. As in load-path 1b experiments, the specimen is pulled in the axial direction and at $\delta = 11.6$ and 23.4 μm a lateral tensile shear load was applied maintaining a constant deformation. At various stages of loading, the isochromatic patterns at the front and the rear faces of the specimen were photographed. In Fig. 4.10a-e, the photoelastic results are shown. The five stages of the front face isochromatic patterns are numbered 1,13,16,27 and 31. Each stage indicates the extent of surface cracking. As can be seen in Fig. 4.9, these stages are identified on the P-δ diagram.

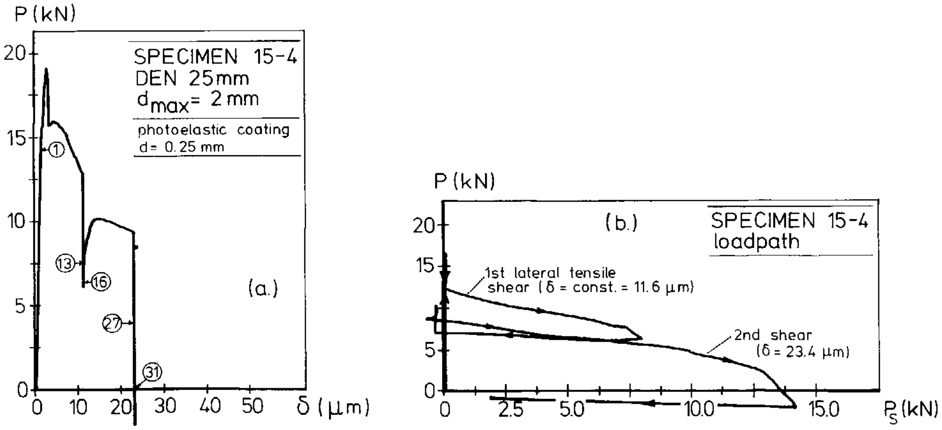

Figure 4.9 P-δ (a), P-P_s (b) diagram for the load-path 1(b) experiment(Van Mier[88]).

At stage 1, two white contours extended from the left and the right notch (Fig. 4.10a). Note, that the stage 1 was in the pre-peak region at 2 μm axial deformation. At stage 13, where 6.9 kN lateral shear was applied, a crack has connected the notches. Due to the lateral tensile shear, two small diagonal cracks emanate at both notches.(Fig. 4.10b). Upon subsequent shearing the crack at the left notch extends further, whereas the crack at the right notch comes to a stop (Fig. 4.10d-e). The directional changes of the crack at the right notch indicates the stress redistribution that occurs during lateral shear. The final failure was along the right diagonal crack and rather explosive since a load control was maintained in the lateral direction.

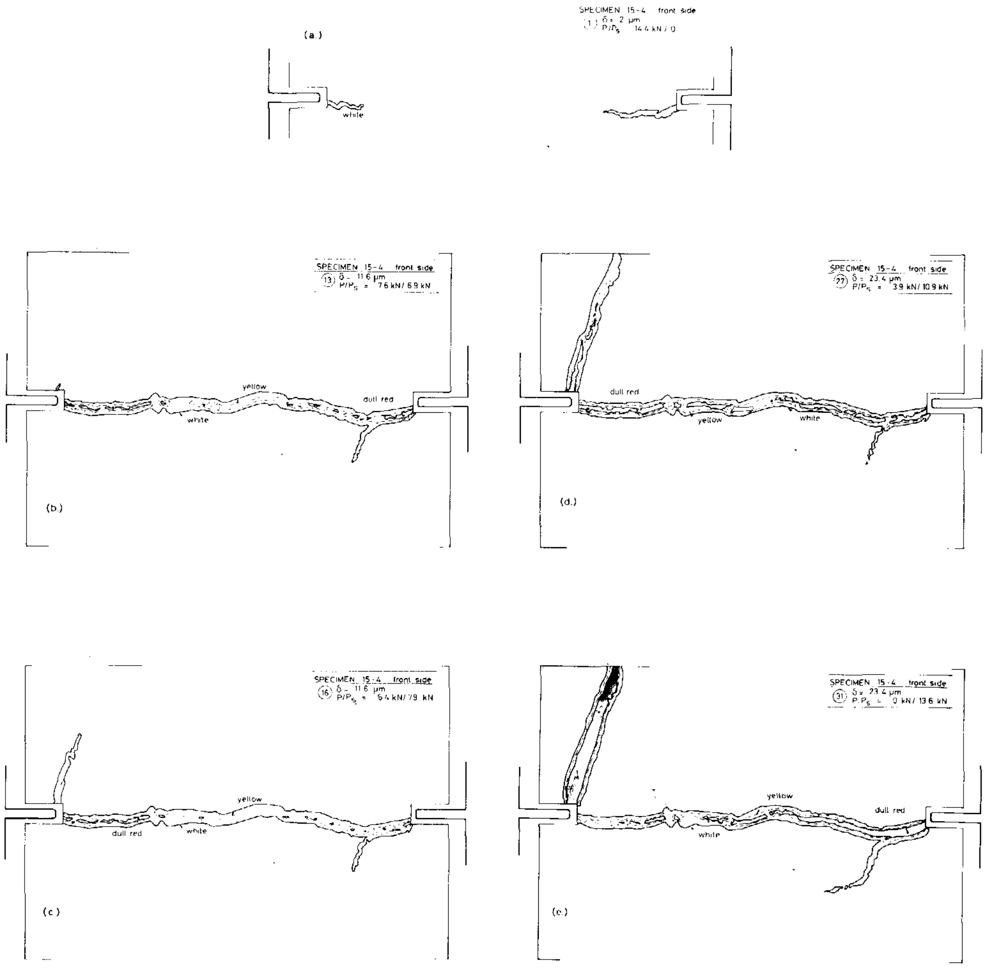

Figure 4.10 Isochromatic patterns at the front side of the specimen at five different stages. The stages are indicated in Figure 4.9(a)(Van Mier[88]).

4.3 Influence of crack opening

In the following paragraphs the influence of the crack width in relation to shear capacity, fracture mode etc. are discussed.

lateral tensile shear at a zero axial load $P = 0$; load-path 2

In this study, δ_a corresponds to a predetermined axial deformation ($P > 0$) on the descending branch where the axial tension begins to unload, whereas δ_{a*} relates to the axial deformation such that $P = 0$. The former and the latter deformations are hereafter called as unloading axial deformation (δ_a) and the true crack opening (δ_{a*}).

Results of experiments with tensile shear at zero axial load are shown in Figs. 4.11 - 4.14 for series 17 and 18. For example specimen 17-04 (see Fig. 4.11a), was pulled in the axial direction and at an unloading axial deformation $\delta_a = 65\ \mu m$, the specimen was unloaded till $P = 0$. Subsequently, the shear load P_s was activated in the lateral direction. Note, that the average true crack opening (δ_{a*}) before shearing was $55\,\mu m$. The corresponding P_s-δ diagram, for $\delta_a = 65\ \mu m$ is shown in Fig. 4.11c. Similarly, for different δ_a values, from 65 till $400\,\mu m$, the relevant P-δ and P_s-δ diagrams are also shown in Figs. 4.11a-c. The crack pattern corresponding to each specimens are given in Fig. 4.12.

The following observation can be made from the P-δ, P_s-δ diagrams and the crack patterns. A decreasing shear capacity due to the increase in unloading axial deformation was measured until $\delta_a = 250\,\mu m$. For crack openings (δ_a) greater than $250\,\mu m$, the shear capacity seems to remain constant. From the crack patterns shown in Figs. 4.12a,b,c and d, for δ_a values less than $250\,\mu m$ multiple diagonal tensile cracks were observed. There is a clear transition in the behaviour of these specimens at $\delta_a = 250\,\mu m$. A transition from tensile splitting to sliding failure was observed at $\delta_a = 250\,\mu m$.

However, at $\delta_a = 250\,\mu m$, the specimens 17-05 had the maximum shear load which was almost twice that of the specimen 18-04, as can be seen in Fig. 4.13b. Furthermore, specimen 17-05 had a higher residual load than that of 18-04 (Fig. 4.13a). The crack patterns of Fig. 4.13e and f show that specimen 17-05 had a crack overlap near the left notch. The failure of the specimen was due to diagonal cracking rather than sliding and this may be due to the non connected crack branches which formed during the axial tension. In contrast, specimen 18-04 failed by sliding and which was accompanied by crack widening. The above observation strengthen the assertion that the $250\,\mu m$ unloading axial deformation falls near the transition from diagonal cracking to sliding failure. However, not enough tests have been carried out to come to a sound statistical basis for this conclusion.

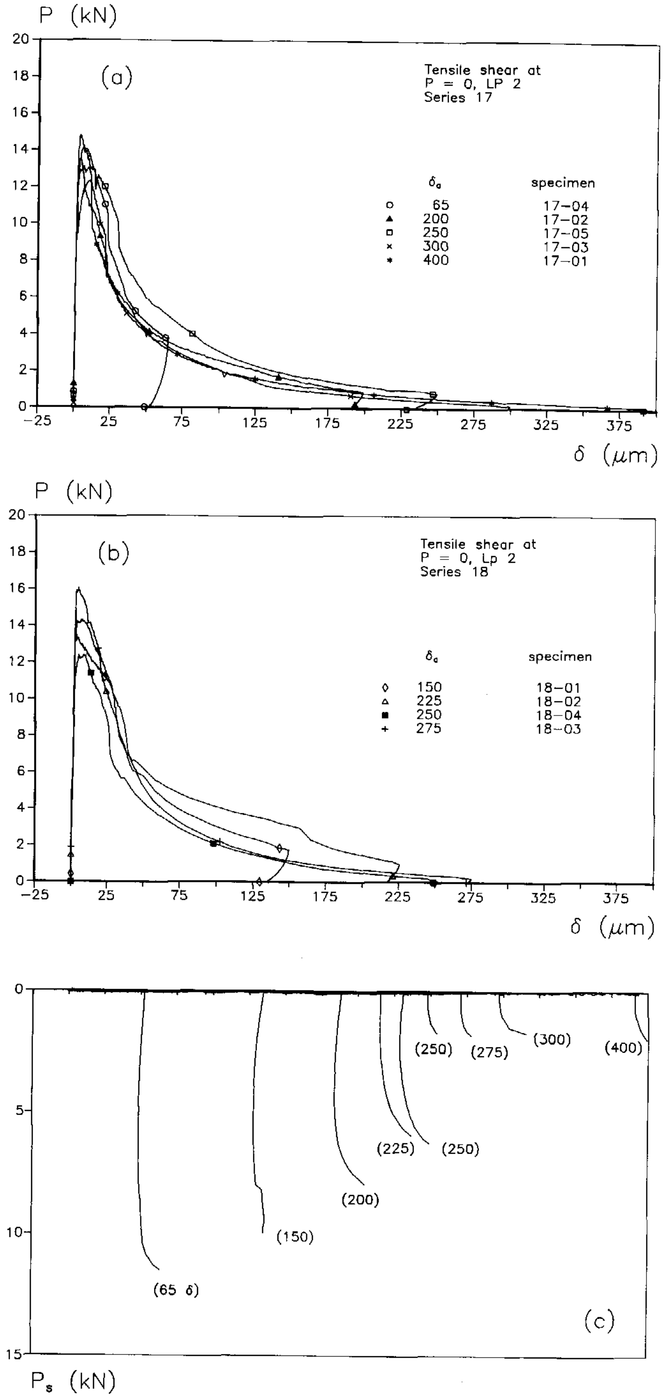

Figure 4.11 P-δ diagram for series 17 (a), series 18 (b) and P_S-δ diagram (c) for the load-path 2 experiments.

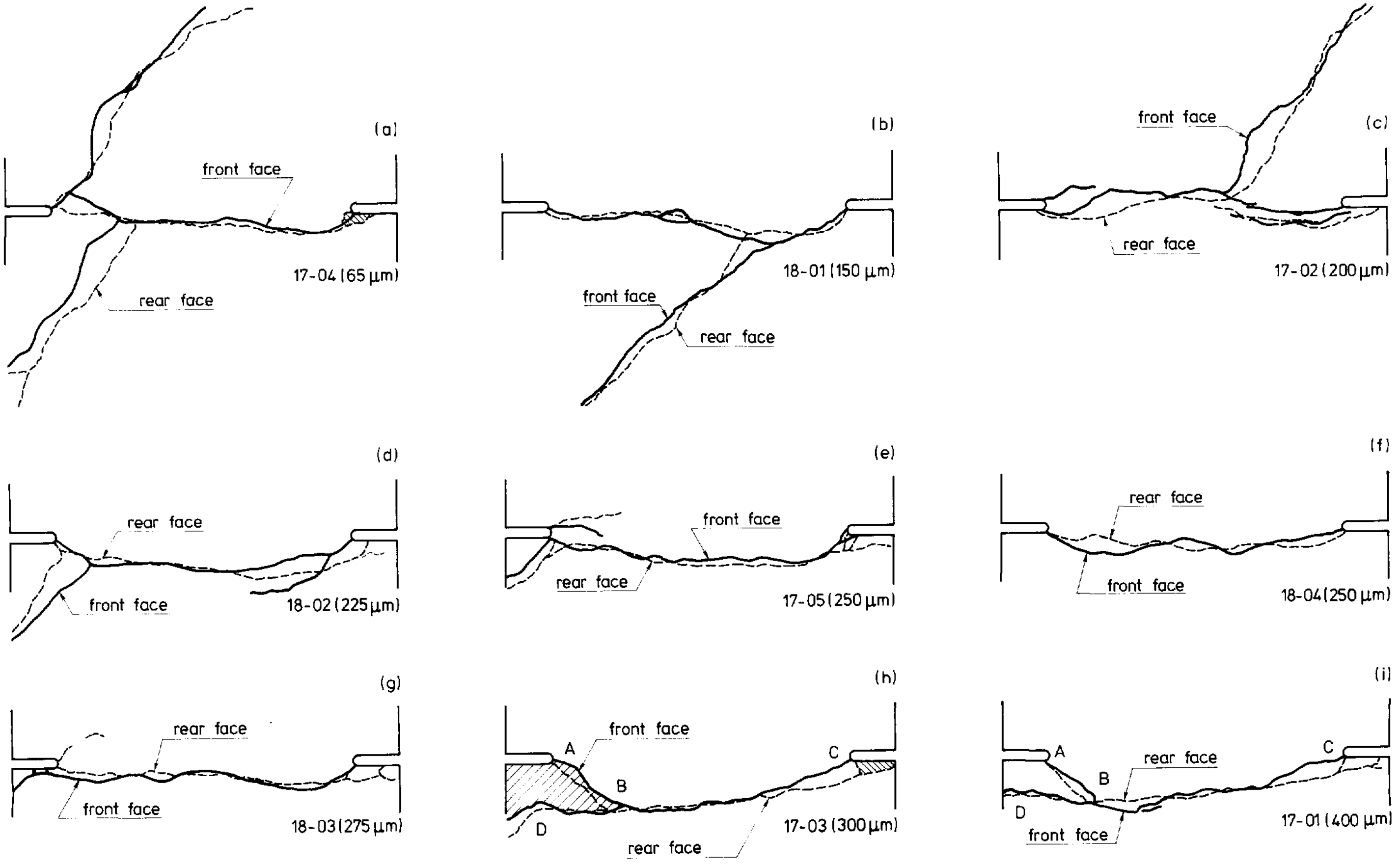

Figure 4.12 The final crack patterns for the load-path 2 experiments. Front face cracks are shown as solid lines, rear face cracks as dashed lines. The unloading axial deformation is indicated in each case.

In all the tests with sliding failure beyond $\delta_a = 250\,\mu$m, no side cracks were visible except for specimens 17-03 and 17-01 with $\delta_a = 300$ and $400\,\mu$m respectively. In Figs. 4.12 h and i, the crack branches AB were relatively narrow and further opening of crack AB slowed down after crack initiation. This is in line with the observations on the crack openings at the right notch as can be seen in the δ_i-δ plot shown in Fig. 4.14. In both of these tests, the final crack-plane ran along path CBD, which is below the gauge length of the extensometers 1 and 4. A system of overlapping cracks evolved in these two experiments as was shown in the photoelastic experiment in the previous section.

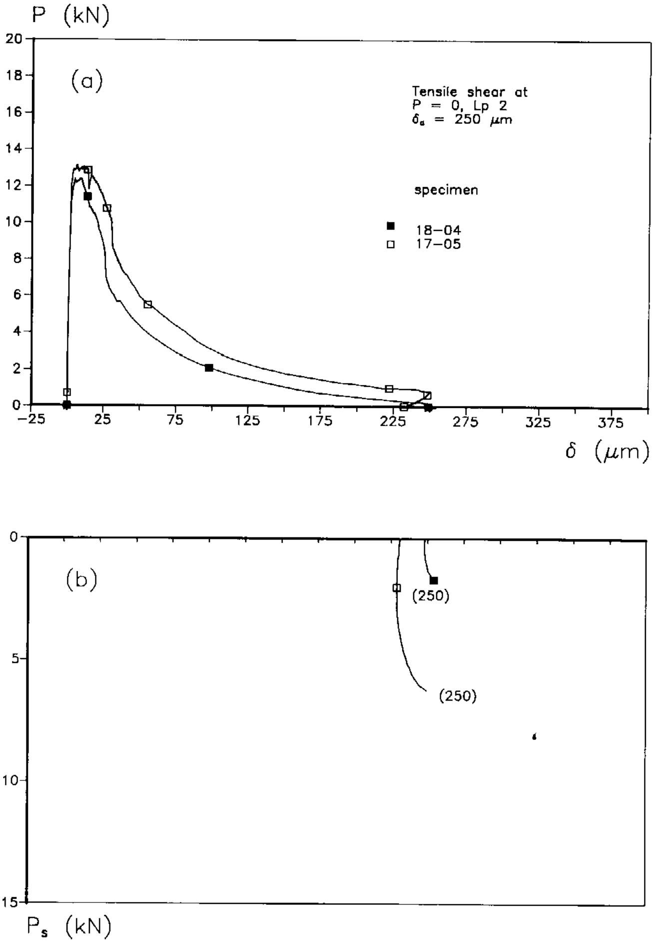

Figure 4.13 P-δ (a) and P_S-δ (b) response for two experiments (load-path 2), unloading axial deformation $= 250\,\mu$m.

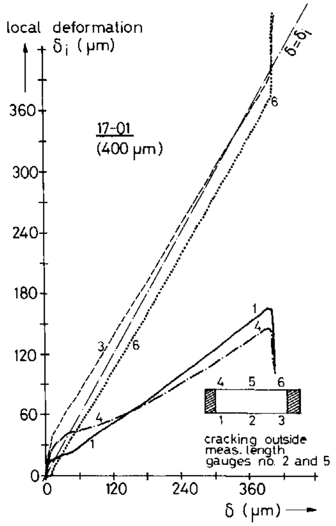

Figure 4.14 Local deformation δ_i versus LVDT deformation δ for the load-path 2 experiment at the unloading axial deformation = 400 μm.

In sum, it can be said that the development of non-connected crack branches and crack interface bridging, which evolved during uniaxial tension has a clear effect on the final fracture mode under shearing.

It is important to mention that the testing process was constantly updated. When the load-path 2 experiments were carried out, the facility to measure the lateral shear deformation δ_s was not available in the testing arrangement. Therefore, it was not possible to calculate the shear stiffness with respect to different crack openings in the load-path 2 and the load- path 1a and 1b experiments as well. In this sense the load-path 3 experiments were a further extension in the development of the testing technique.

4.4 Influence of axial confinement

To be able to study the influence of the axial confinement on a partially opened crack, the load-paths 3a and 3b were pursued. Some results of load-path 3 have been published before, see Nooru-Mohamed & Van Mier[89]. For the load-path 3a experiments, the lateral shear force was applied while a zero axial load prevailed normal to the partially opened crack surface. However, in the load-path 3b experiments, the shear load was applied while a 1000 kN axial force was maintained normal to the crack surface. In this way an actual comparison can be made with respect to the unconfined and the confined experiments.

Three types of materials namely: mortar, normalweight concrete and Lytag lightweight high strength concrete with maximum aggregate size d_{max} of 2, 16 and 12 mm respectively were used. In the Lytag mix, 12 mm is the largest diameter of the Lytag particle, whereas the maximum diameter of the sand particle was 4 mm. Three different unloading deformations were chosen for each material. For mortar the unloading deformations were, $\delta_a = 225, 250$ and $275\,\mu$m; for 16 mm concrete, $\delta_a = 200, 300$ and $400\,\mu$m; and for the Lytag, in view of the expected local smoothness of the fracture plane relatively low values were chosen: $\delta_a = 50$, 100 and 150 μm. In Appendix A2 (see Table A2), the test scheme corresponding to load-path 3 is given.

The reason for choosing different axial openings was to determine the shear stiffness as a function of axial opening, and also to find out any shift in failure modes similar to the diagonal tensile/cracking transition discussed in section 4.2.

In the following section, the results obtained for the Lytag concrete results are discussed.

4.4.1 Lytag unconfined shear (load-path 3a)

In Fig. 4.15 a,b and c the P-δ, P_s-δ_s and the $\delta-\delta_s$ diagrams for specimen 29-06, 29-01 and 29-02, with unloading deformations of 50, 100 and 150 μm are shown. As far as the peak values of the uniaxial P-δ diagrams are concerned, there is a relatively small scatter. Fig. 4.15b shows the corresponding P_s- δ_s diagrams. From Figs. 4.15a and 4.15b the interaction between average axial opening, residual load and shear capacity can be identified. It is evident that the shear capacity decreases when the average axial opening increases (Fig. 4.15b). Comparing Figs. 4.15a and 4.15b, it can be concluded that a lower residual load leads to a lower shear capacity. A large axial opening is related to more damage in the fracture zone, which will consequently lead to a lower stiffness (Fig. 4.15b). The same tendency was reported by Reinhardt et al.[89]. In the latter tests, shear was applied at constant crack width, which differed from the present experiments where no restriction existed with regard to the axial crack opening and P = 0 normal to the crack plane.

In all three tests final failure was due to sliding. From the P_s- δ_s diagrams it can be seen that the shear load increased up to a peak and descended rapidly afterwards. As soon as both halves started to slide and simultaneously the axial crack opened, failure was uncontrollable. The crack patterns obtained for the three specimens were identical, see Fig. 4.16. A transition in fracture modes, similar to the transition reported for mortar in section

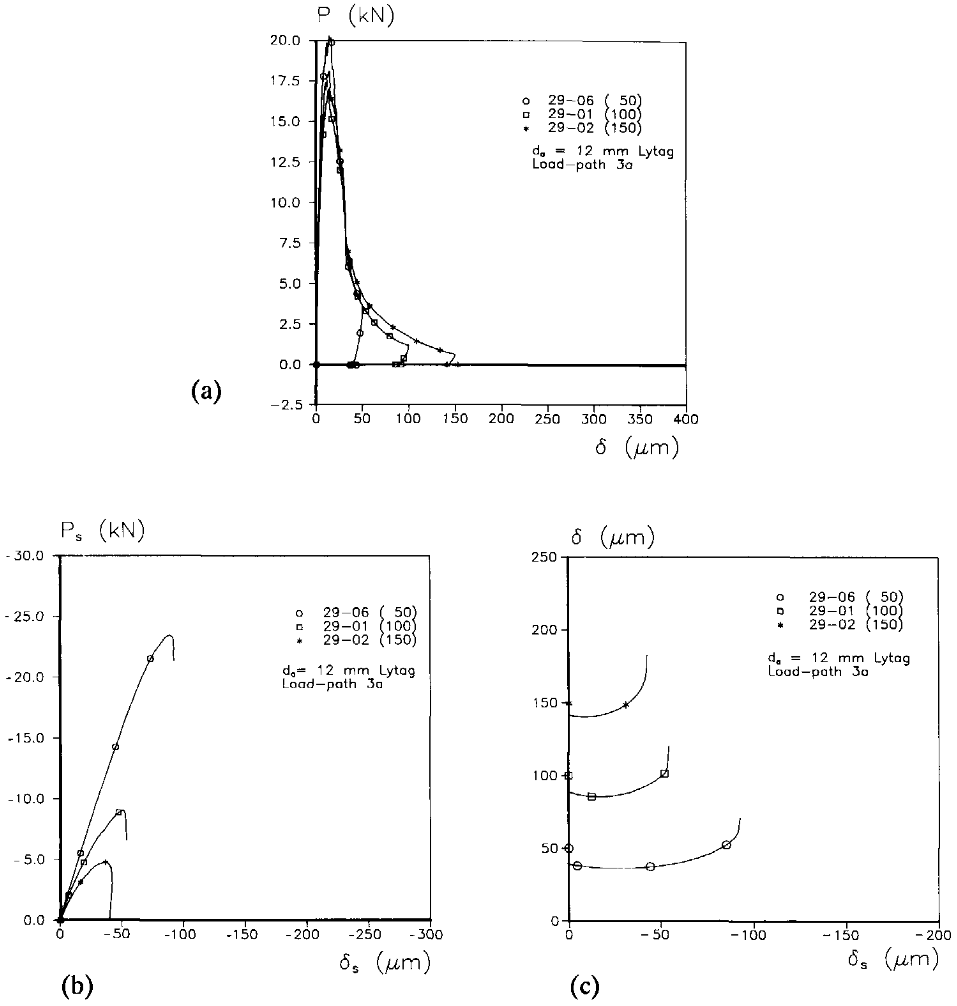

Figure 4.15 P-δ (a), P_S-δ_S (b) and δ-δ_S (c) diagrams for the unconfined shear (load-path 3a) experiments at different values of axial crack openings.

4.3 was not seen in these Lytag experiments with axial openings of 50, 100 and 150 μm. However, the shear force was compressive instead of tensile in the above tests, and also the material used was different. The Lytag concrete had aggregates which were weaker than the matrix and cracks ran through the matrix as well as through the aggregates, and the final surface contained less protruding particles as compared to normal concrete.

The unconfined shear experiments (load-path 3a) were performed for 2 mm mortar and 16 mm concrete as well. For 2 mm mortar a correlation between the axial opening and the shear stiffness as was seen for the Lytag concrete was not observed. It can be that the three axial openings chosen for the 2 mm mortar was almost in the narrow range, 225, 250 and 275 μm. Moreover, any two identical tests of 2 mm mortar gave completely different shear behaviour. In Appendix A3 and A4, the unconfined and confined results for the 2 mm mortar and 16 mm concrete are shown.

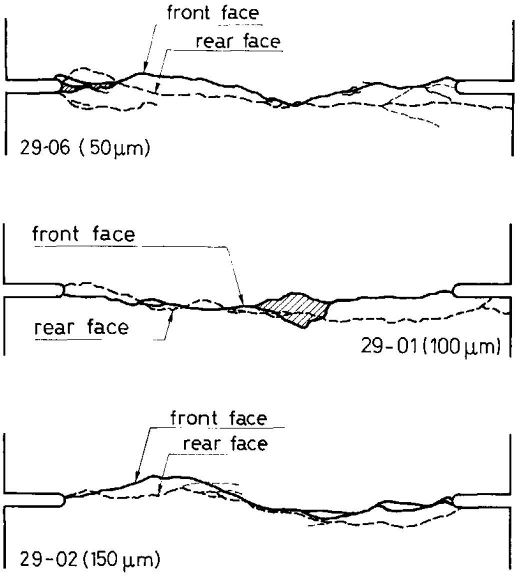

Figure 4.16 crack patterns corresponding to load-path 3a experiments.

4.4.2 Lytag confined shear (load-path 3b)

In Fig. 4.17a, b and c, the P-δ, P_S-δ_S and the δ-δ_S diagrams for the Lytag specimens 29-03, 29-04 and 29-05 are shown. The unloading axial deformation δ_a was 50, 100 and 150 μm respectively. From Fig. 4.17a it can be seen that during unloading δ_a was reduced considerably due to crack closing, especially when compressive confinement was introduced normal to the crack plane. The axial crack opening immediately before shearing was 30.0, 65.4 and 98.6 μm for specimens 29-03, 29-04 and 29-05 respectively.

In Fig. 4.17b the corresponding P_S-δ_S diagrams are shown. A decrease of shear stiffness with increasing axial crack opening was observed, similar to the unconfined tests (Fig. 4.17b). Yet it is difficult to compare the stiffness of confined and unconfined tests. This is because shear was applied at different axial openings for confined and unconfined specimens, even though both had the same axial unloading deformation δ_a.

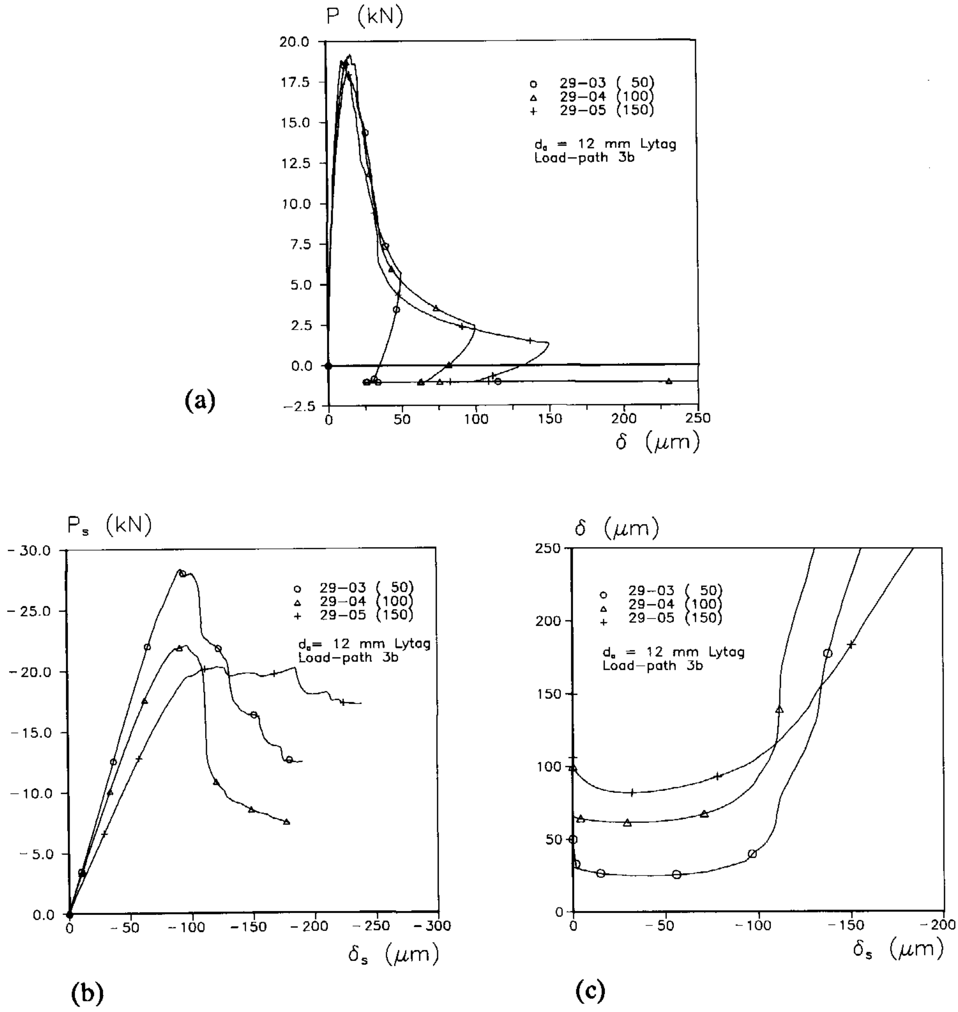

Figure 4.17 P-δ (a), P_S-δ_S (b) and δ-δ_S (c) diagrams for the unconfined shear (load-path 3b) experiments at different values of axial crack.

Initially both P_S and δ_S increased. Once P_S has reached a peak shear value, a gradual decrease of P_S was observed while δ_S increased. This can be called "shear softening",analogous to softening in uniaxial tension. All three experiments showed a stable behaviour. However, the P_S- δ_S curves stabilized at various residual load levels, or put differently, a constant shear load was measured under increasing shear displacement. The effect can be explained from differences in crack modes. Consider for example experiment 29-05 with

$\delta_a = 150\,\mu m$ (see Fig. 4.18c). Crack ABC developed in axial tension, whereas due to shear branch CD extended. Furthermore, it was found that crack BC closed during shearing, indicating that a compressive strut developed in the specimen as shown in Fig. 4.19. The distance BC is a measure for the strut size, and the crack branch CD is no more than a splitting crack parallel to the strut. The development of CD was restricted due to the confinement in axial direction, viz. P = -1000 N. In the other experiments (with $\delta_a = 50$ and $100\,\mu m$) a similar mechanism was observed. Yet in the latter experiments the strut size seemed much smaller. Each experiment was duplicated and a good repeatability was observed.

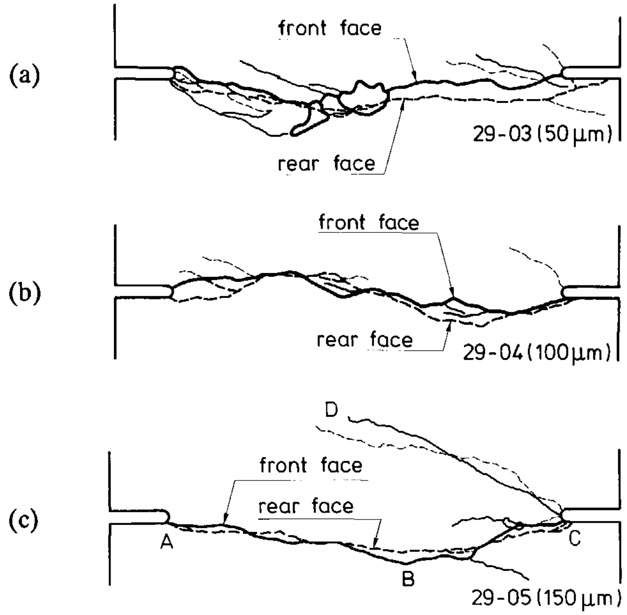

Figure 4.18 Crack patterns corresponding to load-path 3b experiments.

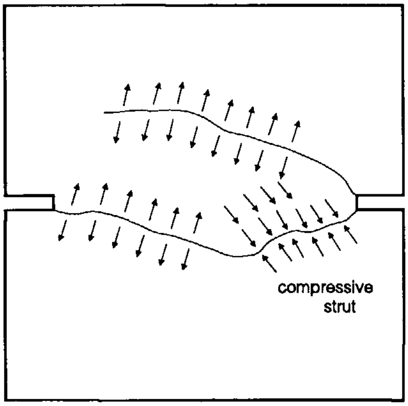

Figure 4.19 Schematic representation of the compressive strut.

crack opening path

The behaviour of a specimen in a confined situation is schematically clarified in Fig. 4.20 As shown in Fig. 4.20a, the P-δ curve reached position 1, where it corresponds to δ_a, the unloading axial deformation. The specimen was further unloaded to a confinement of 1000 N compressive force in the axial direction and the P-δ curve reached position 2. In Fig. 4.20b, the position 2 is shown as a decrease in δ, at a constant $\delta_S(=0)$. At position 2, a compressive shear force was applied. During this time the previously opened crack closed and reached position 3 (Fig. 4.20a and b). At position 3 (Fig. 4.20a), an increase in the lateral shear load is associated with an increase in the lateral shear δ_S. However, the vertical deformation remained stationary (Fig.4.20b). In Fig. 4.20b this is shown from 3 to 3* which can be called a *free slip* (non dilatant shear). Due to the lateral shear load, the partially opened crack surfaces first close and afterwards slide to engage themselves to resist shear. This engagement or a free slip occurs before one surface establishes bearing on the other (at 3*). After a good bearing was established further shear slip was accompanied by fracturing of the specimen. This is identified as 4 in the diagrams.

The crack opening paths (δ-δ_S curves) for the confined and the unconfined experiments for the Lytag concrete are shown in Figs. 4.15c and 4.17c. In Fig. 4.15c, the horizontal plateau corresponds to the free slip which occurred during the initial shearing of the two halves when zero axial load prevailed over the crack plane. However, a comparison between the two crack opening paths clearly indicates the influence of the confinement. The crack opening paths for the 2 mm mortar and 16 mm concrete are shown in the Appendix A3 and A4. The schematized crack opening path described above also applies to these two materials.

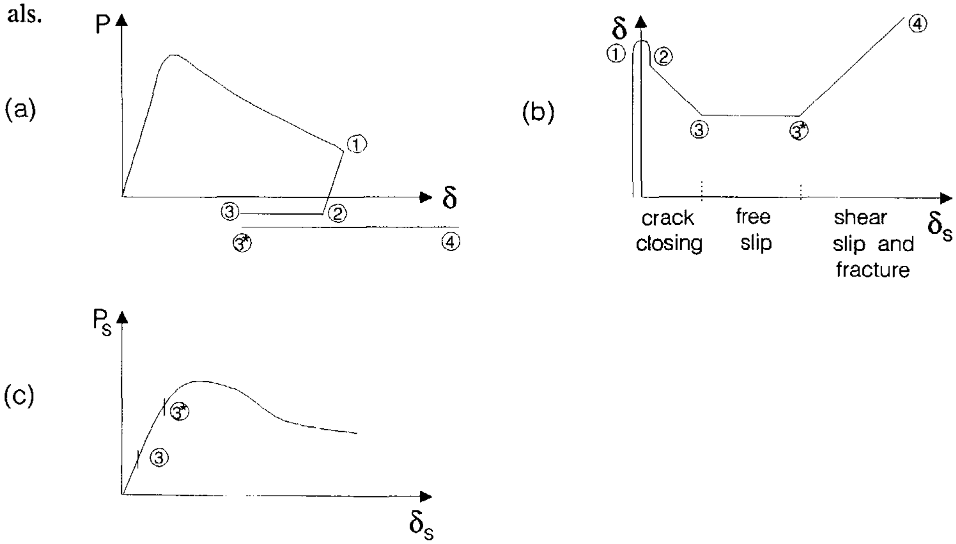

Figure 4.20 Schematic representation of the crack opening path associated with the load-path 3 experiments.

a comparison with aggregate interlock results

Shear transfer by aggregate interlock has been thoroughly investigated in the late 1970s. Shear force can be transmitted over a tensile crack due to interlocking of protruding aggregate particles from each crack face on the matrix surface during sliding. A large amount of experimental results and analytical work exists on this aspect.

The load-path 3b experiments using DEN specimens can be used to compare with the previously published aggregate interlock results. It is worth recalling that in load-path 3b experiments first a tensile crack was formed due to axial tension and that at a prescribed axial deformation the axial force was unloaded and replaced by a compressive force of -1000N. Subsequently a lateral shear was applied in displacement control while load control was maintained along the vertical direction.

In the aggregate interlock experiments, researchers have maintained one or more of the following conditions over the crack surface in their experiments: (1) a restraining stiffness normal to the crack, (2) a restraining force normal to the crack, and (3) a constant crack width. According to Millard & Johnson[86], maintaining a restraining stiffness normal to the crack resemble closer to the occurrence in reinforced concrete and to conduct tests with constant normal restraining forces would result in an unrealistic amount of crack widening due to frictional overriding. They also assert that tests with a constant crack width would bear little resemblance to the real situation as the shear force would be provided almost entirely by crushing of the cement matrix surrounding aggregate particles.

The confined experiments (load-path 3b) performed with the three materials correspond to the second condition i.e, maintaining a constant restraining force normal to the crack. However, from the results discussed above and as shown in the crack opening paths in Fig. 4.17c for the Lytag concrete, an unrealistic crack widening as claimed by Millard & Johnson[86] was not observed, see the crack opening paths for mortar and concrete in the Appendix A3 and A4 (Fig. A3.3c and A4.3c).

In numerical analyses it is important to know the role of aggregate interlock for small crack openings. Almost all the aggregate interlock experiments were conducted on specimens which were pre-cracked along the shear plane. This shear plane forms along a precast grove at the middle of the specimen and a tensile crack was formed by applying a line load along this grove (Walraven[80]). This entire pre-cracking process was performed in a rather uncontrolled manner. The initial crack width in the experiments of Walraven[80] varied from 0 to 400 μm. Yet, the tensile capacity of the crack was not known. Afterwards, the desired crack width was set using the nuts on the restraining bars (Walraven[80], Laible et al.[77]).

By contrast, in the load-path 3b experiments the specimen was pulled in the vertical direction and unloaded at a desired axial opening till the required compression was reached in a controlled manner. The loading rate was 1.6 μm/minute. The true axial opening varied with respect to each material which is due to the choice of the unloading axial deformation. The detailed information with respect to actual openings is given in the Table 4.1. However, the true crack opening varied between, 188 to 231 μm, 148 to 359 μm and 30 to 108 μm for 2 mm mortar, 16 mm concrete and 12 mm Lytag respectively.

A comparison is now made with the aggregate interlock experiments of Walraven[80] on externally restraint bars. Fig. 4.21 shows the crack opening paths for two tests of Walraven[80], with the same initial axial opening of 400 μm ($d_{max} = 16$ mm, $f_c = 37.6$ MPa) and the restraining stiffness of 1.5 MPa/mm and 5.0 MPa/mm. These restraining stiffness were computed based on the normal stresses 0.3 and 1.0 MPa at an arbitrarily defined crack width of 600 μm. As can be seen in the Fig. 4.21, the continuous line with the symbols (a circle and a square) correspond to the actual test result of Walraven and the broken line is a speculation what has occurred during the uncontrolled cracking of the specimens. Information with regard to the crack opening behaviour at small slip from zero to 70 μm cannot be inferred from the results of Walraven. In the same figure, the crack opening paths for two experiments with unconfined and confined shear (load-paths 3a and 3b) are shown. Note that the maximum aggregate size was 16 mm and the compressive strength was 49.6 MPa, which is higher than the aggregate interlock results shown. Moreover, the unloading axial deformation was 400 μm in the present test and the true axial opening at the time of shearing was 395, and 359 μm for the unconfined and confined experiments respectively. By comparing the two results, it can be seen that the aggregate interlock results with externally restrained bars falls between the present results with zero and 0.13 MPa confinement. In the experiments of Walraven, a slight change in the restraint stiffness leads to a different crack opening path, as shown in Fig. 4.21. Furthermore, at a constant slip, a decrease in axial restraint leads to an increase in axial opening. Since specimen 28-04 had the lowest axial stress of 0.13 MPa, it was expected that the crack opening path would fall above the rest of the crack opening paths of Walraven. However an opposite trend was seen. This discrepancy may be due to the inherent difference in the mechanism in which shear was transferred in both type of experiments. In the aggregate interlock experiments, first a through crack was created in the specimen such that it could carry no load normal to the crack plane. And the crack plane were subsequently loaded in in-plane shear, where shear was resisted only due to aggregate interlock. In the present experiments a tensile crack was formed in a controlled manner and unloaded to the desired axial compression at a predetermined axial opening. It was observed that during shear not only sliding but also further fracturing of the specimen occurred. This observation question the applicability of the aggregate interlock theories for small crack openings.

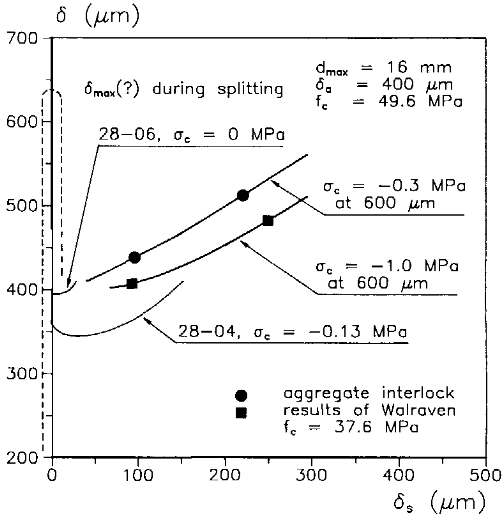

Figure 4.21 A comparison between the crack opening paths from the aggregate interlock experiments of Walraven[80] and the present study.

4.4.3 Shear stiffness analysis

The shear resistance of a cracked concrete specimen may vary depending on the crack width and the amount of confinement normal to the crack plane (Walraven[80], Paulay & Loeber[74]). In Fig. 4.22, the decrease of initial shear stiffness P_s/δ_s is shown as a function of the axial crack opening δ_{a*}. The shear stiffness was defined as the secant modulus between 10% and 30% of the maximum P_s values. The δ_{a*} represents the true crack opening at which shearing was initiated, and is smaller than the unloading axial deformation δ_a. In Table 4.1 (section 4.5) the true axial openings corresponding to this test series are given. In Fig. 4.22, the results of all successful experiments are included. A decreasing shear stiffness is observed for the three materials tested, and for larger crack openings ($\delta_{a*} > 200\,\mu$m), there seems to be an influence of the confining stress normal to the crack plane.

In finite element analysis the shear stiffness of a cracked concrete is represented by means of a shear retention factor β, which indicates the percentage of the elastic shear modulus that is retained after cracking. The elastic shear modulus G_0 is reduced to βG_0 once the solid is cracked. The shear retention factor β, can be related to the cracked shear modulus G_{cr}, simply considering that the βG_0 is associated with the total strain, and G_{cr} with the crack strain. By decomposition of the total strain into an un-cracked and cracked strain, the assumption was made that the concrete and the crack act like springs connected in series. This leads to the following stiffness relation (Rots et al.[84], De Borst & Nauta[85]):

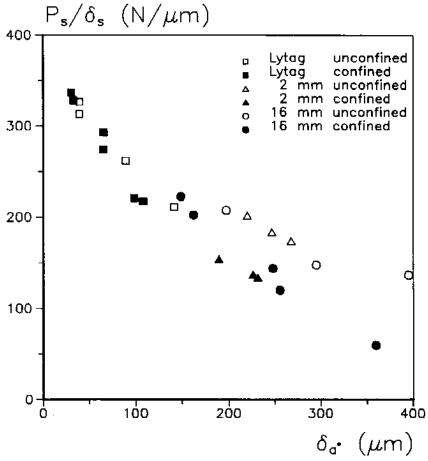

Figure 4.22 Reduction of shear stiffness as a function of axial crack opening δ_{a*}.

$$1/G_0 + 1/G_{cr} = 1/(\beta G_0) \qquad \text{......(4.1)}$$

This implies that

$$G_{cr} = (\beta/(1-\beta))G_0 \qquad \text{......(4.2)}$$

Using the aggregate interlock results of Paulay & Loeber[74], Rots[84] had proposed a formulation for β as a function of ε_{nn}, where ε_{nn} is the smeared out normal strain.

$$\beta = 1 / (1 + 4447\, \varepsilon_{nn}) \qquad \text{......(4.3)}$$

A similar formulation was also obtained by Rots[84] using the rough crack model proposed by Bazant & Gambarova[80].

$$\beta = 1 / (4762\, \varepsilon_{nn}) - 1 / (1346\, \sqrt{\varepsilon_{nn}}) \qquad \text{......(4.4)}$$

Pruijssers[88] proposed a different formulation based on the two phase model of Walraven and links β as a function of ε_{nn} and γ.

The formulation proposed by Rots requires knowledge of the crack band width h, which conveniently cancelled while formulating equation 4.2. However, one encounters some practical problems when extracting β values from the current results. Choosing the correct band width h was indeed a problem in computing β values from the present test results.

Assume a crack band h which forms in a rectangular concrete cross section due to shearing as shown in Fig. 4.23. Then the shear strain $\gamma = \delta_s/h$. From the experimental results, δ_s values can be retrieved. There are three possibilities for the choice of the crack band width h.

- the gauge length of the control LVDT, which was equal to 65 mm
- the ligament length l between the notch
- three times the maximum aggregate size (Bazant[84]).

In the following paragraphs the procedures adopted for the calculation of β values are briefly mentioned.

Preliminaries

Method adopted for load-path 3a and 3b experiments.

Step 1 : Calculate G_0 from $G_0 = E/2(1+\nu)$. Where $E_0 = 0.3P_{max}/(\delta$ at 0.3Pmax) and (E = average of E_0 computed out of 12 tests).

Step 2 : Read P_{max} for each test.

Step 3 : Compute $0.3P_{max}$.

Step 4 : Read δ and δ_s values corresponding to 0.3Pmax and $\varepsilon_{nn} = \delta$/gauge length = 65 mm.

Step 5 : Compute τ, which is equal to $0.3P_{max}/l*t$ where t is the thickness of the specimen.

Step 6 : Compute ε_{nn}: $\varepsilon_{nn} = (\delta$ at 0.3Pmax) / (l_{gauge} = 65 mm)

Step 7 : Compute γ, which is equal to δ_s/h

Step 8 : Compute $G_{cr} = \tau / \gamma$

Step 9 : Use equation (4.1), $G_{cr} = (\beta/(1-\beta))G_0$ to calculate β.

Step 10 : Compare the β value obtained in Step 9 with equation (4.2)

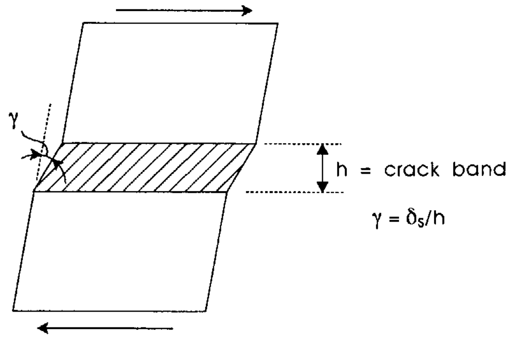

Figure 4.23 Assumption of crack band for shear strain calculation.

In load-paths 3a and 3b three materials were used. In Figs. 4.24 a,b and c the computed values for the shear retention factor β for the three materials are plotted against the smeared normal strain ε_{nn}. In the same figure the β values obtained from Equation (4.3) are also plotted. As can be seen in Fig. 4.24a, an increase in axial normal strain caused a reduction in the shear retention. For the 16mm concrete, the three h values chosen were 48 mm (three times the maximum aggregate size), 65 mm(the gauge length of the vertical LVDT) and the ligament length l between the notches. As can be seen in Fig. 4.24a, the estimated β value depends heavily on the choice of the crack band width h. A lower and a higher shear retention β is obtained when h is equal to 3^*d_a and the ligament length l respectively. For the 16 mm concrete, the computed β values are larger compared to the same values obtained using equation (4.2), formulated by Rots[84]. Note, however that the choice of the crack band width $h = 3^*d_a$ comes closer to the Equation (4.3) at larger axial strain. Based on the above observation, it is extremely difficult to propose a crack band width h for the evaluation of β.

A different phenomenon is observed for the Lytag concrete. Here, four h values chosen were 6, 36, 65 mm and l. Again, the choice of a h value greatly influences the β values computed (see Fig. 4.24b).The choice of the band width h = 6 and 36 mm underestimates the β values computed from Equation (4.3). Moreover, the final crack pattern for the Lytag specimens showed crack branching apart from the major crack(see Fig. 4.18c). However, for the 16 mm concrete, tortuous crack formed with secondary cracking (see Appendix A4, Fig. A4.4a-e). For the Lytag concrete, a choice of a crack band h = 6 mm gave an extremely low shear retention factor. Furthermore, irrespective of the material, a decrease in the axial smeared normal strain led to a higher shear retention.

4.5 Influence of material structure

The influence of the material structure can be derived from the load-path 3a and 3b experiments performed on three materials: Lytag, mortar and 16 mm concrete.

With regard to a partially opened crack, the two important factors are:(1) the amount of stress transfer over the crack surface, and (2) the magnitude of the crack opening. Depending on these two factors, further crack development may be due to tensile splitting or sliding of the fracture surface after overcoming the resistance from aggregate interlock, surface tortuosity etc. As discussed in section 4.3, a transition in fracture mode from tensile splitting to sliding failure occurs in the neighbourhood of 250 μm axial deformation, when the lateral tension was applied in the presence of a zero axial load. It was one of the aims to see whether a similar transition in failure modes occurs when the lateral shear is compression instead of tension. Furthermore, the amount of crack opening required for

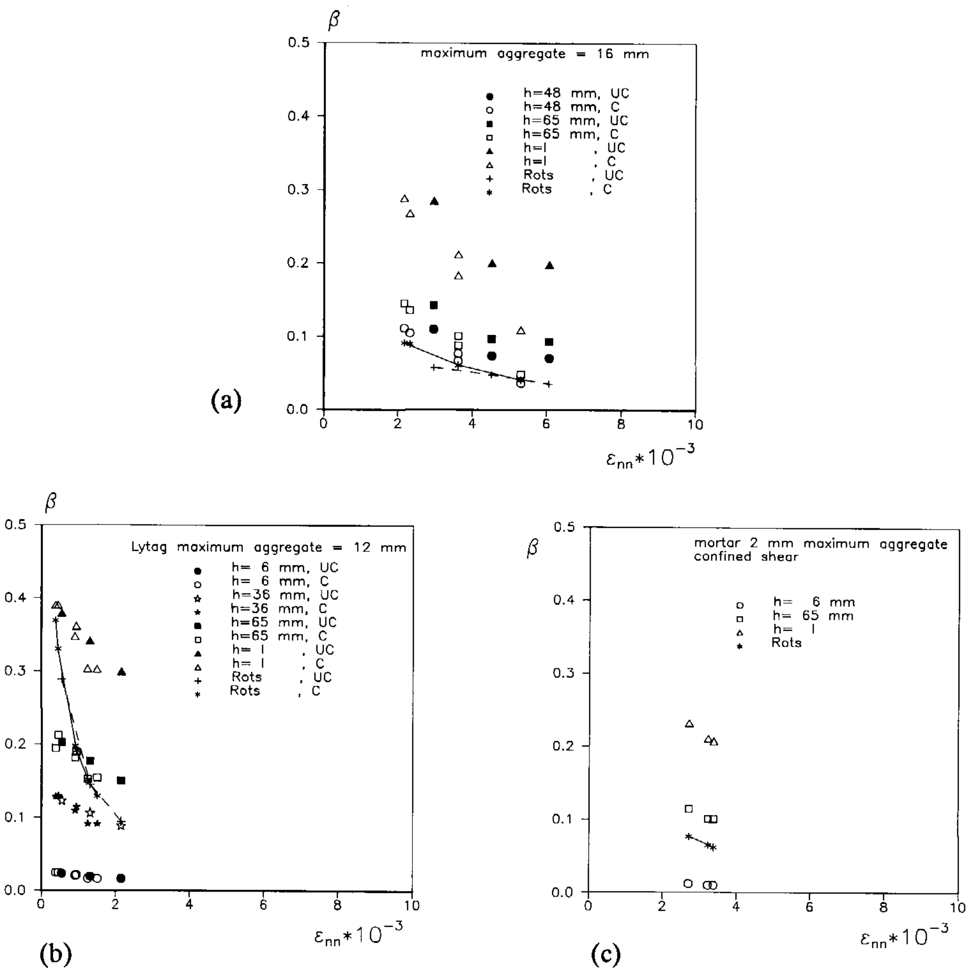

Figure 4.24 Plot of computed β values versus axial normal strain ε_{nn} for various crack band widths for 16 mm concrete (a) 12 mm Lyag (b) and 12 mm mortar (c).

sliding heavily depends on the material structure. Keeping the material structure in mind fairly small and large deformations were chosen. For example, in Lytag concrete, the crack always runs through the aggregate, since the matrix is stronger than the aggregate. In this type of materials the maximum axial opening which could be reached was in the neighborhood of 150 μm. However, for the 16 mm concrete axial opening as high as 400 μm was chosen. For the 2 mm concrete, crack openings were 225, 250 and 275 μm.

In Fig. 4.25a the load-displacement (P-δ) response of the three materials are compared for load-path 3a and 3b. As can be seen in Fig. 4.25a, the Lytag concrete showed a brittle behaviour. The highest axial tensile peak load was attained by the Lytag concrete, followed by 16 and 2 mm concrete. In all three materials there exists the usual scatter in the axial peak load. This may be due to the differences in the age of loading, and the batch strength. The residual load, for example, at δ = 150 μm was larger for 16 mm concrete and followed by 2 mm and Lytag. The largest sand particle used in the Lytag concrete was 4 mm as compared to 2 mm mortar. In spite of that, a higher residual load for Lytag concrete could not be seen.

After unloading the specimen to a 1000 kN axial compression, the lateral compressive shear was applied. The true axial opening (δ_{a*}) at the time of shearing is shown in Table 4.1. As can be seen in Table 4.1, two identical tests gave two different crack openings. (i.e., 231.4 and 226.0 μm corresponding to 26-02 and 32-06 both had the same δ_a = 275 μm).

Table 4.1

Material	Specimen no	True axial opening δ_{a*} (μm)	Unloading axial opening δ_a (μm)
2 mm	26-03	188.6	225
"	26-02	231.4	275
"	32-06	226.0	275
16 mm	28-01	148.4	200
"	27-05	161.4	200
"	28-03	247.8	300
"	27-02	255.5	300
"	28-04	359.4	400
Lytag	29-03	30.0	50
	30-04	32.6	50
	29-04	65.4	100
	30-01	65.2	100
	30-03	108.0	150
	29-05	98.6	150

In Fig. 4.25b the P_s-δ_s diagrams for all three materials corresponding to load-path 3b are compared,whereby, it is understood that the true axial crack opening at the time of shearing was not identical for every specimen. As can be seen in Fig. 4.25b, the shear stiffness for the lytag concrete was larger compared to 16 mm concrete. The amount of confinement over the crack plane is the same for all the specimens. However, the axial true crack opening before shearing was 30.0 to 108 μm for the Lytag concrete, whereas 148.4 to 359.4 μm for the 16 mm concrete. For the 2 mm mortar, the shear stiffness was between the

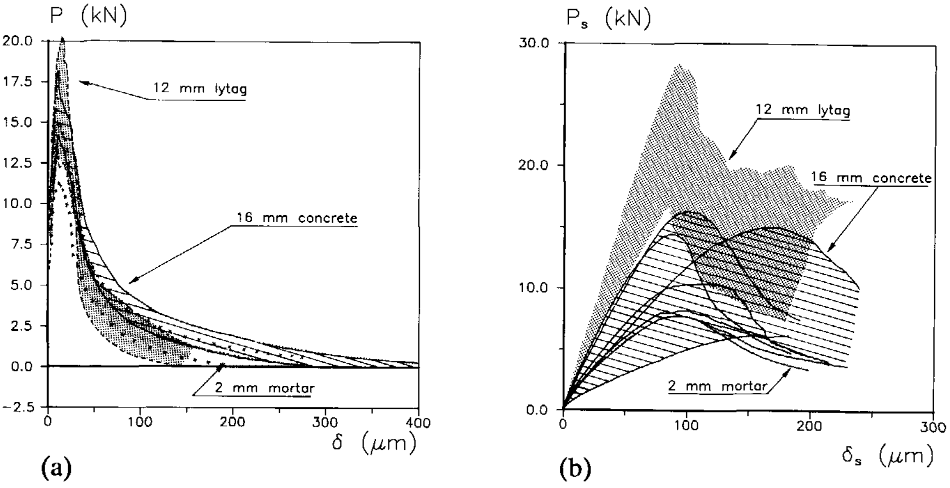

Figure 4.25 Comparison of P-δ (a) and P_S-δ_S (b) response for three different concretes.

highest and the lowest values of the 16 mm concrete. Again, the true crack opening for the 2 mm mortar is lower than that of the 16 mm concrete, see Table 4.1. The largest peak shear load was reached by the Lytag concrete and followed by 16 mm concrete and 2 mm mortar.

The final crack pattern observed for the 16 mm concrete showed a tortuous crack path and very many secondary cracks compared to the 2 mm mortar. These secondary cracks formed during the lateral shearing regime.

The crack patterns and the P-δ, P_S-δ_S and δ-δ_S plots corresponding to the rest of the specimens for the load-path 3a and 3b are given in the Appendices A3 (for 2mm) and A4 (for 16 mm). In Lytag concrete the matrix is stronger than the aggregate. Generally the crack patterns observed in Lytag concrete are less tortuous than for the 16 mm concrete. However, the final crack pattern observed for the Lytag concrete was in many respects different from that of 16 mm concrete and 2 mm mortar (See section 4.4 and Appendix A3 and A4). The reason is mainly the material structure and the chosen crack openings.

4.6 Influence of lateral confinement

4.6.1 Experiments

In the load-path 4 experiments, first a lateral compressive shear was applied in displacement control until P_S = -5, -10 kN or the maximum shear load corresponding to load-path 4a, 4b and 4c respectively. Subsequently, the lateral test control was changed to load control and an axial tensile load was applied in displacement control. In other words, a constant lateral confinement was maintained while the axial tensile force was activated. In Figs. 4.26a, b and c, the P_s-δ_s, P-δ and the δ-δ_s diagrams for the 200 mm specimens corresponding to load-paths 4a, 4b and 4c are shown. The shear load for these load-paths was -5, -10 and -27.5 kN (maximum shear) respectively.

For specimen 46-05 (Fig. 4.26a), the P_s-δ_s plot is linear till $P_s = -10$ kN. At $P_s = -10$ kN, the shear deformation δ_s, and the highest local deformation δ_i (Fig. 4.27a) corresponding to the measuring point 1 were 22 and 4 μm respectively. Point B on the P_s-δ_s diagram at $\delta_s = 22\mu$m for load-path 4b (Fig. 4.26a) corresponds to the activation of the tensile load. As can be seen in the δ_i- δ_s plot (Fig. 4.27a), the largest increase in δ_i first occurred at gauges 1 and 2 and subsequently at gauge 5. In Fig. 4.27b, the locations of the measuring points are identified. This confirms the crack initiation at the left and the right notches. The crack opening was faster at the left notch than at the right notch. Evidently, this crack initiation occurred during subsequent axial pulling at a constant lateral compressive shear (P_s) equal to 10 kN. The two overlapping curved cracks EF and GH with a compressive strut(enclosed area between EF and GH) in the middle were formed at the end of the test as shown in Fig. 4.28b. Specimen 48-03 subjected to load-path 4a behaved in a similar fashion. Meanwhile, the overlapping cracks AB and CD (Fig. 4.28a) were more flat compared to Fig. 4.28b and gave a smaller strut size.

For the specimen 47-06 with the maximum shear, the P_s-δ_s diagram became nonlinear at $P_s = -12.9$ kN and $\delta_s = 30\mu$m. This nonlinearity is due to the crack initiation at the front left notch (measuring point 1), and this can be seen in the δ_i-δ_s plot (Fig. 4.29a). Further shearing led to a maximum shear load of -27.5 kN at which time the shear deformation was 92.4 μm. As can be seen in Fig. 4.29a, the largest increase in δ_i occurred first at gauge 1, subsequently at gauges 11,6 ($\delta_{11} = \delta_6$) and 7. Gauges 1 and 11 were located near the left notch at the front and rear faces of the specimen. Evidently, the crack propagated on the front face of the specimen from the left notch to the location of gauge 7. This crack extension is identified as IJ on the crack pattern shown in Fig. 4.28c and 4.29c. However, on the rear face the fracture evolution was somewhat slower during the lateral shear. The crack on the rear face reached gauge 17 (located opposite to gauge 7) only after activating the axial tension.

The crack propagation during the lateral shear caused an increase of δ (note that the LVDTs were mounted near the notches). Point A on the P-δ diagram for load-path 4c (Fig. 4.26b) corresponds to the axial deformation due to the lateral compressive shear.(During the lateral compressive shear, a load-control was maintained in the axial direction, thereby $P = 0$). At A the axial tensile loading was activated, maintaining a constant lateral shear load of -27.5 kN (slightly below the maximum shear). As can be seen in Fig. 4.26b, soon after the

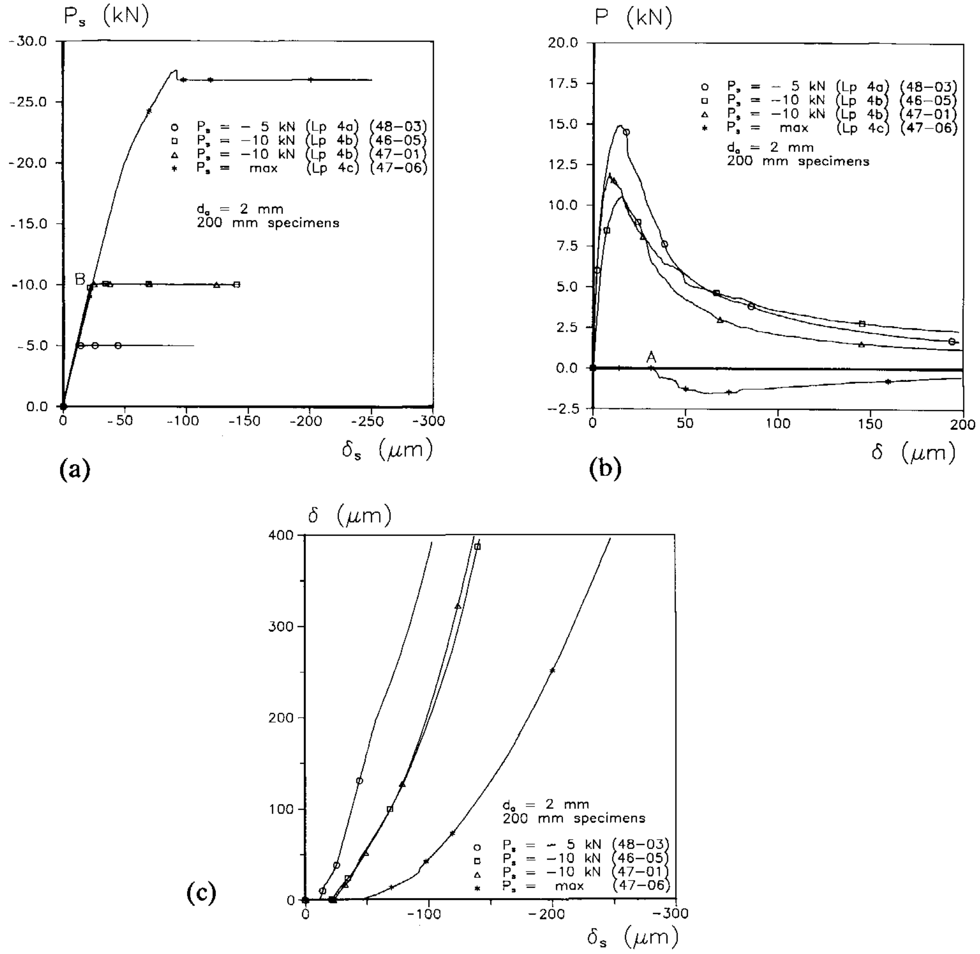

Figure 4.26 P_S-δ_S (a), P-δ (b) and δ-δ_S (c) response for 200 mm specimen corresponding to load-path 4 experiments.

activation of the axial load P became compressive. During the activation of the axial load crack KL initiated at the right notch.

The highest axial tensile load (15 kN) was measured in the test with the low shear load of -5 kN. A 30% decrease in P occurred when P_S was increased from -5 kN to -10 kN. *The presence of a lateral compressive shear load (or a lateral confinement) significantly affects the axial tensile capacity of the specimen.*

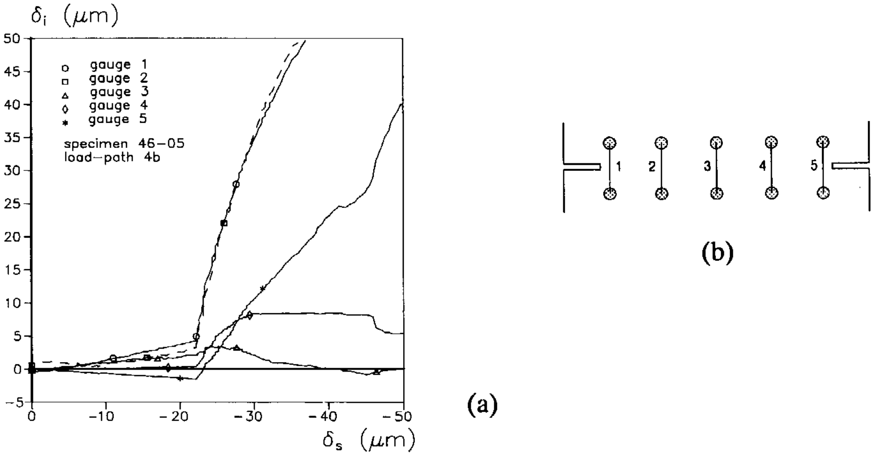

(a)

(b)

Figure 4.27 Local deforamtion versus lateral shear (δ_i-δ_s) and the location of measuring points for specimen 46-05 (load-path 4b).

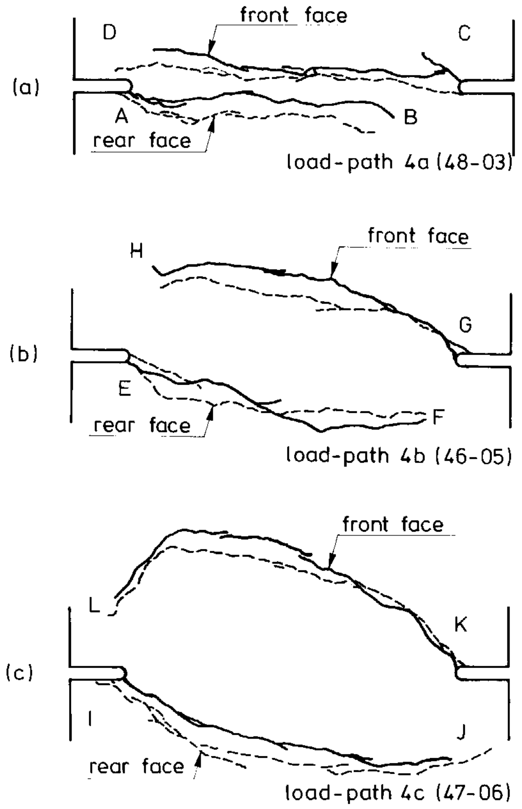

Figure 4.28 Crack patterns for the lateral confinement experiments (load-path 4).

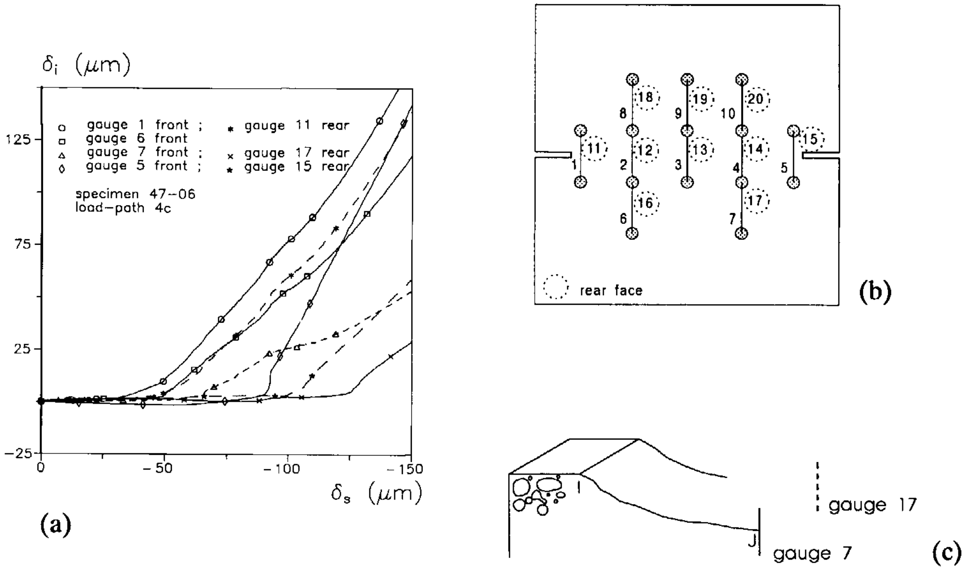

(a)

(b)

(c)

Figure 4.29 δ_i-δ_s (a), mesuring points (b), and crack evolution during the lateral shear (c), for load-path 4c experiment.

Fig. 4.28 shows the crack patterns for the load-path 4 experiments. *There seems to exist a relation between the lateral shear (or lateral confinement) load and the area of the compressive struts.* The specimen with the maximum shear load (Fig.4.28c) shows the largest strut area, whereas the specimen with the lowest shear (Fig. 4.28a) gives the smallest strut size. In all these specimens the crack initiated at an angle approximately equal to 45 degrees. Owing to the application of the lateral compressive shear and the axial tension, the stress state changes at the crack tip and the principal stress rotates. Due to this stress rotation, the crack propagates along a curvilinear path. The results of this load path might be used to tune the various crack models used in smeared finite element analysis (Rots[88]).

The double-notched beam geometry of Fig. 4.30a is often used for mixed-mode crack studies of concrete (eg. Taha & Swartz[88]). The crack pattern obtained in this beam (without an axial force) is shown in Fig. 4.30b, and shows great resemblance to the curved overlapping cracks obtained in the present studies with load-path 4 experiments (compare Figs.4.28c and 4.30b). Suppose the beam is sectioned along AB and CD as shown in Fig. 4.30c, such that the distance between them is equal to the beam depth d. This beam section can then be compared to the 200 mm DEN specimen used in this study (see Fig. 4.30d). As shown in Fig. 4.30c, the cross section is loaded with two shear loads near the notches as in the test beam and two bending moments at the faces AB and CD. For the DEN geometry, the loading condition is as shown in Fig.4.30d. In order to maintain the loading platens in a parallel position, a bending moment must evolve in the specimen machine assembly. In section 3.4.3, the transfer of bending moments through the plate spring assembly has been discussed.

In order to check the repeatability of the test results a small number of tests were duplicated in a random manner.In Appendix A5, (see Table A5) the test scheme corresponding to load-path 4, 5 and 6 is shown. As can be seen in Fig. 4.26b, two tests of P_S = -10 kN were repeated. There exists some deviations in the pre-peak behaviour of specimens 46-05 and 47-01. The observed discrepancy can likely be attributed to the difference in the age of loading (48 and 157 days respectively). However, self similar crack patterns were observed for both specimens.

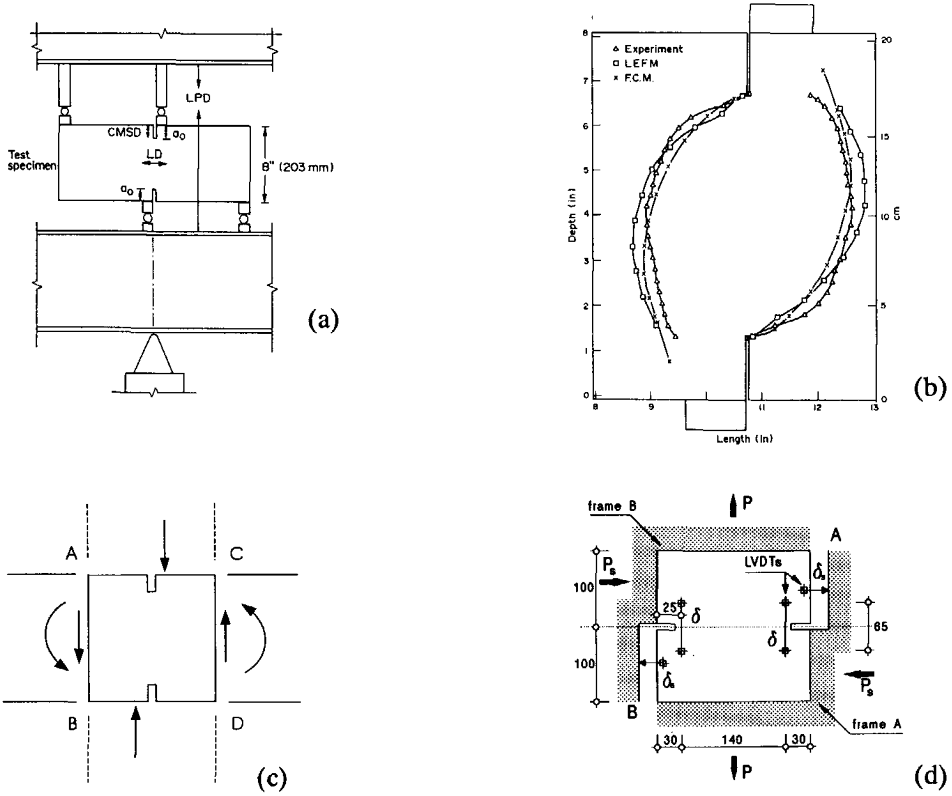

Figure 4.30 Comparison of the lateral confinement experiments with the double-notched beam geometry of Swartz & Taha[90].

4.6.2 Numerical simulation

Numerical tools can be used to gain some insight into the fracture behaviour of concrete structures. Experimental research and numerical tools must play a complementary role in order to arrive at a better understanding of the behaviour of concrete. On the one hand numerical tools can be utilized to interpret the experimental observations, and on the other hand experimental results can be used to tune a numerical model.

The behaviour of the DEN specimens under rotating stress was simulated using the finite element package DIANA (de Borst et al.[84]). The element mesh adopted consisted of eight-noded elements which were integrated using nine-point Gauss quadrature. Non-linear analyses were carried out using the smeared crack concept. The material properties used in these simulations were: Young's modulus $E = 30000$ MPa, Poisson's ratio $\nu = 0.2$, tensile strength $f_{ct} = 3.3$ MPa, fracture energy $G_f = 100$ J/m, crack band width $h = 12.5$ mm and the shear retention factor $\beta = 0$ ($= 0.001$ to avoid numerical problems). The stress-crack opening diagram σ-δ proposed in (Reinhardt et al.[86]) was adopted. An incremental iterative procedure was adopted to solve the nonlinear equations. The arc length method introduced in (Riks[79]) was used to pass limits points in the load displacement space.

Load-path 4a and 4b experiments were simulated numerically and Figs. 4.31a and b show the computed P_s-δ_s and P-δ diagrams. (These analyses have been published before, see Nooru-Mohamed, Schlangen & Van Mier[90]). The calculated maximum load P for load-path 4a and 4b exceeded the experimental peak load by 80%(Fig. 4.31b). Also the post peak P-δ curves deviated from the actual experimental results, at Figs. 4.26b and 4.31b. The numerical analyses were stopped at $\delta = 45\,\mu$m because convergence could not be obtained anymore. In Figs. 4.32a and b the calculated crack patterns are plotted for load-paths 4a and 4b. The calculated crack patterns deviated only slightly from each other and are both rather flat. The curved overlapping cracks found in the experiments were not found in the analyses.

The discrepancy between the numerical and the experimental results can partly be explained from the poor reproduction of the stress gradient near the notch since relatively large elements were used.

However, the major reason is the fact that the adopted smeared crack model incorporates a local rate-independent stress strain relation. Due to this the set of equations that describe the homogeneous continuum become ill-posed. For such ill-posed boundary value problems, the crack propagation direction aligns with the mesh lines as recently demonstrated by Sluys & De Borst[92]. But, a smeared crack model incorporating a rate-dependent stress strain relation was not available at the time of these anlyses were performed.

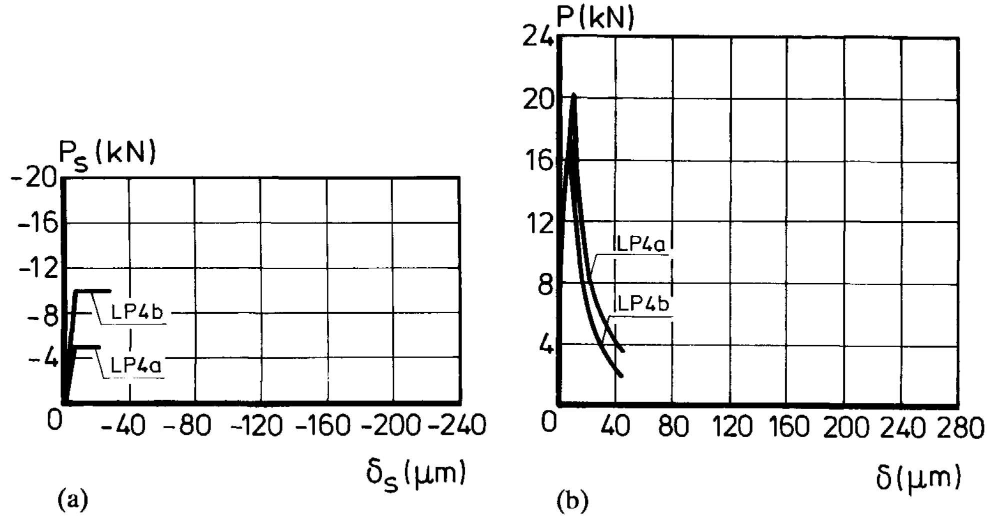

Figure 4.31 Simulated P_s-δ_s (a) and P-δ (b) diagrams for the load-path 4.

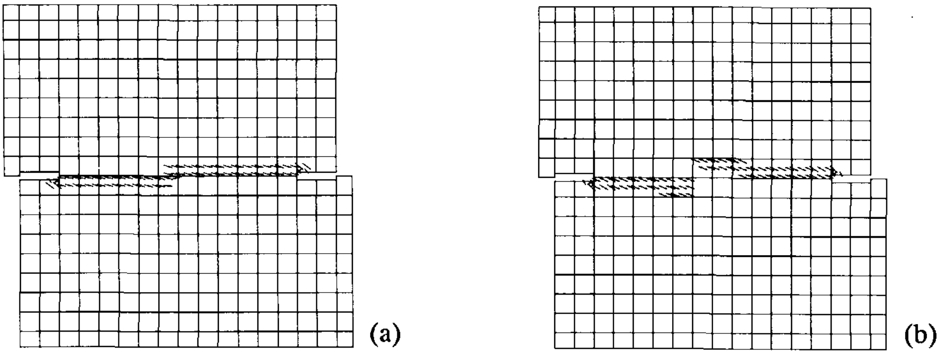

Figure 4.32 Simulated crack patterns for the load-path 4a and 4b.

4.7 Size related influence

In recent years the study on structural size effect of brittle disordered materials has gained prominence. In conventional strength theories, such as elastic allowable strength or plastic limit design, there is no dependence of the influence of the structure size on the nominal strength (σ_N). In a log σ_N - log (size) plot as shown in Fig. 4.33, the strength criterion is shown as a horizontal line. However, in a linear elastic fracture mechanics based approach σ_N decreases as the structure size increases, $\sigma_N = \text{constant}/\sqrt{d}$. This can be plotted as a straight line with a slope = -1/2 as shown in Fig. 4.33. In concrete LEFM is applicable only to very large structures. Therefore, the normal size structures fall in between the strength approach and the LEFM criterion. Futhermore, most of the laboratory size specimens are conventionally kept small and the extrapolation of the results into real structure size is at present done according to the strength criterion. Bazant has questioned this approach and has argued that the existing code provisions do not take fracture mechanics into account. Accordingly the formulation exhibits no size effect. The size effect law proposed by Bazant[85] is as follows.

$$\sigma_N = Bf'_t \,(a_0\xi^{-1} + 1 + a_1\xi + a_2\xi^2 + a_3\xi^3 + ...)^{1/2r} \quad ..... \; (4.5)$$

where $\xi = (d_a/d)^r$ and B, f'_t, r, a_o, a_1, ... are constants. It has been suggested that

$$\sigma_N = Bf'_t \,(1 + (d/(\lambda_o d_a))^r]^{-1/2r} \quad ...... \; .(4.6)$$

is probably sufficient for most applications.

It is worth noting the restriction in applying the size effect law. The size effect law can only be applied to geometrically similar specimens with monotonically increasing loading conditions. That is, the variation in the specimen must be in two dimensions only and the third dimension must remain a constant.

In here, an experimental study was undertaken to investigate the influence of the specimen size in mixed-mode fracture of concrete. Three load-paths, as discussed before namely the load-path 4, 5 and 6 (see section 4.1) were pursued for three specimen sizes,

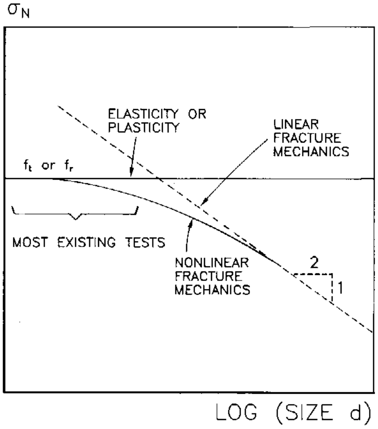

Figure 4.33 Schematic representation of the structural size effect.

viz., 200x200x50, 100x100x50 and 50x50x50 mm. The a/d ratio of 0.125 was adopted for all specimen sizes (where a = notch depth and d = specimen depth).

4.7.1 load-path 4 versus three specimen sizes

The load-displacement diagrams for load-path 4a, 4b and 4c with three different sizes are shown in Fig. 4.34a,b and c. As can be seen in Fig. 4.34a, the axial capacity reduces with decreasing specimen size in the presence of a lateral compressive shear load of 5 kN. A comparison can be made with the uniaxial tensile test. The 200 mm specimen 48-03 in Fig. 4.34a gives a lower axial load than the corresponding specimen 46-03 (load-path 0) in Fig.3.16. Thus the axial load decreases as the confinement increases from 0 to 5 kN, which was expected on the basis of the biaxial tension- compression tests, for example those by Kupfer & Gerstle[73].

The post peak behaviour for load-path 0 (Fig. 3.16) and 4a did not deviate significantly as shown in Fig. 4.34a. In Fig. 4.34b the P-δ plot for load-path 4b is shown for the three sizes. Two duplicate tests for the 200 mm specimens are shown in Fig. 4.34b. There is a difference in the peak values for the same test, which is partly caused by differences in the age at loading(47-01: 138 days and 46-05: 40 days). In the load-path 4b tests the intention was to apply the same lateral shear load of 10 kN to all the specimens irrespective of size. However, the 50 mm specimen posed a problem in terms of a stable test. As mentioned before, the lateral shear load P_S was applied under displacement control. It was observed that three out of five 50 mm specimens failed catastrophically as soon as the axial tensile load was applied. In these cases two cracks originated at the diagonally opposite corners of the specimen, viz. at the bottom left and the top right between the glue layers. Since the crack ran outside the control region, the specimen failed suddenly.

Therefore, the 10 kN shear load for the 50 mm specimen was too high and too close to the maximum shear load. It was thus decided to reduce the shear load level to 9 kN for the 50 mm specimen only. The P-δ curve for the 50 mm specimen is shown in Fig. 4.34b. Here, the maximum tensile load P reached was 850 N. In the post peak region the P-δ curve went into compression. In Fig. 4.34b, the reduction in axial load due to the decrease in specimen size is visible with a lateral confinement of 10 kN for the 200 mm and 100 mm, and 9 kN for the 50 mm specimens.

In Fig. 4.34c the P-δ plot for the load-path 4c is shown for the three sizes. Fig. 4.34c, soon after the activation of the axial load, P became compressive. The axial load in 50 and 200 mm specimen was in compression throughout the test. However, the axial load in the 100 mm specimen gradually reached tension. The reason for this phenomenon in the 100 mm specimen was not clear, also since, an increase in δ during shear was observed for all

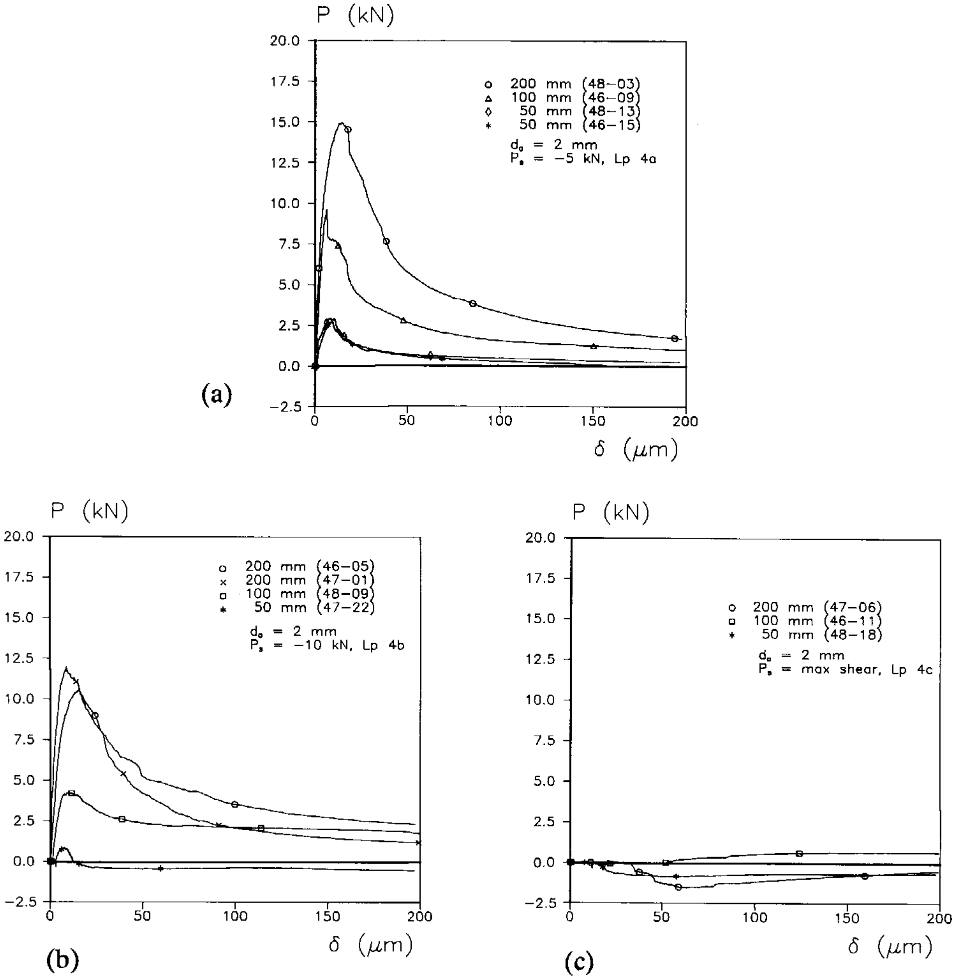

Figure 4.34 P-δ response for three different sizes (load-path 4).

three specimen sizes. This corresponds to crack initiation in all three specimens during the lateral shearing regime.

The final crack patterns corresponding to the load-path 4b for the 200, 100 and 50 mm specimens are shown in Fig. 4.35. Here, the 50 mm specimen is identified as load-path 4b* because of the reduction in the lateral shear load (9 kN). Interestingly, all three specimen sizes gave similar crack patterns for the same load-path (4b). The overlapping curved crack with a confined compressive strut is typical for this load-path. It can be concluded that the specimen size has no influence on the mode of failure, at least for the specimen ranges investigated.

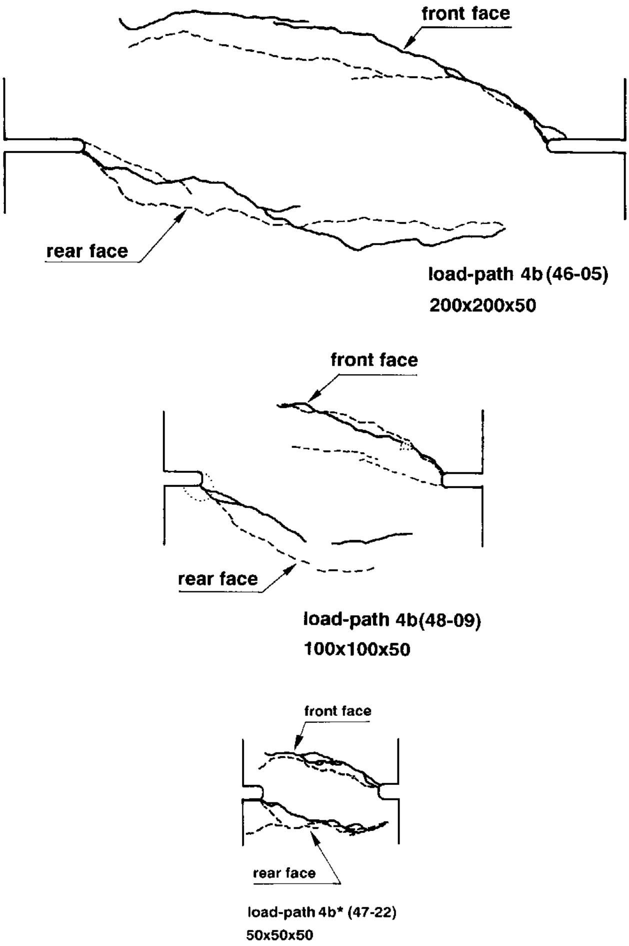

Figure 4.35 Self similar crack patterns obtained for three sizes in load-path 4b experiments.

4.7.2 load-path 5 versus three sizes

The test scheme corresponding to load-path 5 is given in the Appendix A5. In the load-path 5 experiments, first the lateral shear was applied in displacement control. After reaching the desired shear value, the axial tension was activated while maintaining displacement control in the lateral direction. Note that load-path 5 is different from the load-path 4 experiments. In the latter, the axial tension was activated while maintaining a load control in the lateral direction.

Fig. 4.36a and b show the P_S-δ_S and P-δ diagrams for load-path 5a experiments with three sizes. In this load-path, specimens with all three sizes were subjected to a 5 kN lateral compressive shear. As soon as the 5 kN shear was reached, the axial tension was activated, while maintaining a constant lateral deformation (deformation control). The corresponding P-δ diagram is shown in Fig. 4.36b. To maintain a constant lateral deformation during the axial tension, the lateral shear load has to decrease. As can be seen in Fig. 4.36a, the vertical line corresponds to the decrease in the lateral shear at P_S = -5 kN. For example, when the specimen 46-01 traced the complete P-δ diagram, the lateral shear load varied between -5 to -1.4 kN at a constant δ_S = 11.2 μm. Furthermore, the axial tensile load was unloaded at δ = 200 μm and as soon as P = 0, the axial test control was changed to load control. Thereafter, the lateral shear was activated for the second time.

In Fig. 4.36b, a decrease in the axial tensile capacity with the decrease in specimen size is seen. Here, a constant lateral deformation corresponding to P_S = -5 kN was maintained. A similar observation is found for larger lateral shear deformations at P_S = -10 and P_S = maximum shear (see Fig. 4.37b).

As can be seen in Fig. 4.36a, the specimen 46-01 reaches a shear peak load of 25.6 kN during the second shearing regime. It seems that the crack formed due to the axial tension has little influence on the ultimate shear capacity of the 100 and 200 mm specimens. The P_S-δ_S diagram in Fig. 4.37a shows the shear peak load for the un-cracked specimens. However, the shear stiffness during the first and the second shearing was 437.5 and 256.1 N/mm for the specimen 46-01 [load-path 5a]. This decrease in the shear stiffness is due to the formation of crack in a rotated biaxial stress field. Furthermore, the second shear

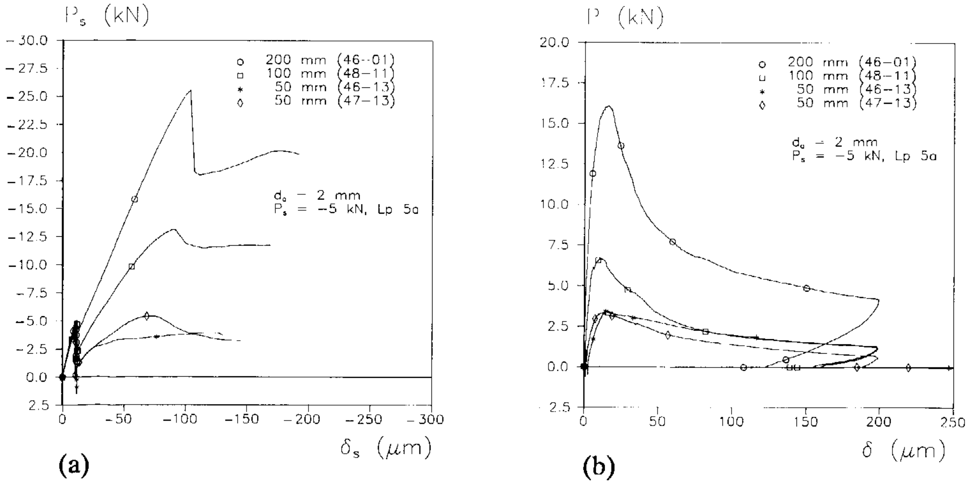

Figure 4.36 P_S-δ_S (a) and P-δ (b) response for three different sizes in load-path 5a experiments.

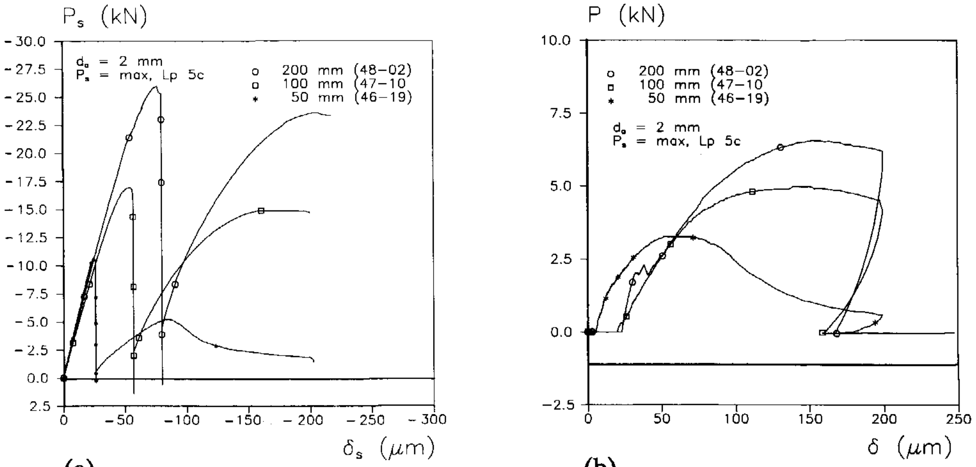

(a) (b)

Figure 4.37 P_S-δ_S (a) and P-δ (b) response for three different sizes in load-path 5c experiments.

stiffness decreases as the specimen size decreases. In all three specimens, a clear shear peak load was observed in the second shearing regime.

The crack patterns corresponding to the load-path 5a experiments for the three sizes are shown in Fig. 4.38a-c. The crack patterns related to load-path 5c are given in the Appendix A6. As can be seen in this figure the familiar overlapping curved crack is formed. There was no crack initiation during the first shearing sequence for the specimen 46-01. However, as soon as the axial force is activated the cracks A and B initiate at the left and the right notch of the specimen respectively. However, the growth of crack A was faster than that of crack B. At 200 μm, a command was given to unload the axial tension and subsequently the lateral shear was activated for the second time, at P = 0. Further extension of crack B on the front face, and the initiation of crack B* on the rear face took place during the second shearing regime. As can be seen in Fig. 4.36a, a sharp drop in the shear capacity of the specimen occurred at the shear peak load. Afterward a gradual increase in shear is seen. The drop from 25.6 kN to 18.0 kN is associated with further crack propagation in the specimen. In this load-path 5a, the familiar overlapping crack is seen. However, an additional secondary crack C formed from the crack A to the free edge of the specimen. When the lateral shear force dropped from 25.6 kN to 18.0, the vertical deformation δ increased from 129.0 to 183.6 μm. The secondary crack C runs in between the measuring length of the left LVDT. Therefore, this drop in shear force can be attributed to the secondary cracking.

The formation of overlapping curved cracks with a compressive strut is a consequence of the rotated stress state due to shear followed by tension in a specimen. Self similar crack patterns in load-path 4b and 5a suggest that the fracture mechanisms in both situations are alike. In load-path 4b and 5a experiments, the axial tensile force was activated when a lateral shear load was present. However, in load-path 4b, the magnitude of the lateral shear was a constant (i.e., -10 kN), whereas in load-path 5a it varied between -5 to 0 kN.

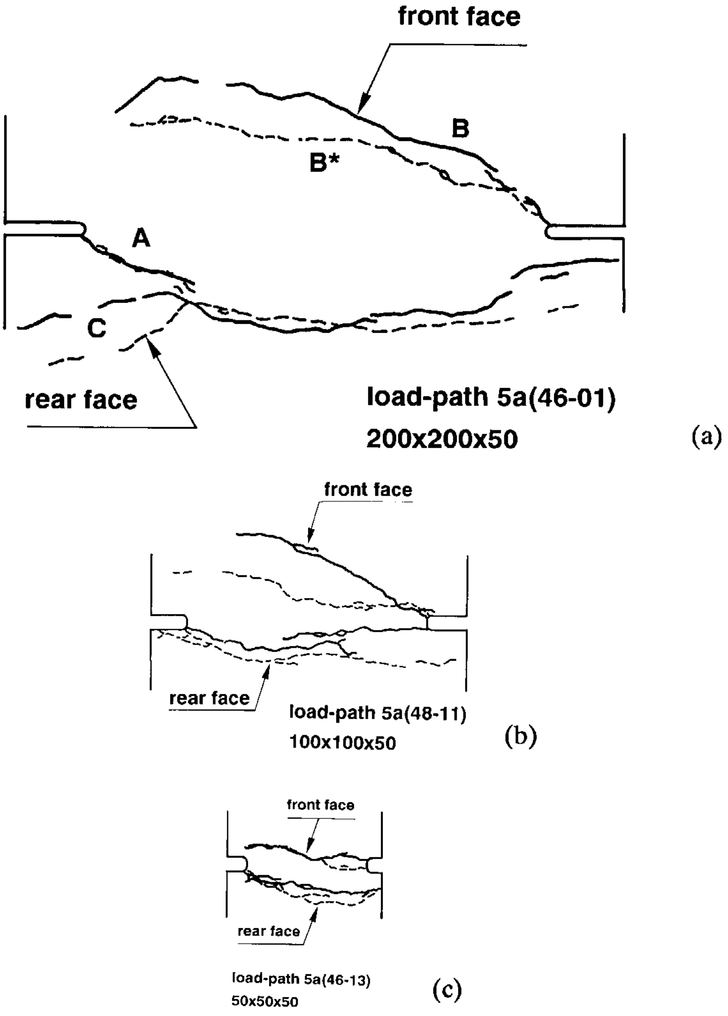

Figure 4.38 Crack patterns obtained for three sizes in load-path 5a experiments.

4.7.3 load-path 6 versus three sizes

In this load-path the axial tensile load and the lateral shear load were applied such that the ratio $\delta/\delta_S = 1.0$. In Fig. 4.39a and b the P/P_{max} - δ and P_S - δ_S plots are shown for the load-path

6a tests. The axial load was normalized with respect to the maximum tensile load P_{max} for each individual test. Because the maximum shear load $P_{s,max}$ was not reached in all tests, the P_S-δ_S diagrams have not been normalized.

As can be seen in Fig. 4.39a, the post peak normalized curves go to compression in the presence of a lateral shear in these proportional load-path experiments. A clear indication of the influence of specimen size is seen in this set of curves. As the size increases the steep drop of the normalized P/P_{max}-δ curve is greatly reduced. Each test was duplicated and the results of Fig. 4.39 indicate that an acceptable repeatability was obtained.

In spite of the good agreement in P-δ response between the 200 mm tests (47-02 and 46-02) two different crack patterns were observed, see Fig. 4.40a and b. The deviations in cracking may have caused by the unintentional difference in notch depth in the two specimens (viz. 20.3 and 26.1 mm respectively for specimens 47-02 and 46-02). The final crack pattern obtained for the specimen 47-02 is with two overlapping cracks with lower curvature. The curvature in the overlapping cracks disappears for the load-path 6 experiments. The order of crack growth for the specimen 46-02 was A,B and C (Fig. 4.40b).

The crack patterns for the 100 and 50 mm specimens are given in Fig. 4.40c,d,e and f. As can be seen in Fig. 4.40c and d, two identical test also gave two dissimilar crack patterns. From the local deformation measurements of the 100 mm specimen (48-08), the overlapping cracks D and E initiated during the proportional loading regime ($\delta/\delta_S = 1.0$). The crack D at the left notch initiated first. However, an identical test with the same δ/δ_S (= 1.0) ratio gave multiple diagonal shear cracks at the front and the rear faces of the specimen. In

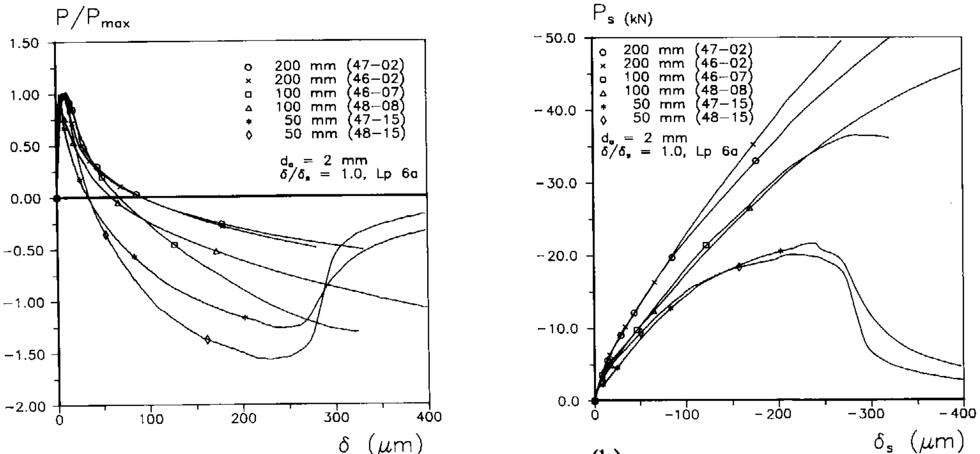

(a) (b)

Figure 4.39 P/P_{max}-δ (a) and P_S-δ_S (b) response for three sizes in load-path 6a experiments.

contrast, the P_S - δ_S curves for both tests were alike. (Fig. 4.39b, specimen 100). The 50 mm specimen reached a peak in compression in the normalized P-δ curve and gradually softened thereafter. This compressive peak and the subsequent gradual decrease in axial force was associated with a shear load peak followed by a gradual decrease in P_S. The phenomenon observed for the 50 mm specimen could have been observed for the 100 mm and 200 mm specimen as well if the capacity of the machine would have been larger than the available 50 kN in both directions.

The crack patterns related to the two 50 mm specimens are given in Fig. 4.40e and f. The familiar overlapping cracks disappear for the 50 mm specimens. Instead, diagonal multiple cracks form at the front and the rear faces of the specimen. For the specimen 47-15, the crack F became the dominant crack (front/rear faces), while the other cracks close to a

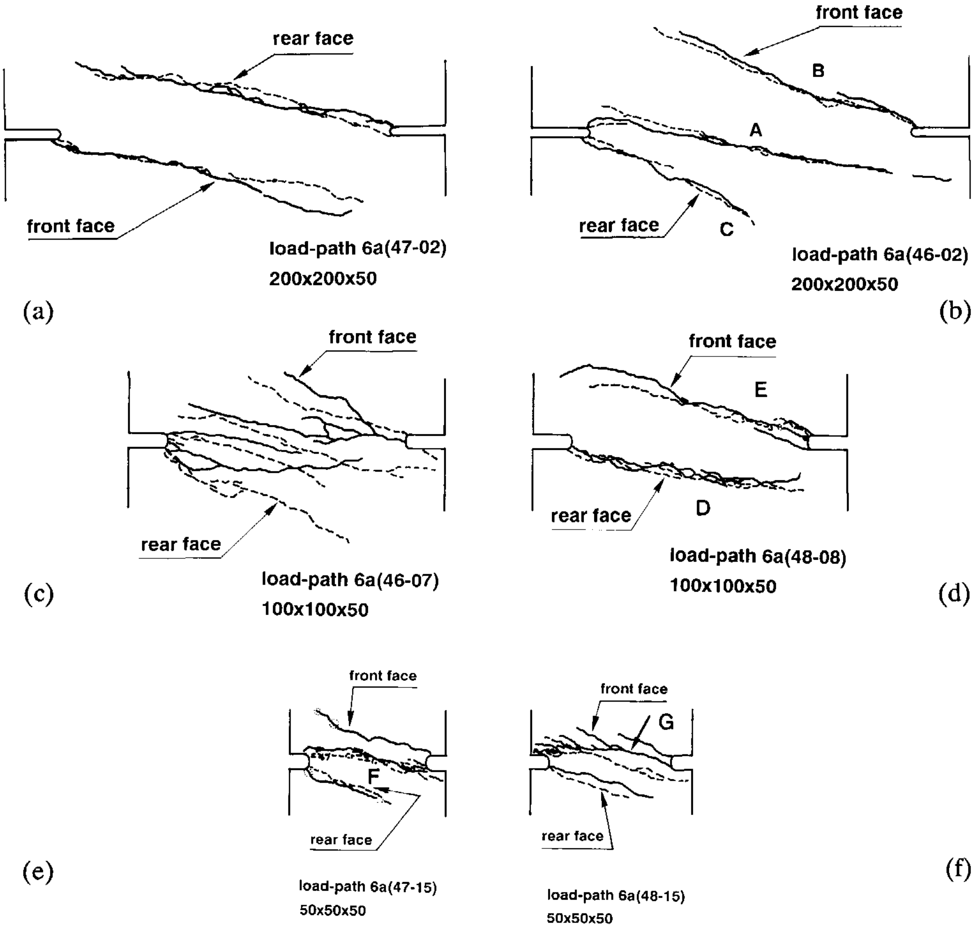

Figure 4.40 Crack patterns corresponding to three sizes in load-path 6a experiments.

certain extent. Moreover, a drop in the shear capacity for the 50 mm specimen is associated with the widening of the crack F (Fig. 4.40e). A similar observation was also made for the specimen 48-15, where widening of the crack G associated with the drop in the post peak shear. Moreover, the dominant crack was tortuous and many fissures appeared on the crack.

It can be concluded that, for the $\delta/\delta_S = 1.0$ experiments, a combination of failure modes exists. That is, the familiar overlapping crack and the inclined distributed crack. It is not clear which mode is dominant, since in the 200 and 100 mm specimens both modes appeared. Reduction in the specimen size always favored the diagonal multiple cracking mode.

In Fig. 4.41 and 4.42 the normalised P-δ curves and the P_S-δ_S plots for the load-path 6b and 6c experiments are shown. In the load-path 6b and 6c experiments, the post peak normalized P-δ curve (Fig. 4.41a 4.42a) gradually softened and fell into a narrow band. The normalized P-δ curves for the load-path 6b and 6c tests showed no relation to the change in the specimen size. Moreover, the final crack patterns obtained for the load-path 6b and 6c experiments were without the familiar overlapping cracks. The detailed crack patterns for load-paths 6b and 6c experiments are shown in Appendix A.7.

From the above observations it appears that the influence of the lateral compressive shear vanished once the δ/δ_S ratio was increased to 2 and 3. Changing the δ/δ_S ratio from 1 to 2 led to a completely different post peak behaviour governed by mode I cracking, irrespective of the specimen size.

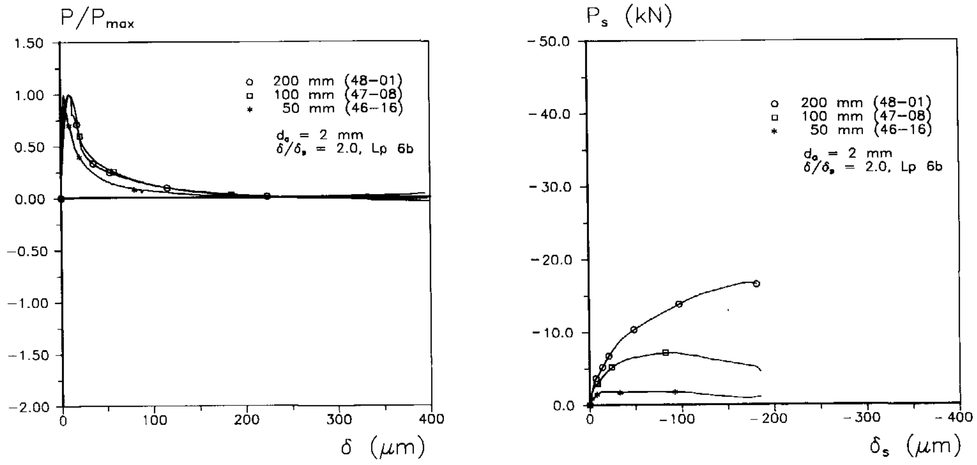

(a) (b)

Figure 4.41 P/P_{max}-δ (a) and P_S-δ_S (b) response for three sizes in load-path 6b experiments.

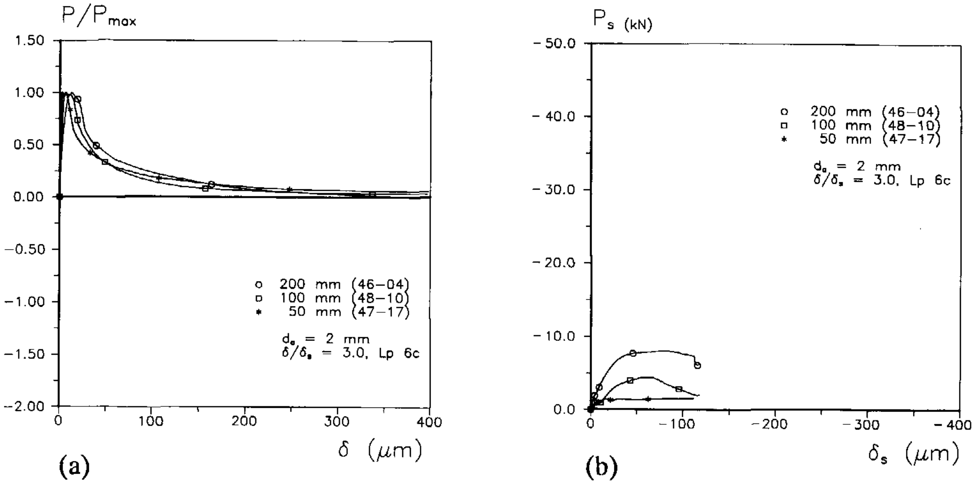

Figure 4.42 P/P_{max}-δ (a) and P_s-δ_s (b) response for three sizes in load-path 6c experiments.

a comparison with other mixed-mode results

Mixed-mode experiments were also performed at Lund Institute of Technology. Their aim was to obtain the mixed-mode properties of a process zone. Concrete cube specimens of size 70x70x60 mm with all four sides grooved at the middle were used in their studies. The net area available for fracture evolution was 40x40 mm. Among the three specimen geometries, the 50 mm DEN specimen falls closest to the cube specimen of Hassanzadeh[89]

In his experiments, Hassanzadeh[89] adopted parabolic and linear load-paths. The parabolic path was defined as $\delta = \eta\sqrt{\delta_s}$, where the value of η varied from 0.4 to 0.9. The linear path was assumed as $\delta = (\tan\alpha)\delta_s$, $\alpha = 30^0, 60^0$ and 75^0 respectively. Recently they also tried a mixed path combining the linear and the parabolic paths.

In the present test, the δ/δ_s ratios were $1.0(\alpha = 45^0)$, $2.0(\alpha = 63.4^0)$ and $3.0(\alpha = 71.6^0)$ for load-paths 6a,6b and 6c respectively. Even though, the prescribed δ/δ_s ratios specified were 2 and 3 (with $\alpha = 63.4^0$and 71.6^0), during the course of testing the δ/δ_s ratio varied as shown below.

δ/δ_s	corresponding α	α during testing	average
2	63.4	68.7 - 65.4	67.4
3	71.6	78.7 - 72.9	75.8

The deviation in α between the prescribed and the obtained deformation ratio was 4^0 (for $\delta/\delta_S = 2$) and 3.8^0 (for $\delta/\delta_S = 3$). These deviations can be considered minimal, however, further investigation is required to clarify this behaviour.

In Fig. 4.43a and b the σ-δ and σ_S-δ_S plots for the load-path 6 experiments are shown. In the same figure (Fig. 4.43), the σ-δ and σ_S-δ_S plots of Hassanzadeh, for $\alpha = 30^0$, 60^0 and 75^0 are compared. For $\alpha = 30^0$, and $\delta/\delta_S = 1.0$ experiments, the post peak σ-δ curve went into compression and reached an axial compressive peak stress. Afterwards the axial stress gradually decreased and stayed in the compression region. However, the axial compressive peak stress reached was higher in the present test with $\delta/\delta_S = 1.0$ as compared to $\alpha = 30^0$. Nevertheless, the post peak trend for the $\alpha = 30^0$ experiment is similar to the present test with $\delta/\delta_S = 1.0$. When the ratio δ/δ_S was changed to 2 (average $\alpha = 67.4^0$) and 3 (average $\alpha = 75.8^0$), the post peak σ - δ curve followed the familiar softening curve and entirely stayed in the tension region. However, for $\alpha = 60^0$and 75^0, the post peak σ-δ curve softened and stayed in the compression region. The σ-δ curves for $\delta/\delta_S = 3$ (average $\alpha = 75.8^0$) and $\alpha = 75^0$ were different, even though both tests had the same α.

When comparing the σ_S-δ_S diagrams of Hassanzadeh for $\alpha = 30^0$, with the present results for $\delta/\delta_S = 1.0$, an enormous difference in the peak shear stress and the post peak

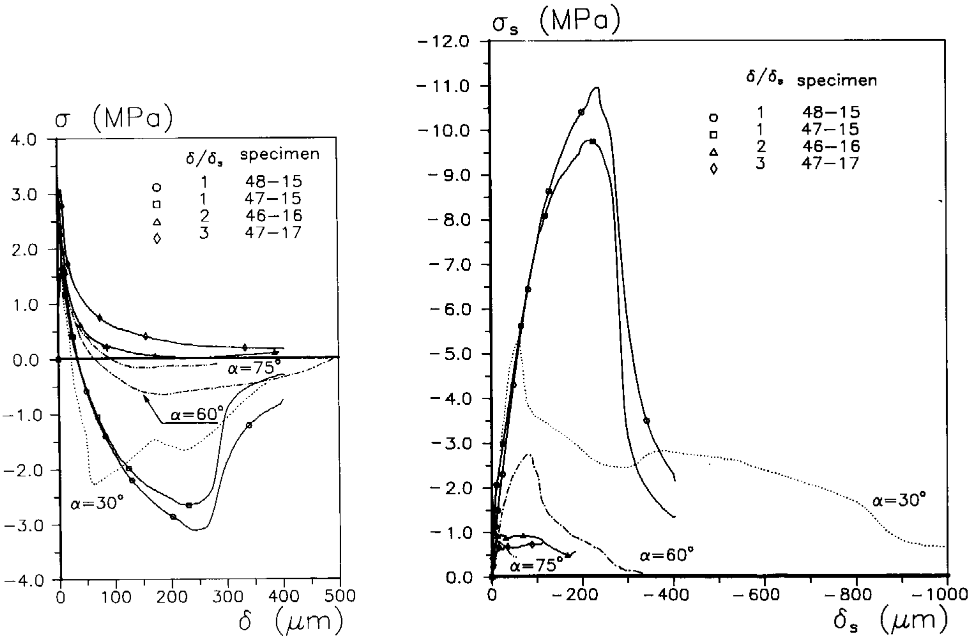

(a) (b)

Figure 4.43 Comparison of load-path 6a results with the linear path results of Hassanzadeh[89].

behaviour is observed. As can be seen in Fig. 4.43b, the largest shear deformation reached for the $\alpha = 30^0$ experiment of Hassanzadeh[89] was 1 mm.

These differences are due to the way in which the tests were performed in both places. The fracture mechanism in both tests can differ. There is no way to check the fracture evolution and the fracture mode etc. from the results of Hassanzadeh et al., since a circumferential notch in their specimens prevent from seeing it.

4.7.4 Size effect

In order to clarify the influence of size, the axial peak load P_{max} is plotted against the ligament length l (i.e. the distance between the notches) for each test. In Fig. 4.44a the data points corresponding to load- path 0 and 4 are plotted for three ligament lengths(size). Two observations can be made from this figure. First, irrespective of the size, the lateral load P_s(= 0, 2.5, 5, 10 kN and maximum shear corresponding to load-paths 0, $4a^*$, 4a, 4b and 4c) reduced the axial tensile peak load P_{max}. Secondly, an increase in P_{max} with increasing specimen size was observed irrespective of the level of lateral confinement excepting load-path 4c.

Moreover, Fig. 4.44b shows the size effect plot for load-path 5a, 5b and 5c. As can be seen in Fig. 4.44b, the axial capacity P_{max} increased with increasing specimen size. However, for the 50 mm specimen, the increase in lateral shear load has not significantly influenced the axial tensile peak load P_{max}. In these load-paths at the pre-determined shear load, axial tension was applied at a constant lateral deformation instead of a constant lateral confinement (load-path 4).

In addition, Fig. 4.44c shows the size effect plot for load-path 6a,6b and 6c, where the δ/δ_s ratio is 1.0, 2.0 and 3.0 respectively. As can be seen in Fig. 4.44c, the axial capacity P_{max} increased with increasing specimen size, for all three ratios of δ/δ_s. It seems that there is very little influence of the δ/δ_s ratio on the axial tensile peak load P_{max} in any particular size. This may be explained from the fact that the lateral compressive load is still relatively small. The biaxial tension compression experiments by Kupfer & Gerstle[73] suggest that the tensile capacity is not much affected by the presence of a small lateral compressive stress.

The results are compared with size effect law of Bazant[84]. The three specimen geometries adopted in the present experiments were compatible since the change in sizes was only in two dimensions. The same thickness was adopted for all experiments. Another requirement posed by the size effect formulation of Bazant[84] was that the load must increase monotonically. At this stage, it is not possible to compare all load-paths. Therefore, only the results of the load-path 0, and 6a tests were compared.

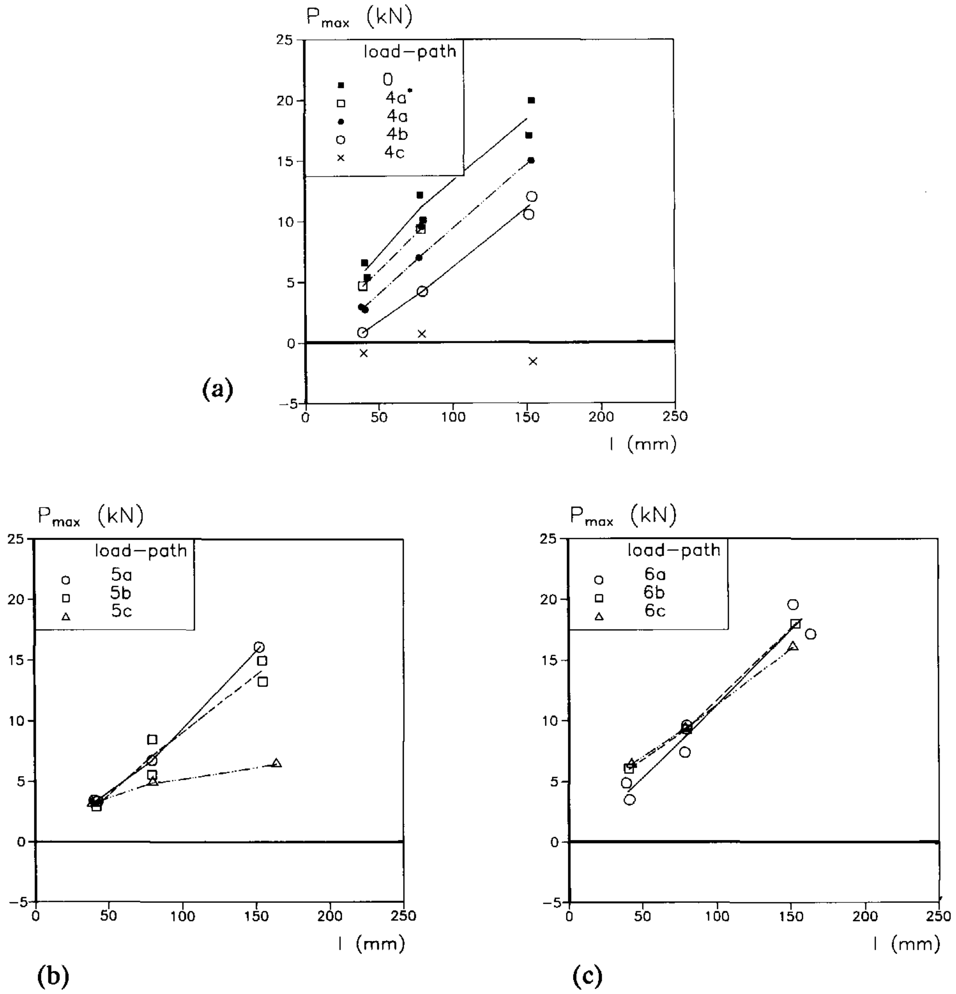

Figure 4.44 Axial peak load P_{max} versus ligament length l for load-path 4, 5 and 6.

The size effect law of Eq. (4.6) can be transformed to a linear plot

$$Y = AX + C \qquad (4.7)$$

in which

$Y = (f'_t/\sigma_N)^2$, $X = d/d_a$(d_a is the maximum aggregate size), $C = 1/B^2$ and $A = C/\lambda_0$.

The slope A and Y -intercept C can be easily determined by statistical regression. That would lead to the two unknown parameters in the size effect law: $B = 1/\sqrt{C}$ and $\lambda_0 = C/A$.

The error estimate of the regression analyses should be accompanied when reporting these constants. Accordingly, the coefficient of variation of the deviations from the regression line is $\omega_{y/x} = S_{y/x}/\bar{y}$, where $S_{Y/X}$ is the modified standard error estimate and is equal to $\{\sum[y_i - y_{est}]^2/(N-2)\}^{1/2}$. And $\bar{y}$ is the mean of the experimental Y values. Also the coefficient of correlation r is given by $\{ 1 - S^2_{y/x}/ S^2_y \}^{1/2}$, where S_y is the standard deviation.

load-path 0

Uniaxial tensile tests were performed with three different sizes namely 50, 100 and 200 mm. In Fig. 4.45a, the linear regression plot for 6 data points are shown. The analysis using Equation (4.7) yields coefficients $A = 0.014$, $C = 1.361$ and the error estimates $\omega_{y/x} = 0.243(24.3\%)$ and $r = 0.629$. Therefore, the parameters of Eq. (4.6) are $B = 0.857$ and $\lambda_0 = 97.214$. Fig. 4.45b shows the size effect curve Eq.(4.6) from the calculated parameters along with the experimental values of normalized nominal stress. The trend of the data is fitted reasonably well by the size effect law. As can be seen in Fig. 4.45b, three data points fall above and the other three below the size effect law. This is due to the number of loading platens used in the uniaxial tests. As discussed in section 3.4.1, higher tensile load was obtained when two loading platens were used. In Fig. 3.16 the influence of the loading platens are shown. It can be said that, irrespective of the number of loading platens in the uniaxial tensile test, the size effect law is valid.

load-path 6a

The linear regression plot for the six data points is shown in Fig. 4.46a (load-path 6a). The coefficients obtained from the analysis were $A = -0.019$, $C = 4.373$ and the error estimate $\omega_{y/x} = 0.652$ and $r = 0.428$. The unknown parameters B and λ_0 in the size effect law estimated from the above constants were 0.478 and -230.158 respectively.

In this load-path 6a experiments, each size is duplicated. However, the age of loading for the duplicate tests varied by 4, 3 and 2 months for the 50, 100 and 200 mm specimen sizes. As can be seen in Fig. 4.46b, the size effect law follows an opposite trend. As the specimen size increases, the size effect law diverges in contrast to the decrease in normalized axial stress. Most likely this difference is caused by the biaxial loading. Further testing is required to arrive at firm conclusions. In any future testing, extreme care must be paid to specimen preparations, especially when the specimen sizes are small.

The unknown parameters in the size effect law (Eq. (4.6)) are B and λ_0 which are empirical constants. The values of B and λ_0 are determined from the coefficients A and C which were obtained from a linear regression. For a clear perspective of the size effect law,

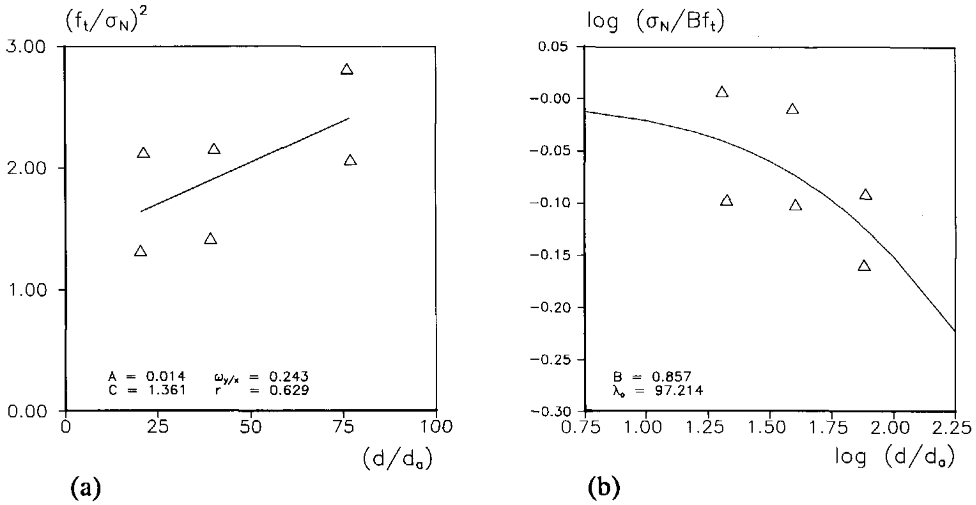

(a) (b)

Figure 4.45 Size effect plots for load-path 0 experiments.

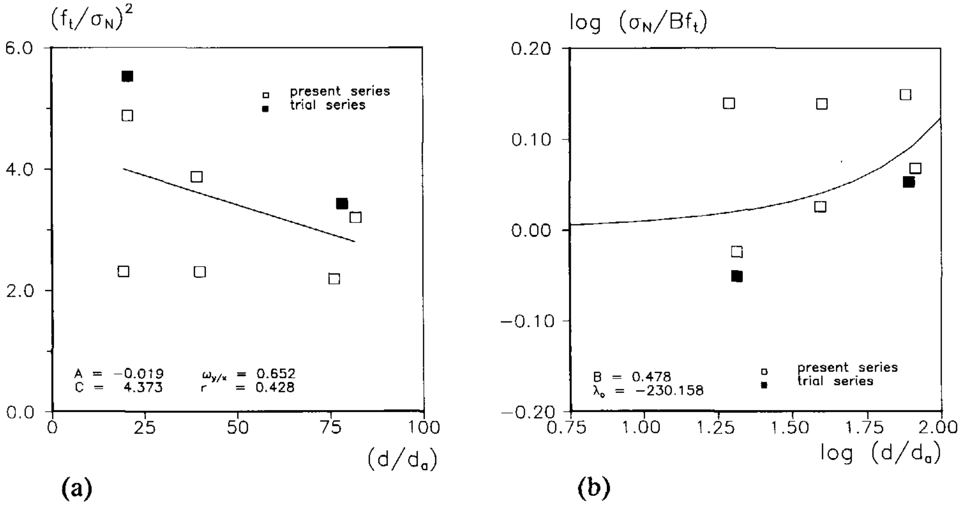

(a) (b)

Figure 4.46 Size effect plots for load-path 6a experiments.

the meaning and the physics behind these coefficients need to be looked into. The values of B and λ_0 depend on the geometrical shape of the structure, but not on its size. Bazant et al.[85] using a three-point bend test showed that the fractrue energy is inversely proportional to the slope A of the regression line of size effect. That is, $G_F = g(\alpha_0)/AE_c$, where $g(\alpha_0)$ is the shape function, $\alpha_0 = a_0/d$ (a_0 = notch depth, d = specimen depth) and E_c is the elastic modulus. They also claim that the Y-intercept (the coefficient C) of this line provides the remaining nonlinear fracture parameters. It is not clear whether same argument holds for other geometries too. In order to address the many problems with the fracture type size effects, the coefficients A, C, B and λ_0 need to be evaluated for a class of problems. If the size effect to be incorporated in the code provisons, then a serious effort must be made in determining the coefficients B and λ_0 for any concievable geometries which show size effect.

In Table 4.2, values of the four coefficients for some geometries reported in the literature are listed. Table 4.2 is arranged in an increasing order of B, the values ranged from 0.139 to 4.230. In the same table the B values obtained for the load-path 0 and 6a are listed. As far as the uniaxial test is concerned, the B value obtained from the present study (B = 0.857) is comparable to the value reported in the literature (B = 0.969).

Table 4.2

from the literature	B	λ_0	A	C
three point bending, HSC** (Gettu et al.[90])	0.139	3.444	15.010	51.700
torsion : notched cyllinder (Tokatly & Barr[91])	0.536	9.667	0.360	3.480
three point bending, NC* (Bazant & Pfeiffer[87])	0.589	5.402	0.533	2.880
torsion : plain beam (Bazant et al.[88])	0.830	6.339	0.229	1.450
uniaxial tension (Bazant & Pfeiffer[87])	0.969	16.800	0.063	1.065
double notched shear beam (Bazant & Pfeiffer[86])	1.647	36.800	0.010	0.369
eccentric compression (Bazant & Pfeiffer[87])	1.977	1.850	0.138	0.256
diagonal shear failure of beams without stirrups (Bazant & Kazemi[91])	4.230	1.867	0.030	0.056
present results				
load-path 0	0.857	97.214	0.014	1.361
load-path 6a	0.478	-230.16	-0.019	4.373

* Normal Concrete ; ** High Strength Concrete

4.8 Path dependence

So far, a systematic study on path dependence in mixed-mode fracture of concrete is lacking except for a few attempts reported in Nissen[87], Walraven & Keuser[88] and Hassanzadeh[89].

From the seven load-paths performed in this series, only four of them were chosen. They are load-paths 3b, 4, 5 and 6. To be able to compare, it is required to have the same dimension and the material structure. Accordingly, 200 mm specimens with 2 mm maximum aggregate size were chosen. For example, Fig. 4.47a shows the four crack opening paths δ-δ_S corresponding to four experiments (load-path 3b, 4b, 5b and 6b). As can be seen in this figure each crack opening path intersects the other in one or more points. The corresponding four P-P_S plot for the same load-paths 3b, 4b, 5b and 6b are shown in Fig. 4.47b.

In order to illustrate the procedure, in Fig. 4.47a, the crack opening paths δ-δ_S for the load-path 4b and 6b experiments are shown. The points of intersection between the crack opening paths 4b and 6b is identified as A. The corresponding loads P and P_S at the intersection A was retrieved from the experimental data. The difference between $P(= \Delta P)$ and $P_S(= \Delta Ps)$ for specimens pertaining to the two load-paths were calculated. The $\Delta P, \Delta P_S$ value was plotted as shown in Fig. 4.48. Similarly, $(\Delta P, \Delta P_S)$ values for the points of intersection for load-paths 4 and 6(circles in Fig. 4.53), 3 and 6(triangles) and 5 and 6 (square) were plotted in Fig. 4.48. It can be seen from Fig. 4.48 that the data points corresponding to the various load-paths discussed above were scattered throughout the diagram. The behaviour of the specimen would be path independent if $\Delta P = \Delta P_S = 0$, which is clearly not the case in the current tests.

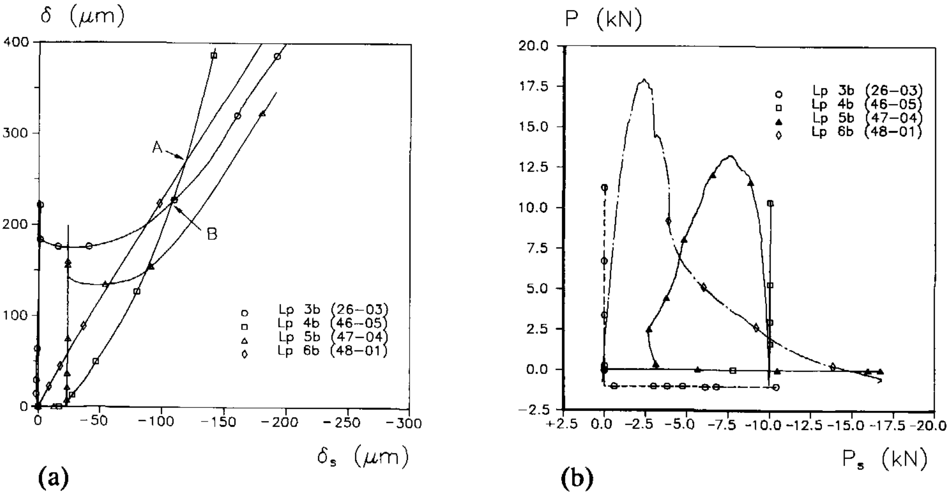

Figure 4.47 Crack opening paths δ-δ_S (a) and P-P_S response (b) for load-path 3b, 4b, 5b, 6b experiments.

For example, point B in Fig. 4.47a corresponds to the intersection between load-path 3b and 4b. It is now recalled how point B was reached. If load-path 3b was followed, then the specimen was pre-cracked first to 225 μm axial deformation and afterwards unloaded to a confinement of 0.13 MPa. Subsequently, a lateral compressive shear was applied. In this load-path, first a tensile crack formed and during unloading to a confinement the crack partially closed. Subsequent shearing lead to secondary cracking. The shearing process is associated with crack closing, free slip (nondilatant shear) and shear slip with fracturing as explained in section 4.4.1. However, if the load-path 4b was pursued, first a lateral compressive shear force was applied until a 10 kN shear force was reached. Afterward, the axial tension was activated maintaining the lateral compressive shear. Here two overlapping cracks formed. Even though both load-paths reached the same point (B), the underlying fracture mechanisms that prevail in both load paths are completely different. This leads to the path dependent behaviour. Also, in Fig. 4.47b, the P-P_S plot illustrates a completely different loading sequence for the load-path 3b and 4b.

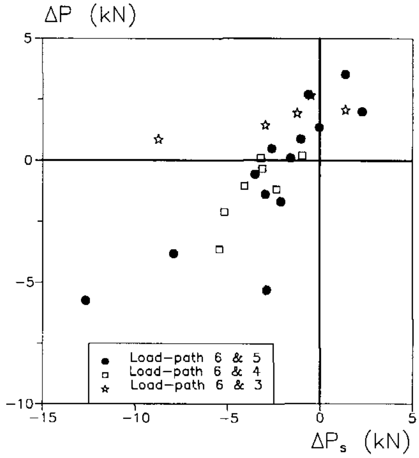

Figure 4.48 ΔP-ΔP_S plot: deviation in the intersection points in the P -P_S plane.

4.9 Failure mechanism

In Fig. 4.49 an overview of the failure modes related to the six load-paths are shown. From the discussions so far, five major fracture modes can be identified. They are: (1) tensile diagonal failure (2) sliding failure (3) formation of compressive struts (4) formation of overlapping curved cracks (5) transition between overlapping straight crack to inclined distributed crack. As can be seen in Fig. 4.49, the appropriate load-path, the external loading condition and the possible stress state inside the specimen related to each failure mode are shown. Moreover, in the last column of Fig. 4.49, the biaxial envelop is schematically drawn for load-path 1(b), 4, 5 and 6.

(1) *Tensile diagonal failure*: This failure mode was favoured under two boundary conditions: (a) tensile shear at a constant crack opening, equivalent to a confined tensile shear situation (load-path 1b), and (b) tensile shear at zero axial load, referred to as unconfined tensile shear (load-path 2). However, in the latter situation the axial crack opening was important and should be less than 250 μm in order to nucleate secondary diagonal cracking.

(2) *Sliding failure*: Sliding failure also occurred under two boundary conditions: (a) the unconfined tensile shear situation discussed in (1), but the axial crack openings were larger than 250 μm, and (b) compressive shear at zero axial load, referred to as unconfined compressive shear (load-path 3a). In the latter case, three materials were used, namely 2 mm mortar, 16 mm concrete and Lytag concrete. The crack openings were chosen between 200 to 400 μm depending on the material.

(3) *Formation of compressive struts*: This failure mode occurs when a sepecimen was subjected to a lateral compressive shear while a confinement across a partially opened crack plane was maintained. This situation is referred to confined compressive shear (load-path 3b). This failure mode was primarily observed for Lytag concrete. However, for 2 mm mortar and 16 mm concrete under the same boundary condition the above failure mode was not observed.

In the failure modes listed in (1), (2) and (3), the main features are secondary cracking or sliding. In situations such as unconfined tensile and unconfined compressive shear the mechanism was sliding. However, for the situation where confined tensile and confined compressive shear the mechanism was splitting due to secondary cracking. Furthermore, the axial crack opening during secondary crack formation was less than 200 μm. When formulating aggregate interlock theories, the formation of secondary cracks during shear at small crack openings was not considered. Often aggregate interlock theories were based on experiments where sliding occurred due to shear at large crack openings. Therefore, extending aggregate interlock theories to small crack openings is highly questionable.

(4) *Formation of overlapping curved cracks*: without pre-cracking the virgin specimen first shear and subsequently axial tension were applied at prescribed lateral shear load(load-path 4). Three specimen sizes were chosen and the overlapping curved cracks were formed in all three specimen sizes. The curved overlapping crack mode was also found in double edge notched beam geometries with rotating supports (Taha & Swartz[88], Van Mier et al.[92]). The

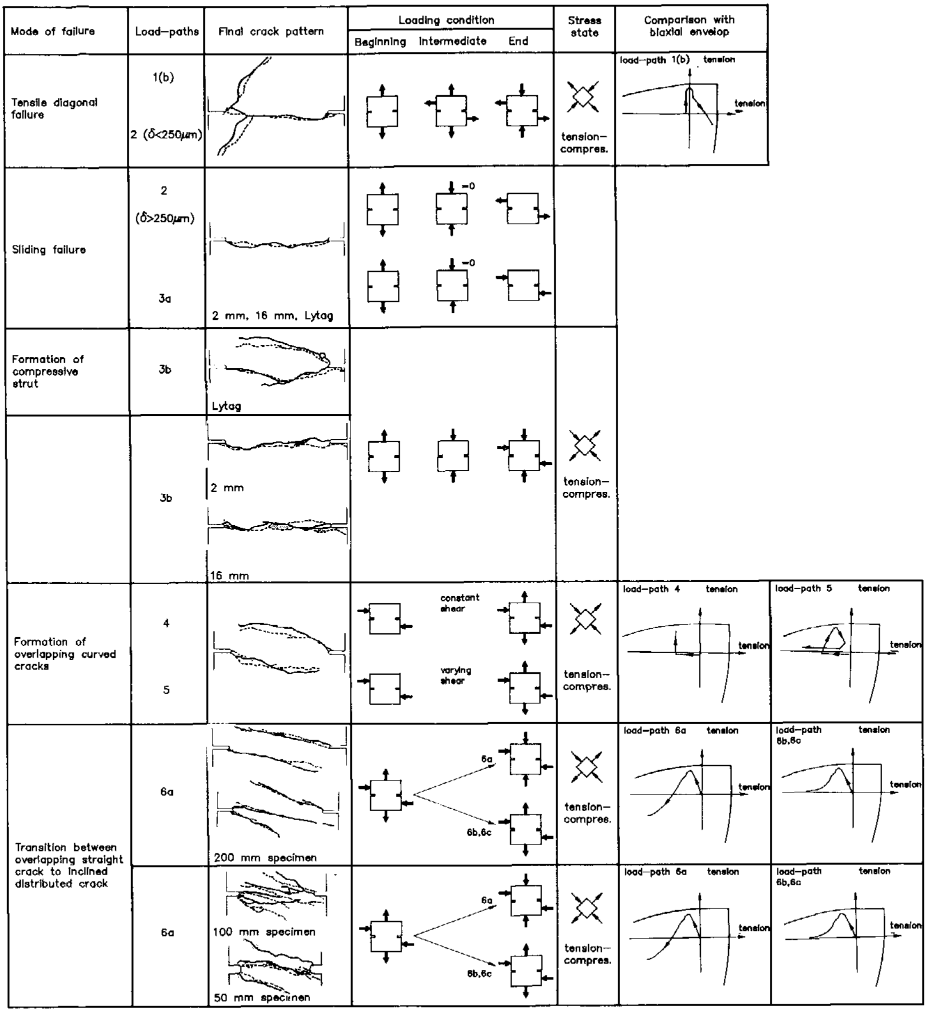

Figure 4.49 Overview of the failure mechanism involved in the various load-paths.

distance between the overlapping cracks depends on the amount of shear in the DEN plate specimens.

(5) *Transition between overlapping straight cracks to inclined distributed cracks*: Two types of failure modes were observed for large specimens (200 mm) when the lateral compressive shear and the axial tension were applied such that $\delta/\delta_S = 1.0$. The two failure modes were (a) two overlapping straight cracks (with lower curvature), and (b) inclined distributed

cracks. However the change of specimen size (50 and 100 mm) led to inclined distributed cracks under the same boundary condition. This aspect needs further investigation, in order to really identify the reason behind this phenomenon. One argument for this behaviour is that in the small specimen distributed fracture occurs due to confinement in the shear zone.

From the above discussion the importance of the boundary condition in shear fracture of concrete is highlighted. Proper numerical study can be used to illucidate this phenomenon.

5 Conclusions and Recommendations

In this investigation, crack growth under combined tension and shear is studied. For this purpose a recently developed biaxial machine was used. The biaxial machine consists of two independent loading frames which are capable of independently moving in the axial and the lateral directions.

Seven load-paths have been pursued. The testing technique is optimized such that any load-path can be followed in a fully automated way.

Double-Edge-Notched (DEN) (plate) geometries with three different sizes (constant thickness = 50 mm) were adopted in this study. Three types of materials, namely normal concrete of 2 and 16 mm maximum aggregate size and Lytag lightweight concrete of 12 mm maximum aggregate size were used.

The seven load-paths in this study can be classified into three broad categories: (1) an investigation of the shear strength or stiffness of partially opened cracks. Here, the specimens were pre-cracked under a tensile load to small crack openings within the range 0 to 400 μm, in a fully controlled condition. Thereafter, a lateral shear was applied. The results of these experiments were utilized to identify the role of aggregate interlock when the crack openings were small; (2) a study of the behaviour of concrete specimens which were first sheared (mode II) without pre-cracking and subsequently loaded in tension; (3) a study of the behaviour when tension (mode I) and shear (mode II) were acting simultaneously such that, the ratio of the axial (δ) to the lateral deformation (δ_s) remains a constant throughout the test.

The following conclusions are drawn:

It is recalled that tensile and compressive shear in this study is referred to the loading situation as shown in Fig. 4.1a and b.

A pre-cracked DEN specimen subjected to a lateral *compressive shear* under a constant crack opening showed no sliding. Under this condition the behaviour of the specimen was governed by a rotating biaxial compressive stress state.

For crack openings less than 250 μm, failure of the DEN specimens subjected to a lateral tensile shear at a constant crack opening, was due to the formation of diagonal tensile cracking.

A transition in fracture mode from tensile splitting to sliding failure was observed for the DEN specimens when the crack openings were larger than 250 μm. Here, a tensile shear load was applied to the specimen while a constant zero axial load normal to the crack plane.

From the above observations, the applicability of the conventional aggregate interlock theories at small crack openings is questionable. When the crack openings were relatively small, the shear transfer mechanism is not only aggregate interlock, but also secondary cracking.

A decrease in shear stiffness with increasing axial opening was observed for all three materials tested (2 mm mortar, 16 mm concrete and 12 mm Lytag). For Lytag concrete, when the axial confinement varied from 0 to 0.13 MPa, the failure mode changed from sliding to a failure mode in which compressive strut developed inclined to the crack plane. The above phenomenon was not observed for the other materials namely normal concrete of 2 and 16 mm maximum aggregate size. This point needs further investigation.

Two overlapping curved cracks formed between the notches when the specimen was subjected first to a lateral shear (mode II) and followed by tension (mode I). A one-to-one relation exists between the lateral compressive shear and the area of the compressive strut which formed between the two overlapping cracks. Also, the axial capacity of a DEN specimen is greatly reduced by the presence of a lateral compressive shear. Self similar overlapping crack patterns were observed for all three specimen sizes (200, 100 and 50 mm). That is to say , the specimen size has no influence on the mode of failure at least for the specimen ranges covered and pertinent to the load-path pursued(i.e., load-path 4).

For the experiments with the proportional ($\delta/\delta_s = 1.0$) load-path, where tension (mode I) and shear (mode II) were applied simultaneously, a combination of failure modes exists. When the specimen size was changed from 200 mm to 50 mm, the failure mode changed from formation of overlapping straight cracks to inclined distributed cracks. This indicates the relation between the specimen geometry and the failure mode. The size effect law of Bazant was compared with the results obtained in this load-path and shows an opposite effect. This may be due to the difference in failure modes which occur when the specimen geometry is changed.

The fracturing of DEN specimen subjected to mixed-mode loading is path dependent.

The experimental results reported in this thesis provide new data into the mixed-mode literature. The testing technique has been updated to a sufficient level where reliable results are obtained.

In order to clearly understand the behaviour of complex structures proper numerical analyses are required. However, the accuracy of the analyses to a large extent depends on the assumed constitutive models and crack modelling. As far as the crack modelling is concerned, in the smeared envirornment, fixed multi-directional or rotating crack concepts has been proposed. Often it was felt that the above crack concepts are not in contact with the current experimental fracture research. However, the present experimental results can be used to tune the various crack models available thusfar. In observed fracture mode in load-path 3 experiments (where first axial tension followed by lateral shear under an axial confinement) may come closer to the assumptions made in the fixed multi-directional crack concept. In the above concept, secondary cracks are allowed to form at the sampling point when the threshold angle α is exceeded. In addition, the load-paths 4, 5 and 6 fall in line with the assumptions made in the rotating smeared crack model. Therefore, the results can be used to verify and tune the model.

The shift in failure modes due to the change of specimen size indicate that the concept of matrial property is violated.

Further testing is required in order to fully capture some of the phenomena observed in this study.

(a) A transition from tensile splitting to sliding failure observed at $\delta > 250 \mu m$ was obtained for normal concrete of 2 mm maximum aggregate size. This needs to be investigated for other material structures.

(b) The transition from fracture mechanics to aggregate interlock needs a through investigation. As observed in this study, shear experiments on partially opened cracks showed secondary cracking at different boundary conditions.

(b) The proportional load-path requires further investigation, in order to substantiate the observation made in this study with regard to the size effect law of Bazant.

(c) In the proportional load-path experiments, the aspects of inclined distributed crack formation for small specimens needs further investigation.

(d) Specimen machine interaction needs further investigation in terms of numerical studies.

Notations

The following notations are used in this text

A = constant = slope of linear regression line

a = notch depth in mm

a_0 = constant

a_1 = constant

a_{ij} = coefficients

B = empirical constant used for the size effect law

$\mathbf{B}$ = $[B_{ij}]_{n,t}$, matrix corresponding to secant stress-crack displacement relation

C = intercept of linear regression line = Constant

$\mathbf{D}$ = $[D^{cr}{}_{ij}]_{n,t}$, crack secant stiffness matrix

d = specimen depth

d_a, d_{max} = maximum aggregate size

E = average Young's modulus

E_0 = Young's modulus computed from individual test

f_c = compressive strength (150 mm cubes)

f_t = tensile strength

f_{spl} = splitting tensile strength (150 mm cubes)

f_1, f_2 = functions of θ

G, G_0 = linear elastic shear modulus

G_c = critical energy release rate

G_{cr} = shear modulus of crcked concrete

G_F = fracture energy

G_t = total energy release

G_I = mode I energy release

G_{II} = mode II energy release

h = crack band width

K_c = citical stress intensity factor

K_{Ic} = mode I critical stress intensity factor

K_{II} = mode II stress intensity factor

l, l_{gauge} = gauge length

$M_{i(i=1,2,3,4)}$ = moments

P = axial load

P_{max} = maximum axial load

P_s = lateral shear load

r = radial distance

r = coefficient of correlation
r_0 = finite distance
S = strain energy density function
t = specimen thickness
w = crack width

α = threshold angle
β = shear retention factor or
angle between a crack and the Y axis
δ = axial deformation (65 mm gauge length)
δ_a = unloading axial deformation
δ_{a*} = true crack opening just before shear
δ_{el} = axial elastic deformation
δ_i = local deformation at measuring point i
(35 mm gauge length)
δ_n = crack opening
δ_s = global shear deformation
δ_t = crack sliding
ε = total strain
ε^{cr} = crack total strain
$\varepsilon^{cr}{}_{nn}$ = normal crack strain
$\Delta\varepsilon_{ij}$ = incremental strain
$i,j = n,t$
$\Delta\varepsilon^{co}$ = decomposed concrete incremental strain
$\Delta\varepsilon^{cr}$ = decomposed crack incremental strain
γ^{cr}_{nt} = shear crack strain
λ_0 = empirical constant
μ = reduction factor for mode I stiffness
ν = poisson's ratio
σ = average axial stress
$\Delta\sigma_{ij}$ = incremental stress
$i,j = n,t$
$\sigma^{c}{}_{nn}$ = normal stress along the crack surface
$\sigma^{c}{}_{nt}$ = shear stress along the crack surface
σ_θ = tangential stress
τ = average shear stress
$\omega_{y/x}$ = error estimate

References

Arrea, M. & Ingraffea, A.R. (1982). Mixed-mode crack propagation in mortar and concrete. Report No. 81-83, Department of Structural Engineering, Cornell University, Ithaca, New York.

Barenblatt, G.J. (1962). The mathematical theory of equilibrium crack in the brittle fracture. *Advances in Applied Mechanics*, **7**, 55-125.

Bazant, Z.P. & Gambarova P. (1980). Rough cracks in reinforced concrete. *Journal of the Structural Division, ASCE*, **106**, ST4, 819-842.

Bazant, Z.P. & Oh, B.H.(1983). Crack band theory for fracture of concrete. *Materials and Structures(RILEM)*, **16**, 93, 155-177.

Bazant, Z.P. (1984). Size effect in blunt fracture: concrete, rock, metal. *Journal of Engineering Mechanics, ASCE*, **110**, 4, 518-535.

Bazant, Z.P. & Gambarova, P. (1984). Crack shear in concrete: crack band microplane model. *Journal of Engineering Mechanics, ASCE*, **110**, 9, 2015-2035.

Bazant, Z.P. & Pfeiffer, P.A. (1985). Tests of shear fracture and strain- softening in concrete. In *Proceedings, 2nd Symposium on "The Interaction of Non-Nuclear Munitions with Structures,"* ed. P.Y. Thompson & A. Ross, University of Florida.

Bazant, Z.P., Kim, J.K. & Pfeiffer, P. (1985). Continuum model for progressive cracking and identification of nonlinear fracture parameters. In *Application of Fracture Mechanics to Cementitious Composites*,ed. S.P. Shah. Martinus Nijhof Publishers, The Hague, pp. 197-246.

Bazant, Z.P. & Pfeiffer, P.A. (1986). Shear fracture tests of concrete. *Materials and Structures(RILEM)*, **19**, 110, 111-121.

Bazant, Z.P. (1986). Mechanics of distributed cracking. *Applied Mechanics Review*, **39**, 5, 675-705.

Bazant, Z.P. & Pfeiffer, P. (1987). Fracture energy of concrete: its definition and determination from size effect tests. In *Concrete Durability, Volume I,* ACI SP-100, ed. J.M. Scanlon. ACI, Detroit, pp. 89-109.

Bazant, Z.P., Sener, S. & Prat, P.C. (1988). Size effect tests of torsional failure of plain and reinforced concrete beams. *Materials and Structures (RILEM)*, **21**, 425-430.

Bazant, Z.P. & Kazemi, M.T. (1991). Size effect on diagonal failure of beams without stirrups. *ACI Structural Journal,* **88**, 3, 268-275.

Broek, D. (1984). *Elementary engineering fracture mechanics,* Martinus Nijhof Publishers, The Hague.

Broek, D. (1988). *The Practical Use of Fracture Mechanics,* Kluwer Academic Publishers, Dordrecht.

Carpinteri, A. (1985). Interpretation of the Griffith instabilities a bifurcation of the global equilibrium. In *Application of Fracture Mechanics to Cementitious Composites,* ed. S.P. Shah. Martinus Nijhof Publishers, The Hague, pp. 287- 316.

Carpinteri, A. (1986). *Mechanical damage and crack growth in concrete,* Martinus Nijhoff Publishers, Dordrecht.

Carpinteri, A., Ferrara, G., Melchiorri, G. & Valente, S. (1990). The four point shear test in single notched specimens: an experimental and numerical analysis. In *Fracture Behaviour and Design of Materials and Structures*, ed. D. Firrao. EMAS Publishers, Warley, pp. 667-675.

Chen, W.F. & Saleeb, A.F. (1982). *Constitutive equations for engineering materials, Vol I,* John Wiley & Sons, New York.

De Borst, R., Kusters, G.M.A., Nauta, P. & de Witte, F.C. (1984). DIANA: A three-dimensional, nonlinear finite element package on a micro-computer. In *Engineering Software for Micro-computers,* ed. B.A. Schrefker, R.W. Lewis & S. A. Odonizzi. Pineridge, Swansea, pp.435-446.

De Borst, R. & Nauta, P. (1985). Non-orthogonal cracks in a smeared finite element model. *Engineering Computations*. **2**, 35-46.

De Borst, R. (1986). Non-linear analysis of frictional materials. PhD thesis, Delft University of Technology, Delft, The Netherlands.

De Borst, R. (1991). Computational Methods in non-linear solid mechanics, part2: physical non-linearity. Report No. 25-2-91-2-06, Delft University of Technology, Delft, The Netherlands.

Dugdale, D.S. (1960). Yielding of steel sheets containing slits. *Journal of Mechanics and Physics of Solids*, **8**, 100-104.

Erdogan, F. & Sih, G.C. (1963). On the crack extension in plates under plane loading and transverse shear. *Journal of Basic Engineering, Transaction of the ASME*, **85**, 519-527.

Fardis, M. & Buyukozturk, O. (1979). Shear transfer across cracks in reinforced concrete. *Journal of the Engineering Mechanics Division,ASCE*, **6**, *EM2*, 255-275.

Feenstra, P., De Borst, R. & Rots, J. (1991*a*). Numerical study on crack dilatancy. I: models and stability analysis. *Journal of Engineering Mechanics, ASCE*, **117**, 4, 733-753.

Feenstra, P., De Borst, R. & Rots, J. (1991*b*). Numerical study on crack dilatancy. II: application. *Journal of Engineering Mechanics, ASCE*, **117**, 4, 754-769.

Gettu, R., Bazant, Z.P. & Karr, M.E. (1990). Fracture properties and brittleness of high-strength concrete. *ACI Materials Journal*, **87**, 6, 608-618.

Gdoutos, E.E (1984). *Problems of mixed mode crack propagation*, EAFM series. Martinus Nijhof Publishers, The Hague.

Gdoutos, E.E. (1990). *Fractiure Mechanics Criteria and Applications*, Kluwer Academic Publishers, Dordrecht.

Hassanzadeh, M., Hillerborg, A. & Zhou, F.P. (1987). Test of Material properties in mixed mode I and II, In *Proceedings SEM/RILEM Conferece on Fracture of Concrete and Rock*, ed. S.P. Shah & S.E. Swartz, SEM, Bethel, pp. 353-358.

Hassanzadeh, M. (1989). Determination of fracture zone properties in mixed mode I and II , In *Proceedings of the 1989 SEM spring Conference on Experimental Mechanics*, Cambridge, MA. pp. 521-527.

Hillerborg, A., Modeer, M. & Petersson, P-E. (1976). Analysis of crack formation and crack growth in concrete by means of fracture mechanics and finite elements. *Cement and Concrete Research*, **6**, 773-782.

Hillerborg, A. (1985a). Influence of beam size on concrete fracture energy determination according to a draft RILEM recommendation. Report TVBM-3021, Division of Building Materials, Lund Institute of Technology, Lund, Sweden.

Hillerborg, A. (1985b). Numerical methods to simulate softening and fracture of concrete. In *Fracture Mechanics of Concrete,* EAFM series, ed. G.C. Sih & A. Ditommaso. Martinus Nijhoff Publishers, Dordrecht, pp. 141-170.

Hordijk, D.A., Reinhardt, H.W. & Cornelissen, H.A.W. (1987). Fracture mechanics parameters of concrete from uniaxial tensile tests as influenced by specimen length. In *Proceedings SEM/RILEM Conference on Fracture of Concrete and Rock*, ed. S.P. Shah & S.E. Swartz. SEM, Bethel, pp. 138-149.

Hordijk, D.A., Van Mier, J.G.M. & Reinhardt, H.W. (1989). Material properties, chapter 4. In *Fracture Mechanics of Concrete Structures From Theory to Applications*, ed. L. Elfgren. Chapman & Hall Publishers, London/New York, pp. 67-127.

Hsu, T.T.C., Slate, F.O., Sturman, G.M. & Winter, G.(1963). Microcracking of plain concrete and the shape of the stress-strain curve. *Journal of the American Concrete Institute*. **60**, 2, 209-224.

Ingraffea, A. & Saouma, V. (1985). Numerical modeling of discrete crack propagation in reinforced and plain concrete. In *Fracture Mechanics of Concrete*, EAFM Series, ed. G.C. Sih & A. DiTommaso. Martinus Nijhoff publishers, Dordrecht, pp. 171-222.

Ingraffea, A.R. & Panthaki, M.J. (1985). Analysis of "shear fracture" tests of concrete beams. In Finite Element Analysis of Reinforced Concrete Structures, ed. C. Meyer & H. Okamura. ASCE, New York, pp. 151-173.

Iosipescu, N. (1967). New accurate procedure for single shear testing of metals. *Journal of Materials*. **2**, 537-566.

Kaplan, M.F. (1961). Crack propagation and the fracture of concrete. *Journal of the American Concrete Institute*. **58**, 5, 591-610.

Keuser, W. & Walraven, J. (1988). Fracture of plain concrete under mixed mode conditions. In *Fracture of Concrete and Rock - Recent Developments*, ed. S.P. Shah, S.E. Swartz & B. Barr. Elsevier Applied Science Publishers, London/New York, pp. 625-634.

Kupfer, H.B. & Gerstle. K.H.(1973). Behaviour of concrete under biaxial stress. *Journal of the Engineering Mechanics Division, ASCE*, **199**, *EM4*, 853- 866.

Laible, J.P., White, R.N. & Gergely, P.(1977). Experimental investigation of seismic shear transfer across cracks in concrete nuclear containment vessels. In *Reinforced concrete structures in seismic zones*, ACI SP-53, ACI, Detroit, pp. 203-226.

Li, B., Maekawa, K. & Okamura, H. (1989). Contact density model for stress transfer across cracks in concrete. *Journal of the Faculty of Engineering*. University of Tokyo, **40**, 1, 9-52.

Millard S. & Johnson, G. (1986). Discussion of the paper "shear transfer in reinforced concrete". *Magazine of Concrete Research*, **38**, 134, 50-51.

Mindess, S. (1984). Fracture toughness testing of cement and concrete. In *Fracture Mechanics of Concrete: Material Characterization and Testing*, EAFM Series, ed. A. Carpinteri & A. Ingraffea. Martinus Nijhoff Publishers, The Hague, pp. 67-110.

Mindess, S. (1991). Fracture process zone detection. In *Fracture Mechanics Test Methods for Concrete*, ed. S.P. Shah & A. Carpinteri. Chapman & Hall, London/New York, pp. 231-261.

Ngo, D. & Scordelis, A.C. (1967). Finite element analysis of reinforced concrete beams. *Journal of American Concrete Institute*. **64**, 3, 152-163.

Nissen, I. (1987). Rissverzahnung des Betons. - Gegenseitige Rißuferverschiebungen und übertragene Kräfte. PhD thesis, Technical University Munich, Munich, Germany.

Nooru-Mohamed, M.B. & Van Mier, J.G.M.(1989). Fracture of concrete under mixed-mode loading. In *Fracture of Concrete and Rock - Recent Developments*, ed. S.P. Shah, S.E. Swartz & B. Barr. Elsevier Applied Science Publishers, London/New York, pp. 458-467.

Nooru-Mohamed, M.B., Schlangen, E & Van Mier J.G.M. (1990). Fracture of concrete plates subjected to rotating biaxial stress. In *Fracture Behaviour and Design of Materials and Structures*,ECF8, ed. D. Firrao. EMAS publishers, Warley, UK, pp. 682-687.

Nooru-Mohamed, M.B. & Van Mier J.G.M. (1991). Size effects in mixed-mode fracture of concrete. In *Fracture Processes in Concrete, Rock and Ceramics*, ed. J.G.M. van Mier, J.G. Rots & A. Bakker. Chapman & Hall Publishers, London/New York, 461-471.

Paulay, T. & Loeber, P.J. (1974). Shear transfer by aggregate interlock. In *Shear in Reinforced concrete Volume I*, ACI SP-42. ACI, Detroit, 1-16.

Petersson, P.E. & Gustavsson, P.J.(1980). A model for calculation of crack growth in concrete-like materials. In *Numerical Methods in Fracture Mechanics*, ed. D.R.J. Owen & A.R. Luxmoore. Pineridge Press, Swansea, pp.707-719.

Petersson, P.E. (1981). Crack growth and development of fracture zones in plain concrete and similar materials. Report TVBM-1006, Division of Building Materials, Lund Institute of Technology, Lund, Sweden.

Pruijssers, A.F. (1988). Aggregate interlock and dowel action under monotonic and cyclic loading. PhD thesis, Delft University of Technology, Delft. The Netherlands.

Rashid, Y.R. (1968). Analysis of prestressed concrete pressure vessels. *Nuclear Engineering and Design,* **7**, 4, pp. 334-344.

Read, H.E. & Hegemier, G.A. (1984). Strain softening of rock, soil and concrete - a review article. *Mechanics of Materials*, **3**, 271-294.

Reinhardt, H.W., Cornelissen, H.A.W. & Hordijk, D.A. (1987). Tensile tests and failure analysis of concrete. *Journal of Structural Engineering*, ASCE, **112**, 11, 2462-2477.

Reinhardt, H.W., Cornelissen, H.A.W. & Hordijk, D.A. (1989). Mixed mode fracture tests on concrete. In *Fracture of Concrete and Rock*, ed. S.P. Shah & S.E. Swartz. Springer Verlag, New York, pp. 117-130.

Riks, E. (1979). An incremental approach to the solution of snapping and buckling problems. *International Journal of Solid and Structures*, **15**, 529-551.

Rots, J.G., Kusters, G.M.A. & Nauta, P. (1984). Variable shear retention factor for the shear resistance of cracked concrete. Report No. BI-84-33, Institute TNO for Building Materials and Structures, Rijswijk, The Netherlands. (in Dutch)

Rots, J.G., Nauta P., Kusters, G.M.A. & Blaauwendraad, J. (1985). Smeared crack approach and fracture localization in concrete. *HERON*. **30**, 1, 1-48.

Rots, J.G., Hordijk, D.A. & De Borst, R. (1987). Numerical simulation of concrete fracture in 'direct' tension. In *Numerical Methods in Fracture Mechanics*, ed. A.R. Luxmoore, D.R.J. Owen & Y.P.S. Rajapakse. Pineridge Press, Swansea, pp. 457-471.

Rots, J.G. & De Borst, R. (1988). Analysis of concrete fracture in 'direct' tension. *International Journal of Solids and Structures,* **25**, 12, 1381-1394.

Rots, J.G. (1988). Computational modelling of concrete fracture. PhD thesis, Delft University of Technology, Delft, The Netherlands.

Rots, J.G. & De Borst, R. (1987). Analysis of mixed-mode fracture in concrete. *Journal of Engineering Mechanics*, ASCE, **113**, 11, 1739-1758.

Sandler, I.S. (1984). Strain softening for static and dynamic problems. In *Proceedings of Symposium on Constitutive Equations: Micro, Macro and Computational Aspects*, ASME Winter Annual Meeting, ed. K. Willam. ASME, New York, pp. 217-231.

Schlangen, E. & Van Mier, J.G.M. (1991*a*). Boundary effects in mixed mode I and II fracture of concrete. In *Fracture Processes in Concrete, Rock and Ceramics,* Vol II, ed. J.G.M. van Mier, J. G. Rots & A. Bakker. Chapman & Hall Publishers, London/New York, pp. 705-716.

Schlangen, E. & Van Mier, J.G.M. (1991*b*). Lattice model for numerical simulation of concrete fracture. In *Proceedings international EPRI conference on DAM FRACTURE,* ed. V.E. Saouma, R. Dungar & D. Morris. EPRI, Palo Alto, pp. 511-527.

Schlangen, E. & Van Mier, J.G.M. (1992). Experimental and numerical analysis of micromechanism of fracture of cement based composites. In Cement and Concrete Composites, Special issue, ed. V.C. Li. (in print).

Shah, S.P. & Carpinteri, A.(eds.). (1991). *Fracture mechanics of concrete: test methods:* RILEM report 89-FMT. Chapman & Hall, London.

Sih, G.C. (1974). Strain energy density factor applied to mixed mode problems. *International Journal of Fracture,* **10**, 3, 305-322.

Sih, G.C. (1984). Mechanics of material damage in concrete. *Fracture Mechanics of Concrete: Material Characterization and Testing EAFM Series*, ed. A. Carpinteri & A. Ingraffea. Martinus Nijhoff publishers, The Hague, pp. 67-110.

Sluys, L.J. & de Borst, R. (1992). Mesh-sensitivity analysis of an impact test on a double-notched specimen. Paper to be presented at 33rd U.S. Rock Mechanics Symposium, Santa Fe, New Mexico, 08-10, June.

Suidan M. & Schnobrich, W.C. (1973). Finite element analysis of reinforced concrete. *Journal of the Structural Division, ASCE*, **99**, 10, 2109-2122.

Swartz S.E., Taha, N.M. (1990). Mixed mode crack propagation and fracture in concrete. *Engineering Fracture Mechanics*, **35**, 1/2/3, 137-144.

Tokatly, Z.Y. & Barr, B. (1991). Size effects in mode II fracture. In *Fracture Processes in Concrete, Rock and Ceramics Vol I.* ed. J.G.M. van Mier, J. G. Rots & A. Bakker, Chapman & Hall Publishers, London/New York, pp. 473-482.

Van Mier, J.G.M. (1984). Strain softening of concrete under multiaxial conditions. PhD thesis, Eindhoven University of Technology, Eindhoven, The Netherlands.

Van Mier, J.G.M. (1986a). Multiaxial strain softening of concrete Part I: Fracture. *Materials and Structures, RILEM*, **19**, 111, 179-190.

Van Mier, J.G.M. (1986b). Fracture of concrete under complex stress. *HERON*, **31**, 3, 1-90.

Van Mier, J.G.M. (1988). Fracture study of concrete specimens subjected to combined tensile and shear loading. In *Proceedings of the International Conference on Measurement and Testing in Civil Engineering*, ed. J.F. Jullien. INSA, Lyon-Villeurbanne, pp. 337-347

Van Mier, J.G.M. & Nooru-Mohamed, M.B.,(1989), Fracture of concrete under tensile and shear-like loading. In *Fracture Toughness and Fracture Energy - Test Methods for Concrete and Rock*, ed. H. Mihashi, H.Takahashi & F.H.Wittmann. A.A. Balkema, Rotterdam, pp. 549-563.

Van Mier, J.G.M. & Nooru-Mohamed M.B. (1990). Geometrical and structural aspects of concrete fracture. *Engineering Fracture Mechanics,* **35**, 4/5, 617- 628.

Van Mier, J.G.M. (1991). Mode I fracture of concrete: discontinuous crack growth and crack interface grain bridging. *Cement and Concrete Research*, **21**, 1, 1-15.

Van Mier, J.G.M., Schlangen, E. & Nooru-Mohamed, M.B. (1992). Shear fracture in cementitious composites part I: experimental observations. In *Proceedings of the First International Conference on Fracture Mechanics of Concrete Structures* (Framcos 1). Breckenridge, Colorado, 01-05 June.

Vonk, R.A., Rutten, H.S., Van Mier, J.G.M. & Fijneman, H.J. (1991). Micromechanical simulation of concrete softening. In *Fracture Processes in Concrete, Rock and Ceramics Vol I.* ed. J.G.M. van Mier, J. G. Rots & A. Bakker, Chapman & Hall Publishers, London/New York, pp. 129-138.

Walraven, J.C. (1980). Aggregate Interlock: a theoretical an experimental analysis. PhD thesis. Delft University of Technology, Delft. The Netherlands.

Walraven, J. & Keuser, W. (1987). The shear retention factor as a compromise between numerical simplicity and realistic material behaviour. *Darmstadt Concrete*, **2**, 221-234.

Watkins, J. & Liu, K.L.W. (1985). A finite element study of the short beam specimen under Mode II loading. *International Journal of Cement Composites and Lightweight Concrete*, **7**, 1, 39-47.

Wittmann, F.H. (1983). Structure of concrete with respect to crack formation. In *Fracture Mechanics of Concrete*. ed. F.H. Wittmann, Elsevier, Amsterdam, pp. 43-74.

Zhou, F. (1988). Some aspects of tensile behaviour and structural response of cementitious materials. Report TVBM-1008, Division of Building Materials, Lund Institute of Technology, Lund, Sweden.

Appendix A0

Table A0: *Information regarding test series*

Batch Number	Date of casting	Specimen No	Date of loading	Age of Loading	Load-path Number	Update in Testing	Remarks
14	17.02.88	14-01	06.04.88	49	1(a)	2LVDTS(vertical) 6 extensometers	
(2 mm)		14-02	13.04.88	56	1(a)	"	
		14-04	19.04.88	62	1(b)	"	
		14-05	22.04.88	65	1(b)	"	
15	02.03.88	15-02	03.05.88	62	1(b)	"	
(2 mm)		15-03	19.05.88	78	1(b)	"	
		15-04	26.05.88	85	1(b)	"	
		15-05	01.06.88	91	1(b)	"	
17	29.03.88	17-01	24.06.88	87	2	" + $\delta = 400\,\mu m$	
(2 mm)		17-02	28.06.88	91	2	" + $\delta = 200\,\mu m$	
		17-03	29.06.88	92	2	" + $\delta = 300\,\mu m$	
		17-04	01.07.88	94	2	" + $\delta = 65\,\mu m$	
		17-05	06.07.88	99	2	" + $\delta = 250\,\mu m$	
18	06.04.88	18-01	08.07.88	93	2	" + $\delta = 150\,\mu m$	
(2 mm)		18-02	12.07.88	97	2	" + $\delta = 225\,\mu m$	
		18-03	14.07.88	99	2	" + $\delta = 275\,\mu m$	
		18-04	15.07.88	100	2	" + $\delta = 250\,\mu m$	

Trial batches 19,20,23,24,25 and 31

In these trial experiments following improvements were made to the test set up:

(a) Two horizontal LVDTs were fixed, one at the front bottom half and the other at the rear bottom half.

(b) A number of four LVDTs were used in the vertical direction instead of two. Two of them were placed near both notches of the front face and two at the rear face.

(c) In order to avoid glue failure all four edges of the specimen were polished and an impermeable polyster coating was applied a week before the specimen is glued to the machine.

26	28.09.88	26-01	15.11.88	48	3a	vertical(four), (2 mm) horizontal (two) LVDTs & 6 exten. $\delta = 275\,\mu m$.
		26-02	10.11.88	43	3b	" + $\delta = 275\,\mu m$.
		26-03	16.11.88	49	3b	" + $\delta = 225\,\mu m$.
		26-04	17.11.88	50	3b	" + $\delta = 250\,\mu m$

		26-05	18.11.88	51	3a	" + $\delta = 225\,\mu$m.
		26-06	22.11.88	55	3a	" + $\delta = 250\,\mu$m.
27 (16 mm)	12.10.88	27-01	24.11.88	43	3a	" + $\delta = 300\,\mu$m
		27-02	25.11.88	44	3b	" + $\delta = 300\,\mu$m.
		27-03	29.11.88	48	3a	" + $\delta = 400\,\mu$m.
		27-04	30.11.88	49	3a	" + $\delta = 200\,\mu$m.
		27-05	16.12.88	65	3b	" + $\delta = 200\,\mu$m.
		27-06	19.12.88	68	3b	" + $\delta = 400\,\mu$m.
28 (16 mm)	26.10.88	28-01	20.12.88	55	3b	" + $\delta = 200\,\mu$m.
		28-02	21.12.88	56	3a	" + $\delta = 300\,\mu$m.
		28-03	22.12.88	57	3b	" + $\delta = 300\,\mu$m.
		28-04	23.12.88	58	3b	" + $\delta = 400\,\mu$m.
		28-05	10.01.89	76	3a	" + $\delta = 200\,\mu$m.
		28-06	11.01.89	77	3a	" + $\delta = 400\,\mu$m.
29 (Lytag)	09.11.88	29-01	17.01.89	69	3a	" + $\delta = 100\,\mu$m.
		29-02	18.01.89	70	3a	" + $\delta = 150\,\mu$m.
		29-03	19.01.89	71	3b	" + $\delta = 50\,\mu$m.
		29-04	20.01.89	72	3b	" + $\delta = 100\,\mu$m.
		29-05	23.01.89	75	3b	" + $\delta = 150\,\mu$m.
		29-06	24.01.89	76	3b	" + $\delta = 50\,\mu$m.
30 (Lytag)	23.11.88	30-01	25.01.89	63	3b	" + $\delta = 100\,\mu$m.
		30-02	26.01.89	64	3b	" + $\delta = 50\,\mu$m.
		30-03	27.01.89	65	3b	" + $\delta = 150\,\mu$m.
		30-04	30.01.89	68	3b	" + $\delta = 50\,\mu$m
		30-05	31.01.89	69	3b	" + $\delta = 150\,\mu$m
		30-06	01.02.89	70	3b	" + $\delta = 100\,\mu$m.
32 (2 mm)	07.12.88	32-01	02.02.89	57	3b	" + $\delta = 225\,\mu$m.
		32-02	03.02.89	58	3a	" + $\delta = 250\,\mu$m.
		32-03	06.02.89	61	3a	" + $\delta = 225\,\mu$m.
		32-04	07.02.89	62	3a	" + $\delta = 275\,\mu$m.
		32-05	08.02.89	63	3b	" + $\delta = 250\,\mu$m.
		32-06	10.02.89	65	3b	" + $\delta = 275\,\mu$m.

From batches 14 till 32 the specimen dimension was 200x200x50 mm. However, in the following series two other specimen sizes were used.

In batches 41,42,43,44 and 45, selected number of specimens were used for trial tests.

Batch Number	Date of casting	Specimen No	Specimen Size (mm)	Date of Loading	Age of Loading (days)	Load-path Number	Remarks
46	04.12.89	46-01	200	30.01.90	58	5a	
		46-02	200	01.05.90	149	6a	

		46-03	200	02.03.90	99	0
		46-04	200	14.02.90	73	6c
		46-05	200	15.01.90	43	4b
		46-07	100	15.02.90	74	6a
		46-08	100	01.02.90	60	5b
		46-09	100	24.04.90	151	4a
		46-10	100	13.03.90	100	0
		46-11	100	16.11.90	44	4c
		46-13	50	15.06.90	194	5a
		46-15	50	18.01.90	46	4a
		46-16	50	21.02.90	80	6b
		46-19	50	08.06.90	187	5c
		46-20	100	06.11.90	338	4a*
47	06.12.89	47-01	200	23.04.90	149	4b
		47-02	200	02.03.90	86	6a
		47-04	200	05.02.90	61	5b
		47-05	200	15.03.90	99	0
		47-06	200	24.01.90	49	4c
		47-07	100	22.01.90	47	4a
		47-08	100	05.03.90	89	6b
		47-09	100	03.05.90	148	5b
		47-10	100	06.02.90	62	5c
		47-13	50	07.02.90	63	5a
		47-15	50	04.07.90	210	6a
		47-16	50	19.03.90	103	0
		47-17	50	06.03.90	90	6c
		47-22	50	09.07.90	215	4b
48	11.12.89	48-01	200	07.03.90	86	6b
		48-02	200	08.02.90	59	5c
		48-03	200	25.01.90	45	4a
		48-04	200	04.05.90	144	5b
		48-07	100	21.03.90	100	0
		48-08	100	07.05.90	145	6a
		48-09	100	26.01.90	46	4b
		48-10	100	08.03.90	87	6c
		48-11	100	12.02.90	63	5a
		48-13	50	13.06.90	184	4a
		48-15	50	09.03.90	88	6a
		48-16	50	20.03.90	99	0
		48-17	50	13.12.90	367	5b
		48-18	50	29.03.90	108	4c
		48-16	50	20.05.90	160	0
		48-19	100	08.11.90	332	5a*
		48-20	50	13.11.90	337	5a*
		48-21	50	09.11.90	333	4a*

Appendix A1: Additional results of load-path 1(b) experiments.

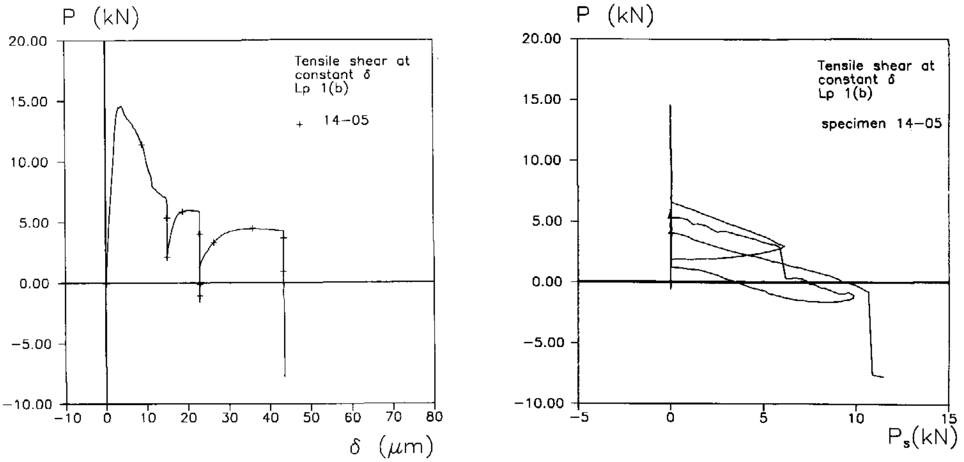

Figure A1.1 P-δ (a) and P-P_S (b) response for specimen 14-05: load-path 1(b) experiment.

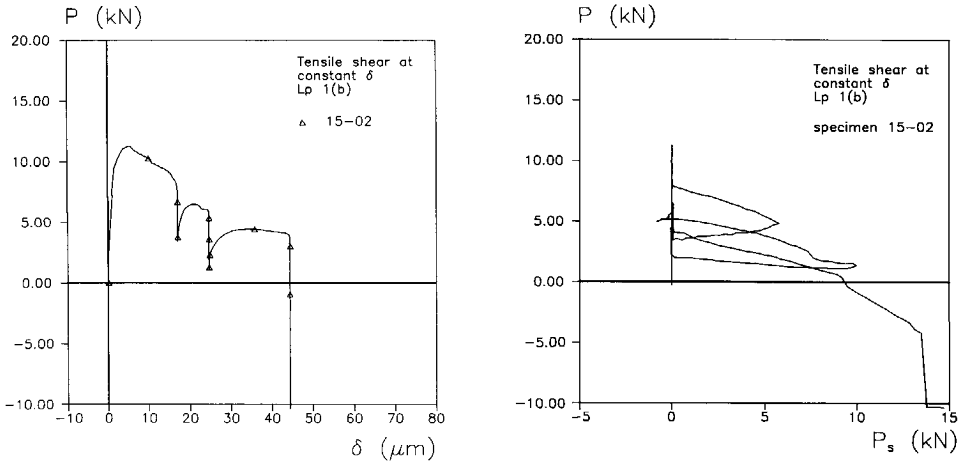

Figure A1.2 P-δ (a) and P-P_S (b) response for specimen 15-02: load-path 1(b) experiment.

Appendix A2: Test Scheme corresponding ot load-path 3

Table A2:

Unloading axial deformation δ_a (μm)	Material	Load-path 3a	Load-path 3b
50	Lytag 12 mm	29-06 ***	29-03 30-04
100	"	29-01 ***	29-04 30-01
150	"	29-02 30-05	29-05 30-03
200	Concrete 16 mm	*** 28-05	27-05 28-01
225	Mortar 2 mm	26-05 32-03	26-03 ***
250	"	26-06 ***	*** ***
275	"	26-01 32-04	26-02 32-06
300	Concrete 16 mm	27-01 ***	27-02 28-03
400	"	*** 28-06	*** 28-04

Relatively large off-sets were observed in this test series. The off-set is defined as the amount of shear displacement δ_s during axila tension. A result was rejected when the off-set was larger than 30 μm. In this series 10 out of 36 tests were discarded. The off-set is most probably caused by the eccentricities in the test set up. Eccentricities may arise during glueing of the specimen in the machine or due to deviations in the specimen dimension. Regarding the off-set problem reader is referred to Nooru-Mohamed & Van Mier [88].

Appendix A3: Load-path 3a/3b results for 2 mm mortar.

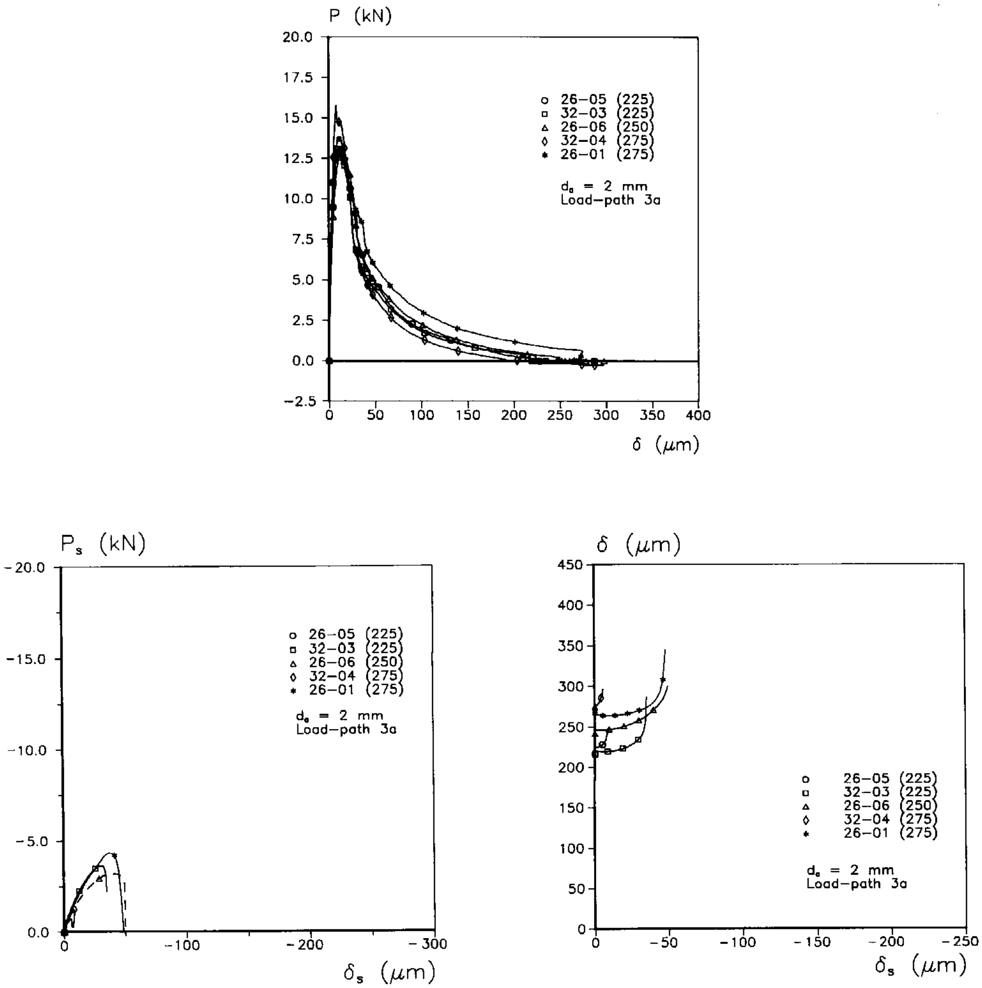

Figure A3.1 P-δ (a), P_S-δ_S (b) and δ-δ_S (c) response for 2 mm mortar: load-path 3a experiments.

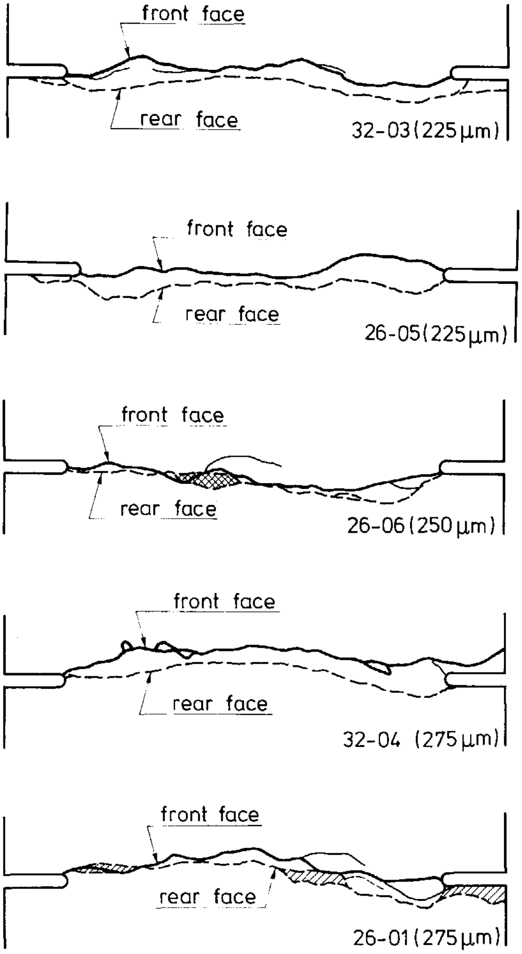

Figure A3.2 (a)-(e) Crack patterns associated with experiments in Figure A3.1.

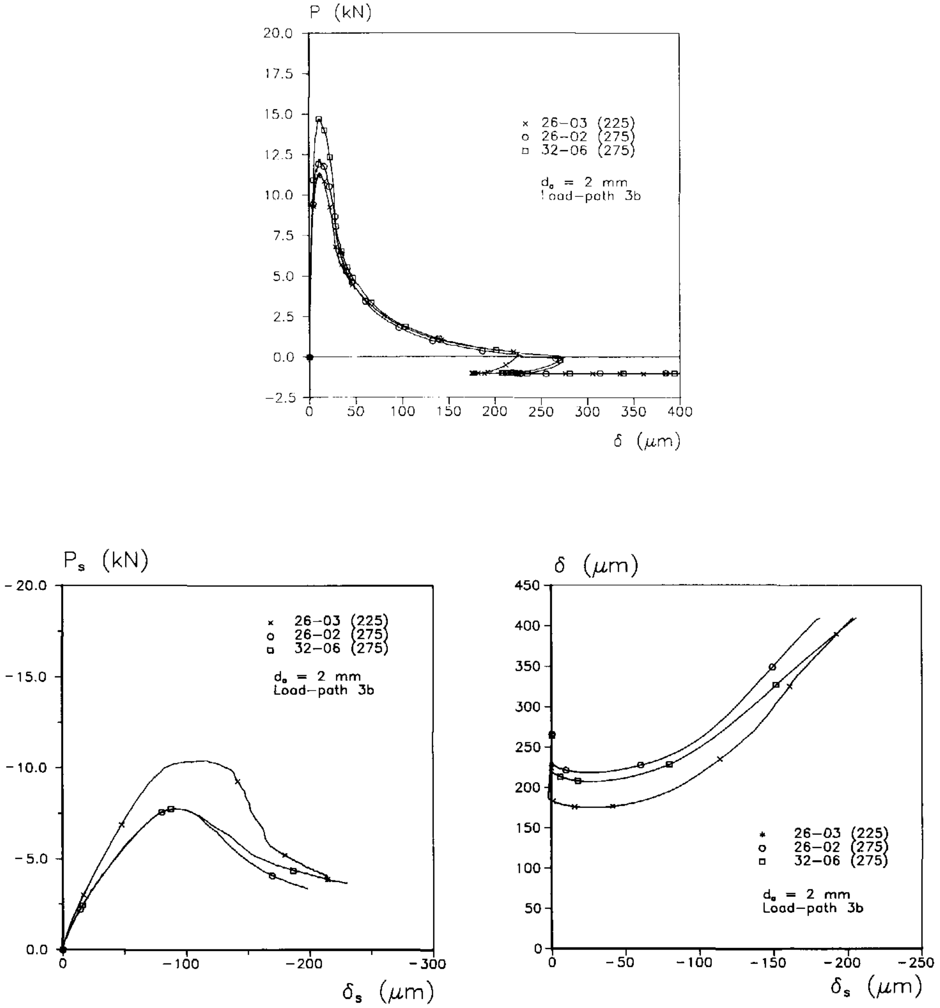

Figure A3.3 P-δ (a), P_S-δ_S (b) and δ-δ_S (c) response for 2 mm mortar: load-path 3b experiments.

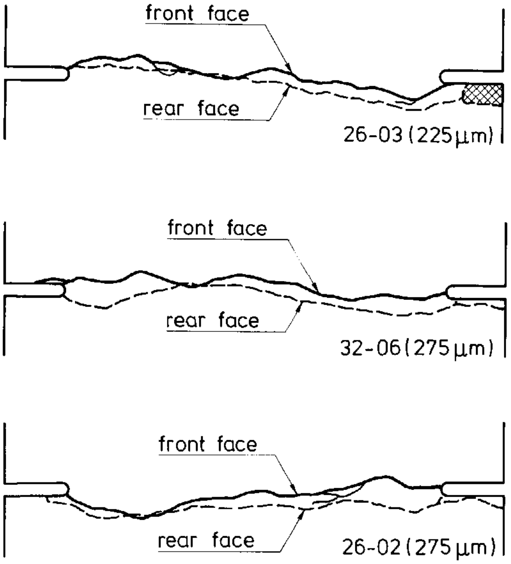

Figure A3.4 (a)-(e) Crack patterns associated with experiments in Figure A3.3.

Appendix A4: Load-path 3a/3b results for 16 mm concrete.

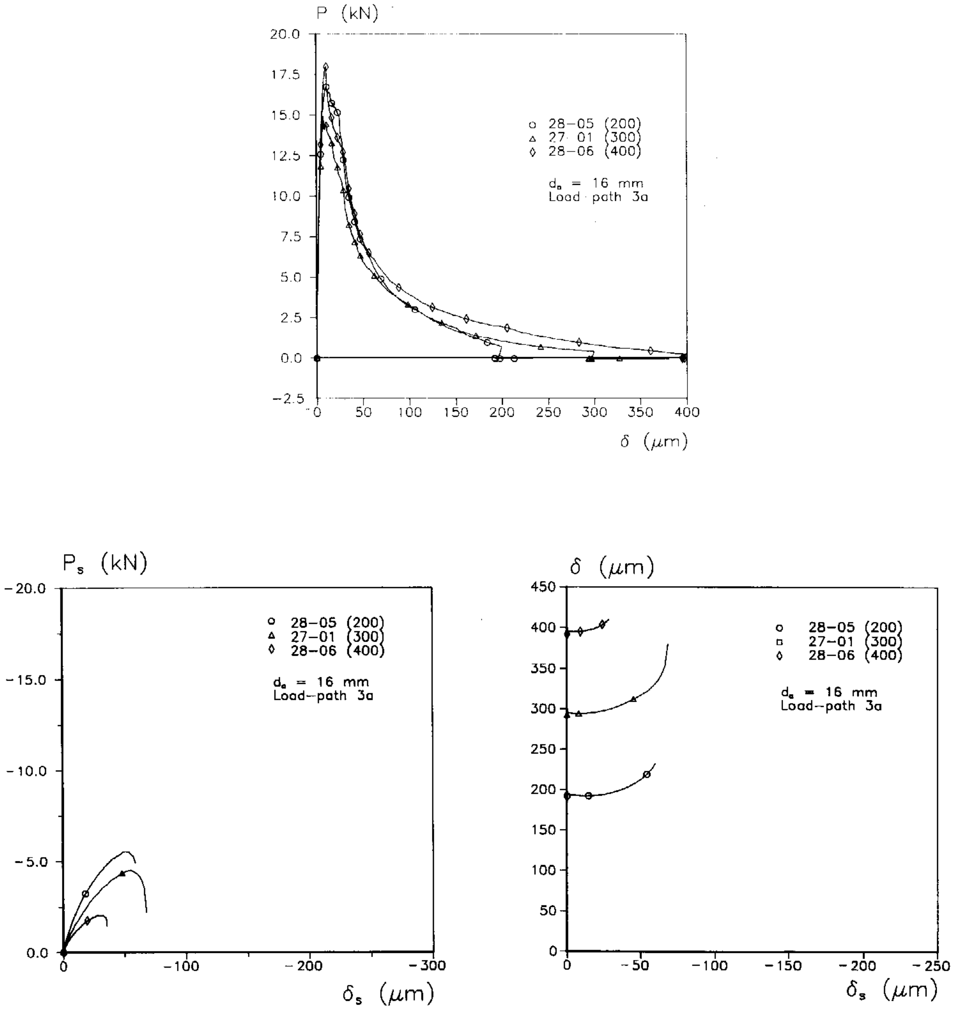

Figure A4.1 P-δ (a), P_S-δ_S (b) and δ-δ_S (c) response for 16 mm concrete: load-path 3a experiments.

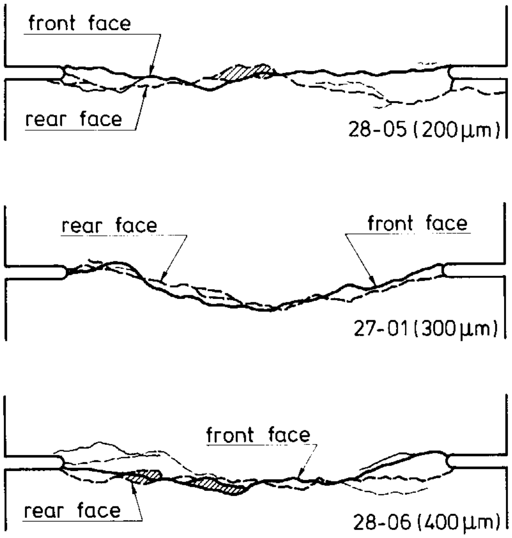

Figure A4.2 (a)-(e) Crack patterns associated with experiments in Figure A4.1.

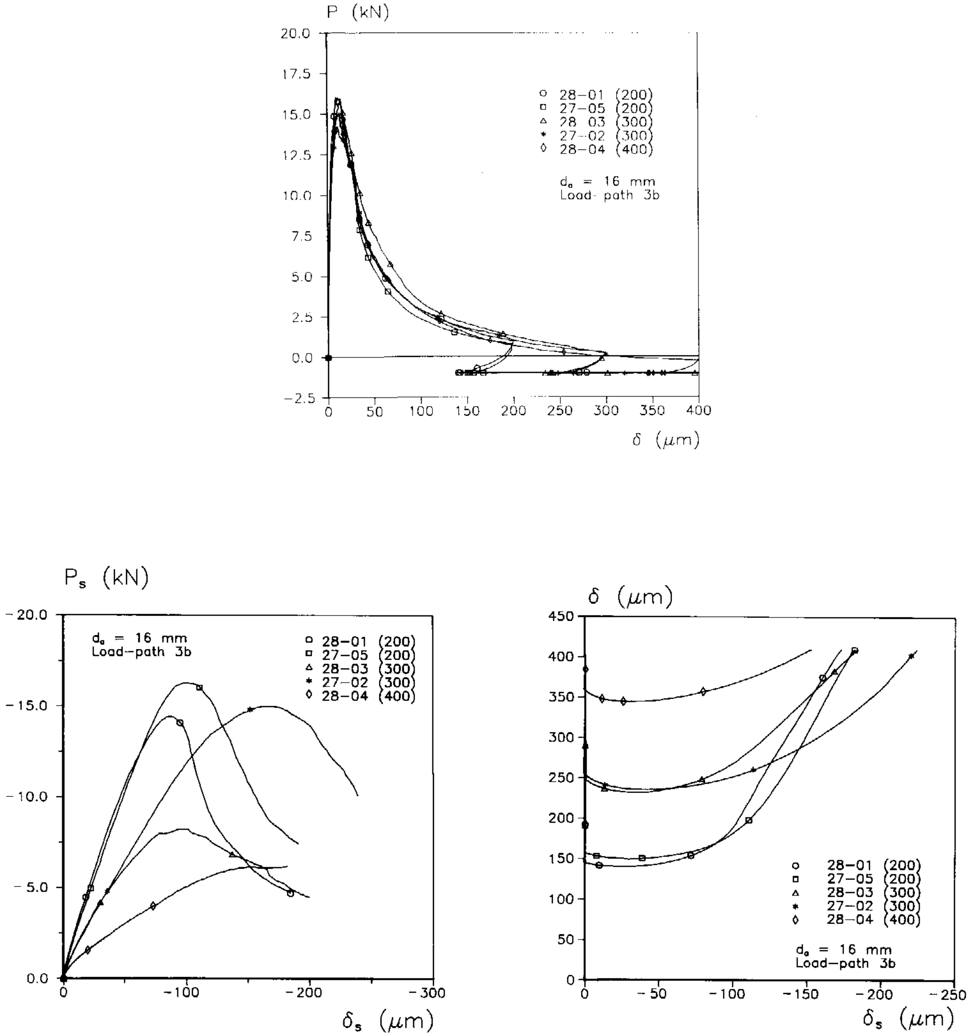

Figure A4.3 P-δ (a), P_S-δ_S (b) and δ-δ_S (c) response for 16 mm concrete: load-path 3b experiments.

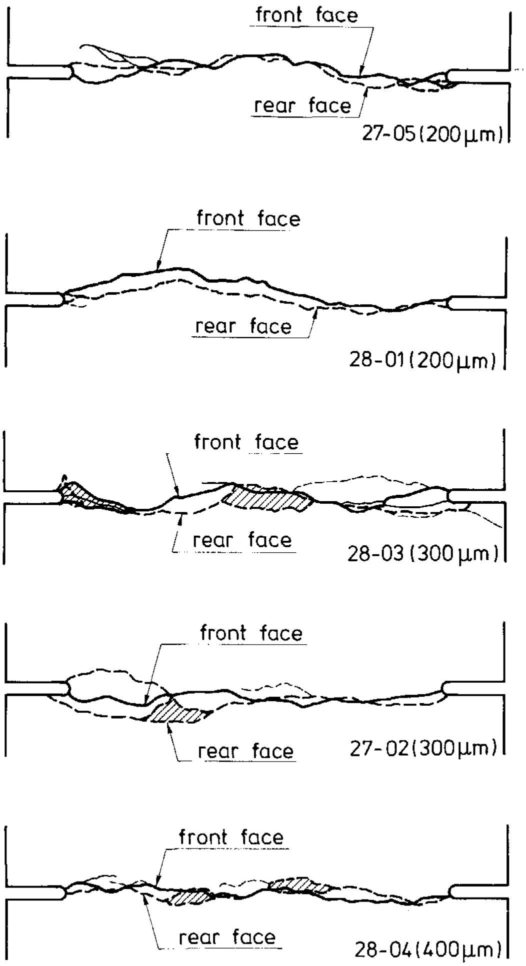

Figure A4.4 (a)-(e) Crack patterns associated with experiments in Figure A4.3.

Appendix A5: Test scheme for load-path 0, 4, 5 and 6 experiments

Table A5

Size	200X200x50	100x100x50	50x50x50
Load-path			
LP 0 (2 glue platens)	47-05	46-10	48-16
LP 0 (4 glue platens)	46-03	48-07	47-16
LP 4a	48-03	47-07 46-09	48-13 46-15
LP 4b	46-05 47-01	48-09	47-22
LP 4c	47-06	46-11	48-18
LP 5a	46-01	48-11	46-13 47-13
LP 5b	47-04 48-04	46-08 47-09	48-17
LP 5c	48-02	47-10	46-19
LP 6a	47-02 46-02	46-07 48-08	47-15 48-15
LP 6b	48-01	47-08	46-16
LP 6c	46-04	48-10	47-17

In order to propose a test series, sufficient amount of trial tests were conducted, see Table A0. A limited amount of duplicate tests were carried out, since only three tests could be performed in a week. The above test series was generated in a random manner.

Appendix A6: Crack patterns corresponding to load-path 5c experiments.

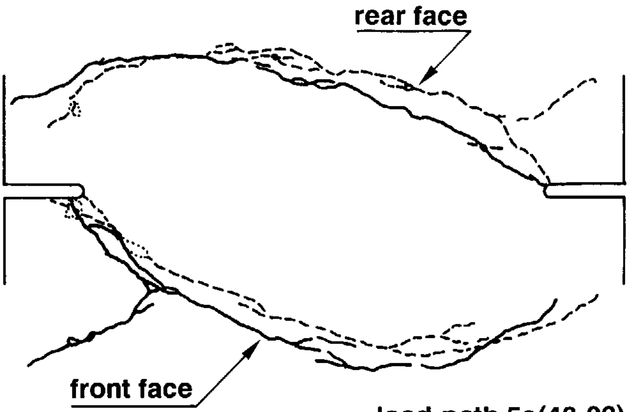

load-path 5c(48-02)
200x200x50

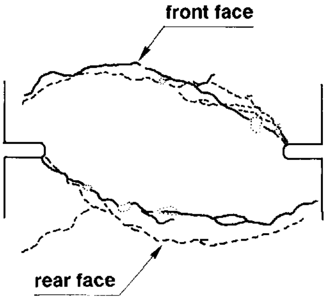

load-path 5c(47-10)
100x100x50

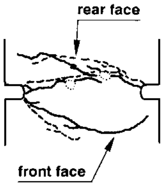

load-path 5c(46-19)
50x50x50

Figure A6 (a)-(c) Crack patterns corresponding to load-path 5c experiments.

Appendix A7: Crack patterns corresponding to load-path 6b and 6c.

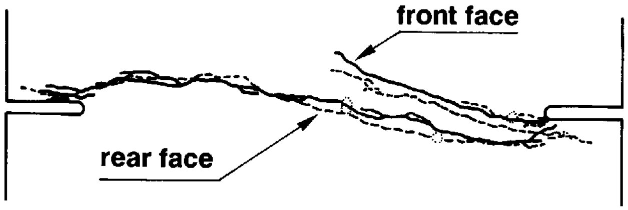

load-path 6b(48-01)
200x200x50

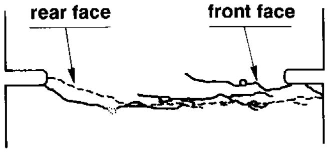

load-path 6b(47-08)
100x100x50

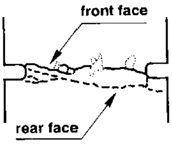

load-path 6b(46-16)
50x50x50

Figure A7.1 (a)-(c) Crack patterns corresponding to load-path 6b experiments.

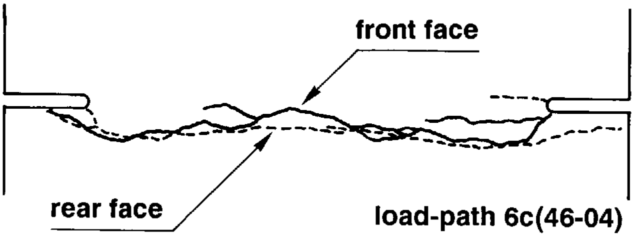

load-path 6c(46-04)
200x200x50

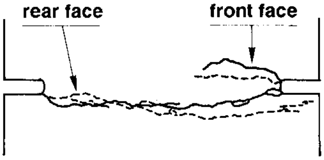

load-path 6c(48-10)
100x100x50

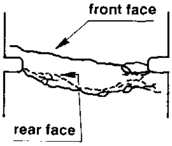

load-path 6c(47-17)
50x50x50

Figure A7.2 (a)-(c) Crack patterns corresponding to load-path 6c experiments.

Summary

An experimental investigation into the behaviour of concrete under mixed-mode loading is undertaken in the light of fracture mechanics. For this purpose the biaxial machine built at the Stevin Laboratory is used. The biaxial machine is unique and consists of two independent stiff square loading frames. The frames can move independent of one another along the axial and the lateral directions. Double-Edge-Notched(DEN) concrete plates of dimension up to 200x200 mm can be loaded in any combination of tension and shear in displacement control.

Three different DEN specimen sizes with the thickness of 50 mm were adopted. Three types of materials, namely normal concrete of 2 and 16 mm maximum aggregate size and Lytag lightweight concrete of 12 mm maximum aggregate size were used.

Seven load-paths have been pursued in this study. They can be classified into three broad categories: (1) an investigation of the shear strength or stiffness of partially opened cracks. Here, the specimens were pre-cracked under a tensile load to small crack openings within the range 0 to 400 μm, in a fully controlled condition. Thereafter, a lateral shear was applied. The results of these experiments are utilized to identify the role of aggregate interlock when the crack openings are small; (2) a study of the behaviour of concrete specimens which were first sheared (mode II) without pre-cracking and subsequently loaded in tension; (3) a study of the behaviour of concrete when tension (mode I) and shear (mode II) were acting simultaneously such that, the ratio of the axial (δ) to the lateral deformation (δ_s) remains a constant throughout the test.

In category (1), depending on the boundary conditions secondary cracking or sliding failure compete. Subjecting narrow cracks to shear led to secondary cracking. The amount of crack opening and the confinement over the crack plane are important. Test were performed with -0.13 MPa or zero confinement. Sliding failure was observed when shear was applied for crack openings larger than 250 μm and zero confinement over the crack plane. The above phenomenon limit the range of applicability of the aggregate interlock theories.

In category (2), two overlapping cracks formed from the two notches and resemble the failure mode observed in double-notched four point shear beams with narrow shear zone. Self similar crack patterns were observed for different specimen sizes.

In category (3) changing the specimen size led to a transition in failure modes: formation of overlapping straight cracks to inclined distributed cracks.

In sum, five failure modes can be identified from the present experimental observations. They are: (1) tensile diagonal failure (2) sliding failure (3) formation of compressive struts (4) formation of overlapping curved cracks (5) a transition between overlapping straight cracks to inclined distributed cracks.

The size effect law of Bazant was compared for biaxial tests with proportional load-path and shows an opposite trend. This might be attributed to the difference in failure modes. From the various load-path investigated, it is concluded that behaviour of the specimen under biaxial loading is path dependent.

The results reported in this study can be used to tune and verify the various smeared crack models as well as micromechanical models.

Samenvatting

Het gedrag van beton onder mixed-mode belasting is bestudeerd door middel van een experimenteel onderzoek op het gebied van de breukmechanica. Daarbij is gebruik gemaakt van de in het Stevin Laboratorium ontwikkelde biaxiale opstelling. Deze opstelling is uniek en bestaat uit twee onafhankelijke stijve belastingframes. De frames kunnen onafhankelijk van elkaar bewegen in horizontale en verticale richting. Betonnen platen met een afmeting van 200*200 mm voorzien van een zaagsnede aan twee zijden (DEN) kunnen verplaatsingsgestuurd worden belast door elke willekeurige combinatie van trek- en schuifbelasting.

In de proeven is gebruikt gemaakt van DEN-proefstukken met drie verschillende afmetingen en een dikte van 50 mm. Hiervoor zijn drie materiaalsamenstellingen toegepast, namelijk beton met een maximale afmeting van de toeslagkorrels van 2 en 16 mm en Lytag lichtbeton met een maximale afmeting van de toeslagkorrels van 12 mm.

In deze studie zijn zeven belastingpaden onderzocht. Ze kunnen worden geclassificeerd in drie categorien: (1) een onderzoek naar de schuifsterkte of stijfheid van gedeeltelijk geopende scheuren. In dit geval zijn de proefstukken eerst volledig gecontroleerd gescheurd onder trekbelasting tot een kleine scheuropening varierend tussen 0 en 400 μm. Vervolgens is een schuifbelasting aangebracht. De resultaten van deze experimenten zijn gebruikt om de invloed van 'aggregate interlock' vast te stellen bij kleine scheuropeningen; (2) een onderzoek naar het gedrag van betonnen proefstukken waarbij eerst een schuifbelasting (mode II) wordt aangebracht en vervolgens een trekbelasting; (3) een onderzoek naar het gedrag van beton wanneer gelijktijdig een trek- (mode I) en een schuifbelasting (mode II) wordt aangebracht, zodanig dat de verhouding van de scheuropening (δ) en schuifverplaatsing in de scheur (δ_S) constant blijft gedurende de proef.

In categorie (1) treedt afhankelijk van de randvoorwaarden secundaire scheurvorming of schuifbezwijken op. Bij een kleine opening van de scheuren die op afschuiving worden belast treedt secundaire scheurvorming op. Bepalend hierbij zijn de grootte van de scheuropening en de grootte van de normaalkracht in de scheurzone. De proeven zijn uitgevoerd met een normaalkracht van -0.13 of 0 MPa. Schuifbezwijken treedt op wanneer afschuiving wordt aangebracht bij scheuropeningen groter dan 250 μm en geen normaalkracht over de scheurzone aanwezig is. Het bovengenoemde fenomeen beperkt het gebied waar 'aggregate interlock' theorien kunnen worden toegepast.

In categorie (2) ontstaan twee overlappende scheuren vanuit de twee zaagsneden. Dit komt overeen met het breukmechanisme dat is gevonden in balken met twee zaagsneden

belast op vier-punts-afschuiving, met een smalle afschuifzone. Identieke scheurpatronen zijn gevonden voor verschillende proefstukafmetingen.

In categorie (3) leidt een variatie van proefstukafmeting tot een verandering van het breukmechanisme: een verschuiving van overlappende rechte scheuren naar gekromde verdeelde scheuren.

Samengevat kunnen vijf verschillende breukmechanismen worden onderscheiden in de experimentnaei: (1) diagonaal trek-bezwijken; (2) afschuif-bezwijken; (3) vorming van druk-diagonalen; (4) vorming van overlappende gekromde scheuren; (5) een verschuiving van overlappende rechte scheuren naar gekromde verdeelde scheuren.

De 'size effect law' van Bazant is geverifieerd voor de biaxiale proeven met een proportioneel belastingpad. De resultaten vertonen een tegengesteld gedrag. Een mogelijke reden hiervoor is het verschil in breukmechanisme. Uit de verschillende onderzochte belastingpaden kan worden geconcludeerd dat het gedrag van de proefstukken onder biaxiale belasting pad-afhankelijk is.

De resultaten van dit onderzoek kunnen worden gebruikt om verschillende uitgesmeerde scheurenconcepten en micromechanica-modellen te tunen en te toetsen. Deze numerieke modellen zijn geschikt voor het uitvoeren van constructieberekeningen (Betonmechanica) en als hulpmiddel bij materiaalkundig onderzoek.